学位論文

An Observational Study of Interstellar Ices in Nearby Galaxies with AKARI Near-Infrared Spectroscopy

「あかり」近赤外線分光観測に基づいた近傍銀河に存在する星間氷の観測的研究

山岸 光義

2014 年 3 月

Contents

List of Figures

List of Tables

Abstract

Interstellar ices are formed on the surface of dust grains in dense molecular clouds with temperatures of $\sim$ 10 K. It is widely known that absorption features due to ices are sensitive to the interstellar environment such as temperature, chemistry, and radiation field. Among various ices, CO_2 ice is one of the most important ices as a probe of the interstellar environment. That is because CO_2 ice is a secondary product unlike H_2O and CO ices which are primarily formed on dust grains. By using various species of ices, discussions on the interstellar environment for Galactic sources have been intensively performed to date. In contrast, ices in external galaxies have not been fully studied yet. In particular, multiple ice features including CO_2 ice have not been fully utilized yet due to the limit of the wavelength coverage and sensitivity of the instruments..

In this thesis, I expand the discussions for Galactic sources to extra-galactic sources, and establish ices as probes of the interstellar environment in nearby galaxies. In order to achieve the goal, H_2O ice at a wavelength of 3.05 μm and CO_2 ice at a wavelength of 4.27 μm are systematically searched with the AKARI near-infrared (NIR) slit spectroscopy between 2.5–5.0 μm. In total, NIR spectra for 1031 regions in 158 nearby galaxies are analyzed, which is the most extensive NIR spectroscopic survey for the ices in nearby galaxies.

As a result of the search, H_2O ice is significantly detected from 125 regions in 30 galaxies, while CO_2 ice is detected from 54 regions in 12 galaxies. Comparing the resultant column densities of the ices with the polycyclic aromatic hydrocarbon (PAH) 3.3 μm and Brα intensities in the NIR spectra, it is found that H_2O and CO_2 ices are detected in regions where PAHs are abundant and Brα is bright, respectively. The CO_2/H_2O ice abundance ratios are in a range of 0.05–0.30, and the typical ratio is 0.14$\pm$0.01 which is the same as that for Galactic sources.

In addition to the statistical study, the ice features in three galaxies (NGC 253, M 82, and NGC 1097) are analyzed in detail, and spatial distributions of the ices in the galaxies are discussed. In the three galaxies, the spatial distributions of the ices show overall correspondence with those of CO gas. It is also found that the spatial distributions of H_2O ice is clearly different from that of CO_2 ice in M 82, suggesting that the ice-forming interstellar environment changes in a galaxy.

Based on the results, the applicability of the ices is investigated as probes of the interstellar environment. First, correlations between the column densities of the ices and $J - K_s$ colors are found, which confirms that the ices are probes of the dense interstellar medium. Next, by comparing the variations of the CO_2/H_2O ice abundance ratios with those of the UV radiation environment, it is suggested that CO_2/H_2O ice abundance ratios are enhanced by massive star formation activity in a galaxy. Furthermore, by focusing on the variations of the CO_2/H_2O ice abundance ratios with those of star formation activity on a galactic scale, a positive correlation between the CO_2/H_2O ice abundance ratios and the specific star formation rate is found, which suggests that the relative abundance of CO_2 ice is related to

the phase of the star formation on a galactic scale. Hence, tight links between ices and the interstellar environment are systematically revealed in nearby galaxies.

Chapter 1

Introduction

1.1 Near-infrared observations of the interstellar media

The interstellar medium (ISM) is one of the major constituents of the universe. Spectroscopic observations provide us with many pieces of valuable information on the ISM. In a wide wavelength range form γ-ray to radio, near-infrared (NIR) is one of the most important wavelengths to investigate the ISM. The advantages in using the NIR spectra are simultaneous observations of many spectral features which originate from various phases of the ISM. For example, a typical NIR spectrum for the Galactic star-forming region is shown in Fig. 1.1, which is obtained with the AKARI satellite. The NIR (2.5–5.0 μm, see section 2.1) spectrum shows many spectral features such as absorption features due to interstellar ices and CO gas, emission features due to polycyclic aromatic hydrocarbons (PAHs) and aliphatic hydrocarbons, hydrogen recombination emission lines, and continuum emission due to interstellar hot dust. Additionally, the interstellar extinction in the NIR is much lower than that in optical wavelength ranges. For example, the interstellar extinction at a wavelength of 3.0 μm is about 20 times lower than that at 0.55 μm. Thanks to the low extinction, it is easy to estimate physical quantities correctly. However, an observational disadvantage is also present. We cannot obtain continuous spectra with ground-based telescopes due to the atmospheric absorption: the transmittance of the atmosphere in the NIR is shown in Fig. 1.2. Therefore, observations with satellites are necessary to investigate spectral features in the NIR, although many observations with ground-based telescopes are also performed through the limited atmospheric windows (e.g., L and M bands).

Interstellar ices possess absorption features in the NIR, which are the main targets of this thesis. Interstellar ices are formed in dense molecular clouds with temperature of $\sim$ 10 K, which have many pieces of information on the interstellar environment. As shown in Fig. 1.1, strong absorption features in the NIR include those due to H_2O ice at a wavelength of 3.05 μm and CO_2 ice at a wavelength of 4.27 μm. Details of interstellar ices are described in the next section. In addition to the ice features, there are absorption features due to molecular gases. The absorption feature due to CO gas at 4.6 μm is attributed to the fundamental ($v = 0 \rightarrow 1$) ro-vibrational transition which is observed in dense gas regions such as AGN tori and photospheres of low-mass (K and M types) stars. Originally the feature consists of many narrow lines (e.g., Shirahata et al. 2013), however in low resolution spectra, the features are observed as a broad feature as shown in Fig. 1.1. From the excitation states of CO molecules in high resolution spectra ($R = \frac{\lambda}{\Delta\lambda} \gtrsim 3000$), we can estimate the temperature, density, and kinematics of the CO gas. The

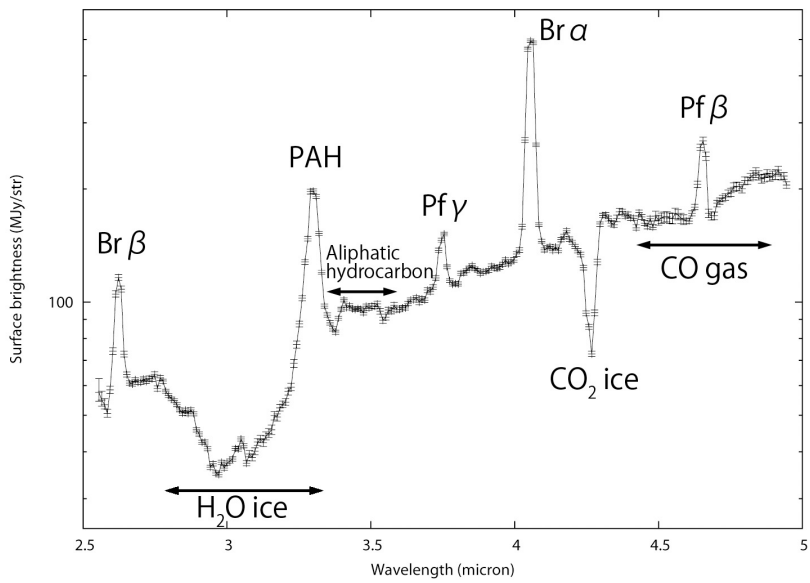

Figure 1.1 Typical NIR (2.5–5.0 μm) spectrum for the Galactic star-forming region W 31 obtained with AKARI.

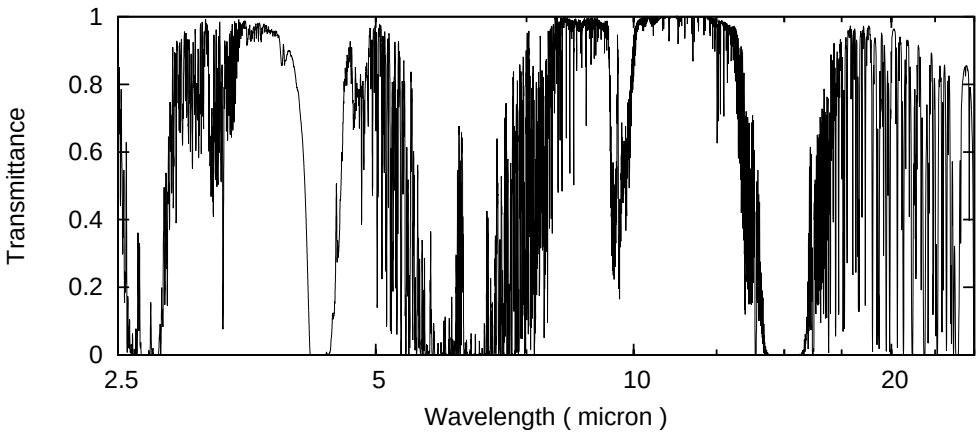

Figure 1.2 Transmittance of the atmosphere in the NIR and MIR at an altitude of 4200 m (`http://www.gemini.edu/`).

absorption feature due to SiO gas at 4.3 μm is attributed to the first overtone ($v = 0 \rightarrow 2$) ro-vibrational transition which arises from photospheres of low-mass stars. Mori et al. (2012) reported the detection of the CO and SiO gas features in early type galaxies where old stellar population is dominant.

The important emission features in the NIR (2.5–5.0 μm) are the PAH 3.3 μm feature and hydrogen recombination lines. The major emission lines and features in the NIR (2.5–5.0 μm) are summarized in Table 1.1. PAHs are large molecules which are composed of tens of benzene rings. Examples of PAHs are shown in Fig. 1.3. PAHs are excited by a far-ultraviolet (FUV) photon and emit spectral features at 3.3, 6.2, 7.7, 8.6, 11.3, 12.7, and 17 μm which are attributed to stretch or bending modes of C-C and C-H bonds. These emission features are ubiquitously observed in the ISM including reflection nebulae, planetary nebulae, and general diffuse ISM. Hence the PAH features are globally used as probes of photo-dissociation regions (PDRs) and the neutral ISM. Since PAHs are small (typically $\sim$ 6 Å) and have planar structures, they are easily destroyed in the harsh environment due to hard UV or X-ray radiation. Among the PAH features, the 3.3 μm feature is attributed to the C-H stretch mode

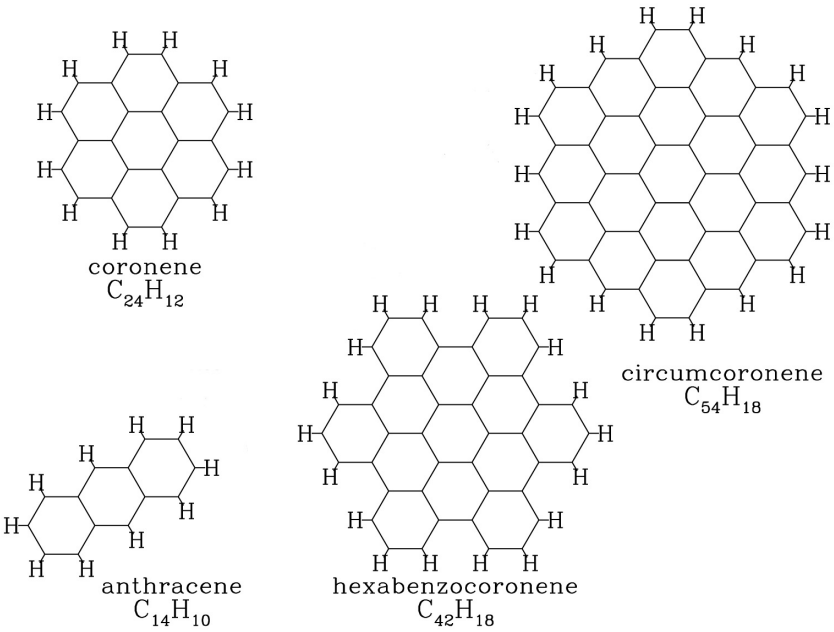

Figure 1.3 Examples of the PAH structures (Draine 2003).

Table 1.1 Major emission features in the NIR (2.5–5.0 μm)

Wavelength (μm)	Name	Notes
Hydrocarbon features		
3.29	PAH 3.3 μm	aromatic C-H stretch
3.40	aliphatic sub-feature	aliphatic C-H stretch (asymmetric CH_2, CH_3)
3.50	aliphatic sub-feature	aliphatic C-H stretch (symmetric CH_2, CH_3)
Hydrogen recombination lines		
4.05	Brα	
2.63	Brβ	
4.65	Pfβ	
3.75	Pfγ	
3.29	Pfδ	blended with the PAH 3.3 μm
3.04	Pf10-5	
2.87	Pf11-5	
2.75	Pf12-5	
4.67	Hu11-6	
4.38	Hu12-6	
4.17	Hu13-6	
H_2 pure rotational lines		
4.69	H_2 0-0 S(9)	
4.41	H_2 0-0 S(10)	
4.18	H_2 0-0 S(11)	
3.84	H_2 0-0 S(12)	

(Allamandola et al. 1989). The emission features at 3.4–3.6 μm are also attributed to the C-H stretch mode but of aliphatic hydrocarbons. The carrier of the PAH 3.3 μm emission feature is thought to be very small PAHs, whereas those in the mid-infrared (MIR) are thought to be relatively large ones (Draine & Li 2007). Thus, the PAH 3.3 μm feature is particularly sensitive to the interstellar radiation environment.

Hydrogen recombination lines in the NIR (2.5–5.0 μm) consist of those in the Brackett ($n \to 4$), Pfund

Table 1.2 Relative intensities of major hydrogen recombination lines in the NIR (2.5–5.0 μm).

Wavelength (μm)	Name	Relative intensity[a]
4.05	Brα	1.000
2.63	Brβ	0.575
4.65	Pfβ	0.203
3.75	Pfγ	0.134
3.29	Pfδ	0.093
3.04	Pf10-5	0.067
2.87	Pf11-5	0.050
2.75	Pf12-5	0.038
4.67	Hu11-6	0.032
4.38	Hu12-6	0.024
4.17	Hu13-6	0.019

[a] Line intensity relative to Brα assuming Case B with temperature of 10^4 K, and electron density of 10^4 cm^{-3} (Hummer & Storey 1987)

($n \rightarrow 5$), and Humphreys ($n \rightarrow 6$) series. The most prominent recombination line in the NIR (2.5–5.0 μm) is Brα at 4.05 μm. The intensities of major recombination lines relative to Brα are listed in Table 1.2. Since these lines are emitted from HII regions mainly ionized by OB stars, they are often used to estimate on-going massive star-formation activities. Additionally, since we can calculate the intrinsic line intensity ratios assuming the Case B (Baker & Menzel 1938) condition, the lines are also used to estimate interstellar extinction by comparing an observed ratio with the intrinsic one. It is notable that Pfδ at 3.29 μm is blended with the PAH 3.3 μm feature. However it is possible to estimate contribution of Pfδ to the 3.3 μm feature by calculating the line intensity from a set of other hydrogen recombination lines (i.e. those listed in Table 1.2).

In the NIR, a variety of continuum emissions are observed. From the regions dominated by old stars such as galactic halos and elliptical galaxies, blue continuum emission is observed, which follows the Rayleigh-Jeans law of blackbody emission with temperature of $T \gtrsim 3000$. From the regions dominated by the ISM such as star-forming regions (Fig. 1.1) and AGN dusty tori, red continuum emission is observed, which is dominated by modified blackbody emission from dust grains with high temperatures ($T \sim 1000$). Additionally from HII regions, free-free emission is observed, which forms a relatively flat continuum slope ($F_\nu \propto \nu^{-0.1}$). Since the slope of the continuum emission depends on the continuum source, we can infer the interstellar environment of the observed region based on a color in a spectrum. Hence, the NIR spectra are abundant in spectral features which can trace various phases of the ISM (HII regions, PDRs, and molecular clouds), and therefore useful as probes to investigate the interstellar environment.

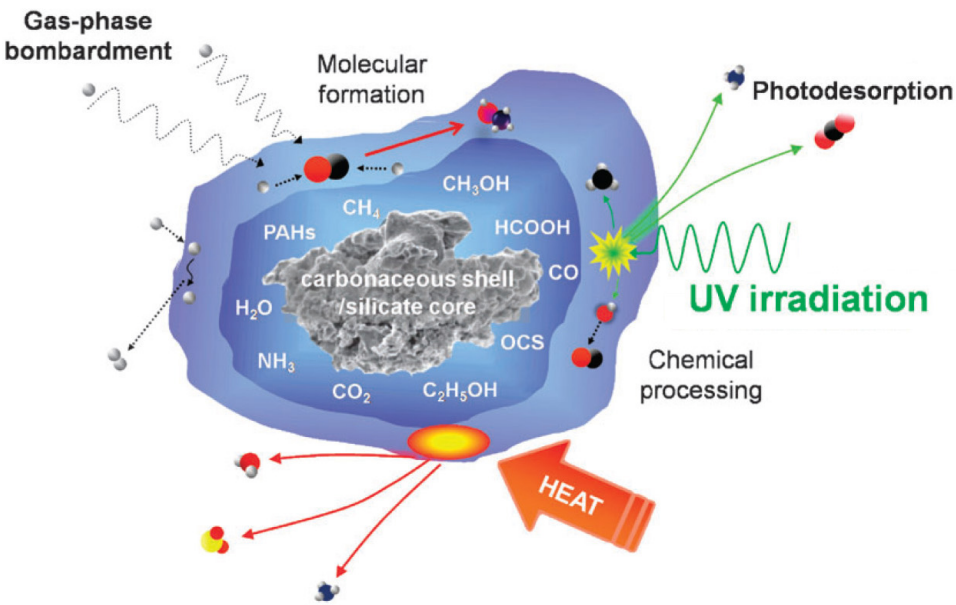

Figure 1.4 Schematic view of ice formation on a dust grain (Burke & Brown 2010). Several examples of molecular species detected in interstellar ices to date are labeled within the inner layer.

1.2 Interstellar ices

Interstellar ices are formed on the surface of dust grains in dense molecular clouds ($T \sim 10$ K, $n_{\rm H} \sim 10^4$ cm^{-3}). Figure 1.4 shows a schematic view of ice formation on a dust grain. In dense molecular clouds, molecules and atoms in the gas phase condense onto a dust grain. Then several molecules are formed via grain surface reactions, and part of the molecules form ice mantles on a dust grain. After ices are formed, ices are affected by the interstellar environment such as UV irradiation and heating. In the case that high-energy photons (UV or cosmic-ray) are irradiated, further processes may undergo, which lead to the formation of complex molecules on dust grains. If temperature of a dust grain rises due to heating, ices are sublimated and the molecules found in the ice mantle are released to the gas phase. Thus, ices play an important role not only in solid-phase chemistry but also in gas-phase chemistry.

1.2.1 Spectral features

Absorption features due to interstellar ices are observed in the NIR and MIR spectra of the ISM. A typical spectrum with absorption features due to ices is shown in Fig. 1.5, while a list of major absorption features (Gibb et al. 2004) is shown in Table 1.3. In the IR spectra, we can observe deep absorption features due to molecules such as H_2O, CO_2, CO, CH_4, CH_3OH, and NH_3. It is notable that most of the ice features are not observable by ground-based telescopes (see also Fig. 1.2). Thus, observations with satellite-borne telescopes are essential for a study of ices.

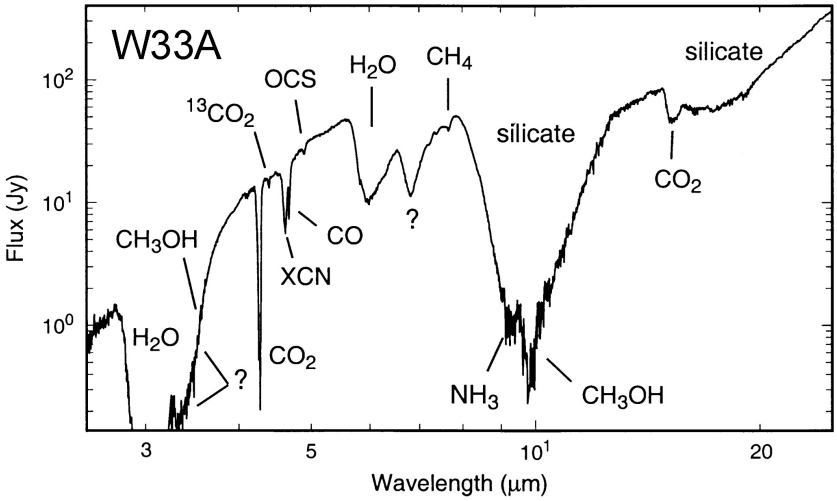

Figure 1.5 ISO IR spectrum of the Galactic young stellar object W33 A (Gibb et al. 2000).

Table 1.3 Major absorption features due to interstellar ices in the NIR and MIR.

Wavelength (μm)	Width (cm^{-1})	Molecule	Vibration mode
2.96	45	NH_3	N–H stretch
3.05	335	H_2O	O–H stretch
3.53	30	CH_3OH	C–H stretch
3.95	115.3	CH_3OH	C–H stretch
4.27	18	CO_2	^{12}C–O stretch
4.38	12.9	$^{13}CO_2$	^{13}C–O stretch
4.50	700	H_2O	$3\nu_L$ and/or $\nu_2+\nu_L$
4.62	29.1	XCN	C–N stretch
4.67	9.71	CO	^{12}C–O stretch
6.02	160	H_2O	H–O–H bend
7.70	8	CH_4	C–H deformation
8.90	34	CH_3OH	C–H_3 deformation
9.35	68	NH_3	Umbrella
9.75	29	CH_3OH	C–O stretch
13.3	240	H_2O	libration
15.3	18	CO_2	O–C–O bend

1.2.2 Formation process

It is important to consider the formation processes of ices in order to extract valuable information on the interstellar environment from the spectral features of ices. The formation processes of ices are mainly divided into two stages. In the first stage, the main reaction processes are hydrogenation of atoms, which result in an H_2O-dominated (polar) ice. In the second stage, CO condenses to the surface of dust grains and the subsequent CO-based chemistry plays important roles in the ice formation, which results in an CO-dominated (apolar) ice. As a result of these processes, ices are hierarchically formed on a dust grain as shown in Fig. 1.6. All the ices in Table 1.3 except CO ice are likely to be formed by grain surface reactions (Whittet 2003). Only for CO ice, condensation is important due to the large abundance in a gas phase ($N_{\rm CO}/N_{\rm H} \sim 3.9 \times 10^{-5}$; Herbst & Leung 1986). The formation scenario described below is mainly based on the recent observational results with Spitzer (Öberg et al. 2011).

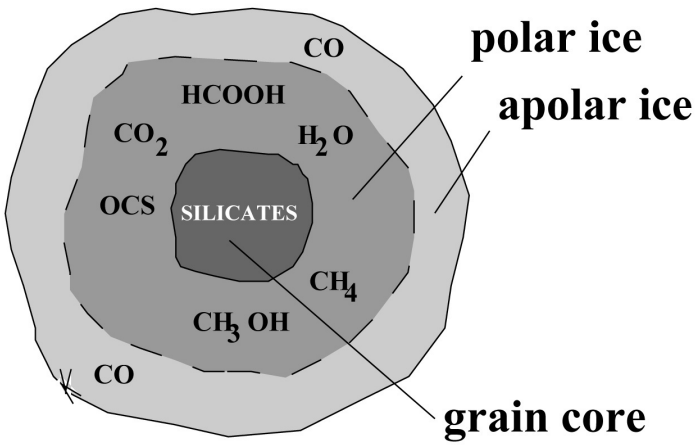

Figure 1.6 Schematic view of icy grain mantles on a dust grain (Boogert & Ehrenfreund 2004).

H_2O, CH_4, NH_3, and CO_2 ices

In early phases of the cloud formation, C, N, O, and H atoms attach to dust grains and react with H atoms, which leads to the formation of OH, CH, NH, and H_2. Whereas H_2 desorb from the grain due to the light weight, the other heavier products are kept to be attached, contributing to further reactions. In such grain surface reactions, H_2O ice is formed, which is the most abundant solid-state molecule in icy grain mantles. Tielens & Hagen (1982) proposed a chemical reaction network by which the formation of H_2O ice begins with hydrogenation of O atoms, O_2, and O_3 on the grain surfaces. Since then, possible pathways for the formation of H_2O ice have been experimentally explored under conditions at temperature as low as 10 K (e.g., Cuppen & Herbst, 2007; Miyauchi et al., 2008; Oba et al., 2010). Among them, the following chemical reactions are thought to be dominant on the surface of dust in molecular clouds (Oba et al. 2012);

$$\mathrm{OH} + \mathrm{H} \rightarrow \mathrm{H_2O} \tag{1.1}$$

$$\mathrm{OH} + \mathrm{H_2} \rightarrow \mathrm{H_2O} + \mathrm{H} \tag{1.2}$$

$$\mathrm{O_2} + \mathrm{H} \rightarrow \mathrm{HO_2} \tag{1.3}$$

$$\mathrm{HO_2} + \mathrm{H} \rightarrow \mathrm{H_2O_2} \tag{1.4}$$

$$\mathrm{H_2O_2} + \mathrm{H} \rightarrow \mathrm{H_2O} + \mathrm{OH} \tag{1.5}$$

Equation 1.1 is the simplest pathway to form H_2O ice. Cuppen & Herbst (2007) proposed that Eq. 1.1 is a main route for H_2O ice formation in diffuse and translucent clouds where H atoms are more abundant than H_2 molecule. Equation 1.2 is thought to be important in dense molecular clouds where H_2 are dominant among various H-related species. Oba et al. (2012) experimentally demonstrated that H_2O ice is actually formed by $\mathrm{OH} + \mathrm{H_2}$ at 10 K through quantum tunneling, although the reaction has a large activation energy barrier (2100 K). Equations 1.3–1.5 involve the sequential hydrogenation of O_2 molecule. Miyauchi et al. (2008) experimentally showed the processes at 10 K. While Eqs. 1.3 and 1.4 have no barrier, Eq. 1.5 has a barrier of 2000 K, which means that the reaction progresses through quantum tunneling. The detection of H_2O_2 in ρ Oph A (Bergman et al. 2011) supports that H_2O_2 is

formed through Eqs. 1.3 and 1.4, since H_2O_2 is not stable if it is formed in a gas phase.

Hydrogenation of C and N atoms produces CH_4 and NH_3 ices. These ices are thought to be important molecules in carbon- and nitrogen-related chemical networks. In particular, these ices are believed to play a key role in the formation of prebiotic molecules. Model studies predict that these ices are formed rapidly on a dust grain through hydrogenation in the early stage of a molecular cloud. Öberg et al. (2008) observationally suggested that CH_4 ice was formed through hydrogenation of a C atom in quiescent clouds based on the result that the CH_4/H_2O ratios are nearly constant (4.7 ± 1.6%) in their low-mass YSO sample. They argued that the formation mechanism depends on the initial conditions of the quiescent clouds, which seem to vary little between different star-forming regions.

CO_2 ice is the most abundant one next to H_2O ice. In terms of the formation processes, CO_2 ice is a secondary product unlike H_2O, CH_4, and NH_3 ices which are primarily formed on dust grains. The following three reactions are proposed for the formation of CO_2 ice.

$$\mathrm{CO + O \rightarrow CO_2} \tag{1.6}$$

$$\mathrm{CO + OH \rightarrow CO_2 + H} \tag{1.7}$$

$$\mathrm{H_2O + CO + h\nu \rightarrow CO_2 + 2H} \tag{1.8}$$

The first reaction (Eq. 1.6) is simple, but a large activation energy barrier of 1000 K exists (D'Hendecourt et al. 1985). Hence it is difficult to efficiently form CO_2 ice through the reaction in the cold interstellar environments ($T \sim 10$ K) without energy input. Possible reactions indicated by the recent model and experimental analyses (e.g., Garrod & Pauly, 2011; Noble et al., 2011) are the second and third ones. The second reaction is also known to have a activation energy barrier (e.g., Yu 2001). Oba et al. (2012), however, experimentally showed that CO_2 ice is formed through the reaction at 10 K, which suggests that the activation energy barrier is very small, if any. In this process, the abundance of CO_2 ice is expected to vary with dust temperature since a high dust temperature changes the mobility of the OH radical. Oba et al. (2012) reported that CO_2 ice was about 2–3 times more efficiently formed at 10 K than at 20 K through Eq. 1.7, which might be caused by competitive reactions relating to active OH radicals. The second and third reactions (Eqs. 1.7 and 1.8) are essentially the same. The difference between the reactions is the energy used in the reactions; the second reaction is a non-energetic process, while the third is an energetic one. The detailed reaction processes of Eq. 1.8 are as follows,

$$\mathrm{H_2O + h\nu \rightarrow OH^* + H,} \tag{1.9}$$

$$\mathrm{CO + OH^* \rightarrow CO_2 + H.} \tag{1.10}$$

High energy photons with an energy of >7 eV break an H-OH bond and form an internally excited OH molecule (OH^*). Watanabe & Kouchi (2002) showed that CO_2 ice is produced through these reactions based on the laboratory experiments. Comparing the energetic process with the non-energetic one, the former more easily forms CO_2 ice than the latter. Yet, based on the observational result that CO_2 ice is detected not only in YSO envelopes but also in quiescent molecular clouds where interstellar UV photons are not sufficiently supplied (Whittet et al. 1998), the non-energetic process is thought to be important as well to explain the abundance of CO_2 ice.

CO, CH_3OH, and XCN ices

In the late stage of molecular cloud formation, dust temperature decreases while gas density increases. In such a situation, ice formation processes differ from those in the early stage of cloud formation. Volatile ices, which are dominated by CO ice, are formed in this stage. It is widely known that CO molecule is the most abundant molecule after H_2 in a gas phase. In this stage, CO condenses onto dust grains from gas phase, and form CO ice. Since the sublimation temperature of CO ice is very low (16 K, Tielens 2005), CO ice mantle is mainly formed in a dense and cold molecular cloud.

CH_3OH is also an ice species which is thought to be formed in the late stage. A possible formation process of CH_3OH is hydrogenation of CO via HCO, H_2CO, and CH_3O (Tielens & Hagen 1982). Actually, H_2CO ice is detected in Galactic YSOs (e.g., Boogert et al. 2008). Since the abundance of CH_3OH ice relative to H_2O ice varies with the local interstellar environment ($< 3\%$ in the Galactic dark clouds, and 3–10% in most YSOs; Chiar et al. 1996; Brooke et al. 1999), CH_3OH ice is not a primary ice in molecular clouds. CH_3OH may be formed with subsequent processes. van der Tak et al. (2000) suggested that the abundance of CH_3OH ice depends on the gas density based on their model calculation.

The ice of an anionic molecule (OCN^-) is also observed, which is called XCN ice. The feature at 4.62 μm was for the first time observed toward the massive protostar W33A (Soifer et al. 1979), and it was later identified with a C≡N mode (Lacy et al. 1984). After these studies, Grim & Greenberg (1987) identified the molecule as OCN^-. It is experimentally known that energetic processing of several ice mixtures containing H, C, N, and O atoms produces an organic residue in which the carrier of the 4.62 μm band lies (e.g., Lacy et al., 1984; Grim & Greenberg, 1987). Alternatively, Öberg et al. (2011) suggested that XCN ice is formed from CO + NH, followed by proton transfer. Furthermore, based on the result that the abundance of XCN ice does not significantly differ between low-mass and high-mass YSOs, they suggested that UV radiation or thermal processing is not necessary to form the XCN ice. The detailed formation process of XCN ice is still unclear.

In the above descriptions of the ice formation processes, CO_2 and CO ices are formed only in polar and apolar mantle, respectively. In fact, however, CO_2 ice in an apolar mantle and CO ice in a polar mantle are also observed (e.g., Gibb et al. 2004; Pontoppidan et al. 2008), although the abundance of the ices are relatively small. Pontoppidan et al. (2008) reported that roughly $\frac{2}{3}$ of the observed CO_2 ice is present in the polar mantle for their low-mass YSO sample, while the remaining $\frac{1}{3}$ is present in the apolar mantle. CO_2 ice in the apolar mantle is thought to be formed through Eq. 1.6, where O atom is supplied from CO ice by breaking a C=O bond through an energetic process (Pontoppidan et al. 2008).

1.2.3 Implications for the interstellar environment

Considering formation processes and properties of ices, we can extract many pieces of information on the interstellar environment from the spectral features of ices. In this section, the information which we can obtain from ices is summarized.

Temperature

We can estimate the temperature of dust grains from the presence or absence of ices. This is because sublimation temperature varies among ice species. Table 1.4 summarizes the sublimation temperatures

Table 1.4 Sublimation temperatures of pure ices.

Molecule	Sublimation temperature
H_2O	90
CH_4	18
NH_3	55
CO_2	50
CO	16
CH_3OH	80

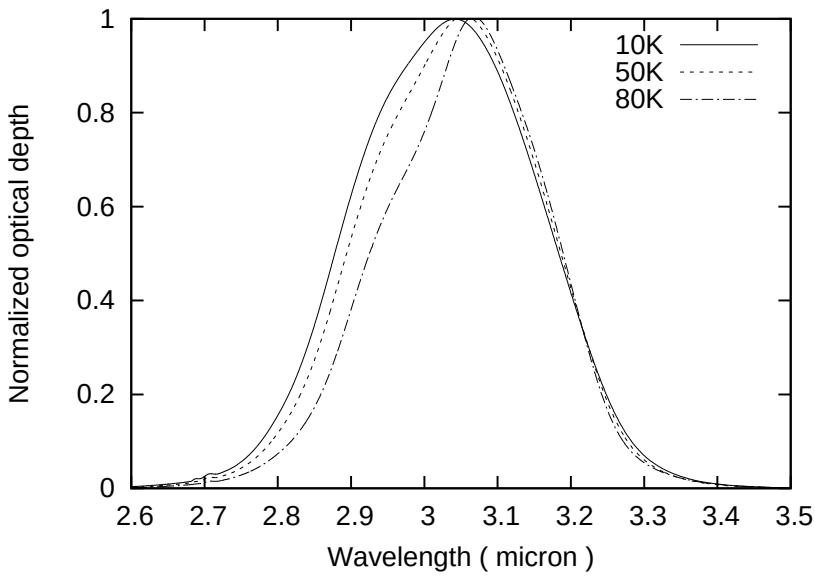

Figure 1.7 Variation of absorption profiles of H_2O ice at 3.05 μm at temperatures of 10, 50, and 80 K (Öberg et al. 2007).

of the pure ices described in the previous section (Tielens 2005). In the table, CO ice has the lowest sublimation temperature, while H_2O ice has the highest one. These temperatures suggest that CO ice is formed deeper inside the molecular clouds than H_2O ice. Here it is notable that a sublimation temperature of ice mixture is different from that of a pure ice; for example, CO ice trapped in polar mantle does not evaporate even at much higher temperatures than the sublimation temperature of the pure CO ice (Tielens et al. 1991).

A spectral profile of each absorption feature also has information on temperature. Thanks to laboratory experiments, it has been found that the position, width, and shape of absorption features are sensitive to temperature of the ice mantle (e.g., Ehrenfreund et al. 1996). Figure 1.7 shows an example of variations in the absorption profile of H_2O ice between 10 K and 80 K (Öberg et al. 2007). The figure clearly indicates that the spectral absorption profiles are different depending on its temperature and that H_2O ice at a higher temperature shows a sharper absorption profile.

Chemistry

Ices also provide information on the interstellar chemistry. As shown in the previous section, ice mantles actually consist of multiple layers and mixture of some molecular species. Hence, the chemical composition of the ice mantle changes the spectral absorption profile, in which the ice formation history is reflected. Figure 1.8 shows variations of absorption profiles of CO_2 ice with three different chemical

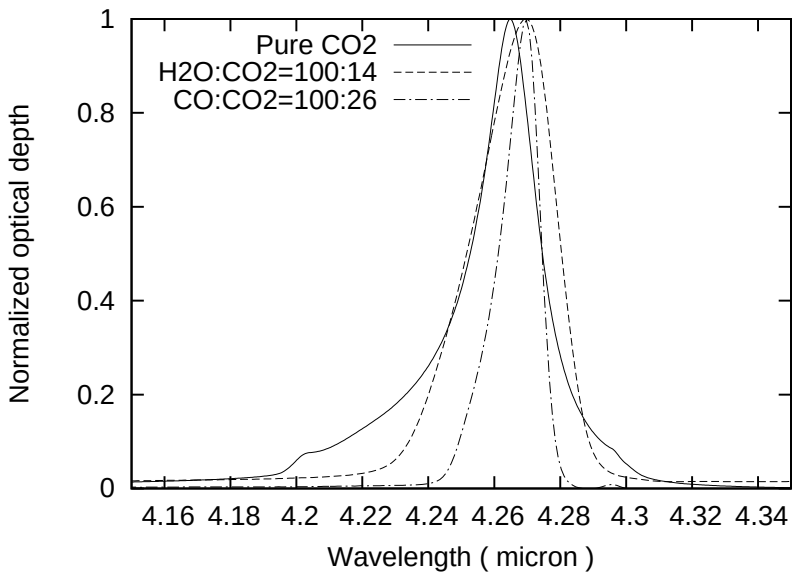

Figure 1.8 Variation of absorption profiles of CO_2 ice at 4.27 μm (Ehrenfreund et al. 1996).

compositions. The profiles are slightly different from composition to composition.

Recently, Shimonishi et al. (2010) showed that CO_2/H_2O ice abundance ratios are significantly different between YSOs in the LMC (0.36±0.09) and those in our Galaxy (0.17±0.03; Gerakines et al. 1999). The LMC has a unique environment in terms of metallicity; the interstellar metallicity in the LMC is $Z \sim 0.3\ Z_{\odot}$ (Luck et al 1998). Then they suggested that the strong UV radiation field and/or the high dust temperature in the LMC due to low metallicity are responsible for the observed high abundance of CO_2 ice.

Radiation field

We can also use ices as probes of the radiation environment. As described in the previous section, UV radiation may be needed to produce CO_2 and XCN ices. Therefore, the abundances of CO_2 and XCN ices relative to H_2O ice may be useful probes of the radiation environment within a molecular cloud. The abundances of ices may also depend on the interstellar radiation field from outside of molecular clouds. If significant UV photons are supplied from nearby stars around a molecular cloud, the dust temperature increases with the radiation field, which suppresses the ice formation near the surface of molecular clouds. Hence the abundances of ices may be sensitive to the intensity and hardness of the interstellar radiation field.

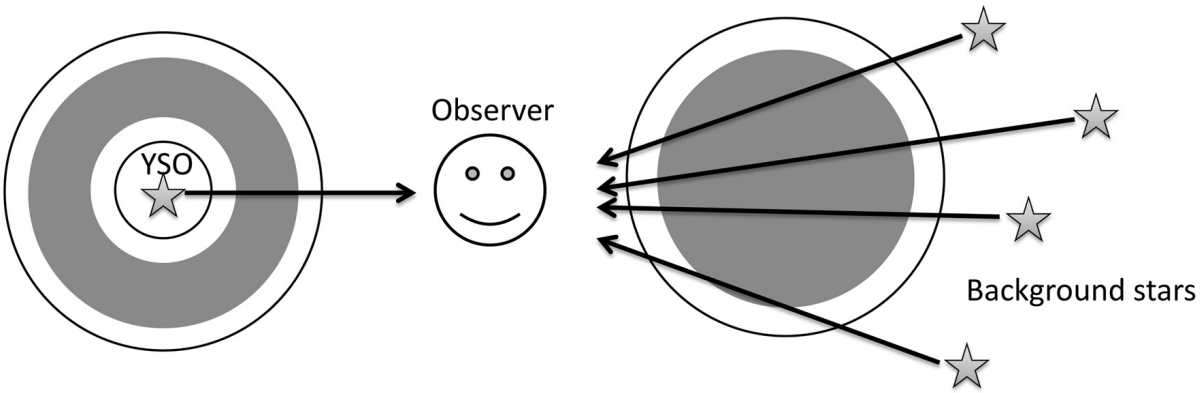

Figure 1.9 Two observational situations of interstellar ices. The regions where ices are present are shown in gray.

1.3 Past studies of ices in Galactic sources

It was 40 years ago that the interstellar H_2O ice was detected in the ISM for the first time (Gillett & Forrest 1973). In such early times, ices were observed by using ground-based telescopes with the spectral windows of the L and M bands. In the ISO and Spitzer era, continuous spectra were obtained covering the ice features in the NIR and MIR, which further advanced the study of ices. Since the first detection, ices have been detected in many Galactic sources, such as low-mass YSOs, high-mass YSOs, Galactic center (Sgr A*), and field stars behind quiescent dark clouds. The observations of ices are mainly categorized into two types based on the continuum emitter; YSOs and background stars (Fig. 1.9). In the former case, we observe ices around YSOs, where not only the properties of the original molecular cloud but also the local environment due to YSOs may affect the abundances of ices. In the latter case, we observe the variations of the column densities of ices by using multiple background stars. The observation of Sgr A* (Gerakines et al. 1999) is categorized into the latter case. Observations of background stars provide us with information on the overall cloud environment.

More than 50 Galactic YSOs have been intensively studied in the ice features to date. An example of the YSO spectra obtained with ISO is already shown in Fig. 1.5 (Gibb et al. 2000). Thanks to the high spectral resolution and intensive efforts of laboratory experiments (e.g., Ehrenfreund et al. 1996), it was revealed that the ices are hierarchically formed as already described in Section 1.2.2 and Fig. 1.6 (Boogert et al. 2008; Pontoppidan et al. 2008; Öberg et al. 2008; Bottinelli et al. 2010; Öberg et al. 2011), and that the spectral absorption profiles change significantly from source to source (Fig. 1.7), suggesting variations in the ice-forming environment. Figure 1.10 shows differences in the absorption profiles of the CO and CO_2 ices between three YSOs, the evolutionary stages of which are expected to be different. In the figure, NGC 7538 IRS1 shows a clear absorption feature due to CO ice, while GL 4176 does not. It is likely that the CO ice toward W3 IRS5 and GL 4176 is partially and completely sublimated, respectively, due to high dust temperature. On the other hand, the CO_2 ice feature is seen in all the spectra, presumably because the sublimation temperature of CO_2 ice is higher than that of CO ice (Table 1.4).

Studies of ices with observations of background stars are not fully performed yet since observational targets are limited due to the geometry of molecular clouds and stars. Such studies are performed only

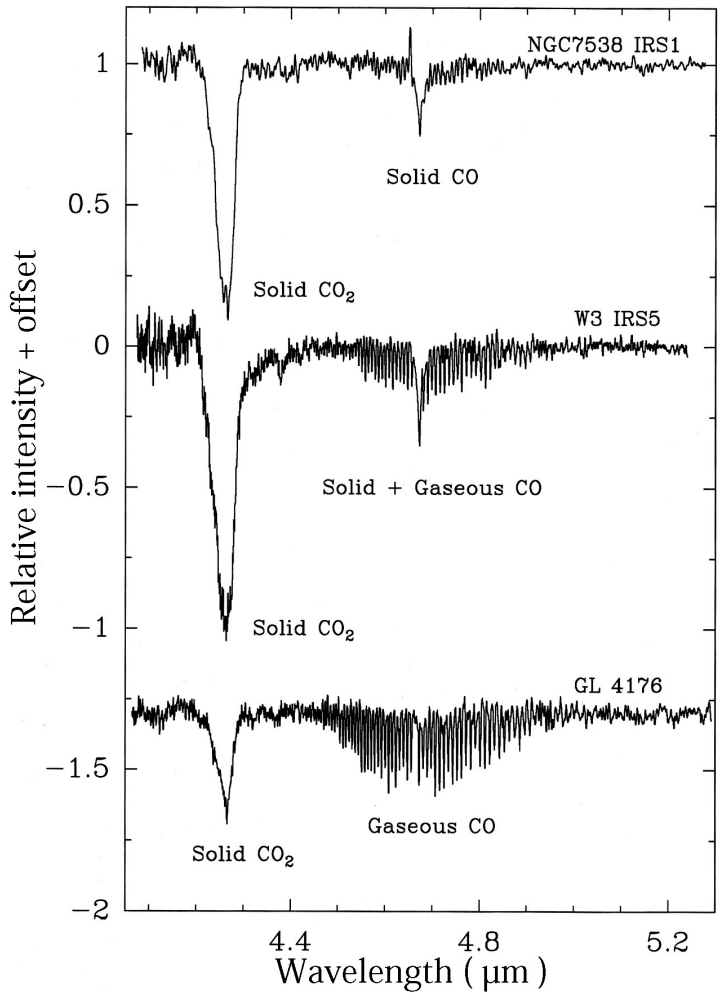

Figure 1.10 ISO IR spectra of three Galactic YSOs in different evolutionary stages (Whittet 2003)

for Taurus, IC 5146, Serpens, Lupus, and ρ Oph clouds to date (e.g., Whittet et al. 1988, 2007; Chiar et al. 2011; Eiroa & Hodapp 1989; Tanaka et al. 1990; Boogert et al. 2013). An example of spectra obtained from the K-type star Elias 16 toward the Taurus dark cloud is shown in Fig. 1.11 (Whittet et al. 1998). The spectrum clearly shows absorption features due to H_2O, CO_2, and CO ices. A K-type star itself does not show such ice features. Therefore the ice features are likely to originate from the foreground Taurus dark cloud.

Important information on the interstellar environment taken from observations of background stars is the relation between the column densities of ices and interstellar extinction in a line of sight (A_V). The relations in the Taurus molecular cloud are well represented by the following equations (Whittet et al. 1988, 2007):

$$N_{H_2O} = 13.0 \times 10^{16}(A_V - 3.2) \quad [\mathrm{cm}^{-2}], \tag{1.11}$$

$$N_{CO_2} = 2.52 \times 10^{16}(A_V - 4.3) \quad [\mathrm{cm}^{-2}], \tag{1.12}$$

$$N_{CO} = 4 \times 10^{16}(A_V - 6.7) \quad [\mathrm{cm}^{-2}], \tag{1.13}$$

where A_V given in units of magnitude and the column densities of the ices (N_{H_2O}, N_{CO_2}, and N_{CO}) are evaluated from the observations of the background stars toward the cloud. These relations indicate that

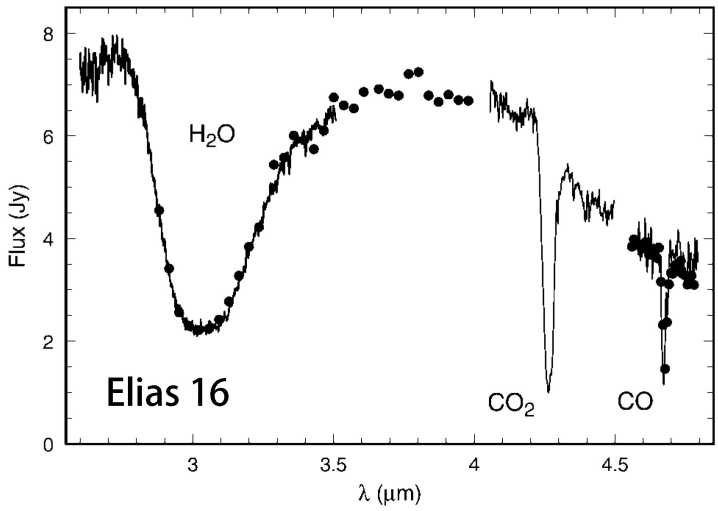

Figure 1.11 NIR spectrum of Elias 16 obtained with the ISO/SWS (solid curves) and ground-based telescope (filled circles; Whittet et al. 1998).

Table 1.5 Relative abundances of ices in three Galactic objects

Molecule	high-mass YSO (W33A)	low-mass YSO (Elias 29)	Dark cloud (Elias 16)
H_2O	100	100	100
CO_2	13	20	24
CO	8	5	25
XCN	6	<0.2	<1.5
NH_3	15	<7	<10
CH_3OH	17	<4	<3

the ices exist deeper inside the cloud than the extinction threshold (H_2O: 3.2 mag; CO_2: 4.3 mag; CO: 6.7 mag). The high extinction threshold of CO ice probably reflects the low sublimation temperature of CO ice (Table 1.4). It is known that the extinction threshold shows significant variations from region to region. For example, the extinction thresholds of H_2O ice in Serpens and ρ Oph are ~5.5 mag and 10–15 mag, respectively (Eiroa & Hodapp 1989; Tanaka et al. 1990), which are considerably higher than the threshold in Taurus. These variations are likely to be governed by the interstellar UV radiation environment; Taurus is a low-mass star forming region without massive stars, while ρ Oph is located close to an OB association.

Table 1.5 shows the relative abundances of ices for three types of objects in our Galaxy, high-mass YSO, low-mass YSO, and dark cloud (Gibb et al. 2004). Since H_2O ice is the most abundant ice, the abundance of each ice is generally defined as a ratio of the column density of the ice to that of H_2O ice. As shown in Table 1.5, the abundances of ices are different from region to region; in massive YSOs, ices are heavily processed while in the others are not. The differences in Table 1.5 may reflect those in the ice-forming interstellar environment. Among the parameters, it may be worth referring to the difference in the CO_2/H_2O ice abundance ratio for low-mass and high-mass YSOs. CO_2/H_2O ice abundance ratios for high-mass and low-mass YSOs are 0.17±0.02 and 0.32±0.02, respectively (Gerakines et al. 1999; Pontoppidan et al. 2008). Pontoppidan et al. (2008) proposed that a new formation process for CO_2 ice may be activated around the low-mass YSOs. However, the origin of the high ratios has not been clarified yet.

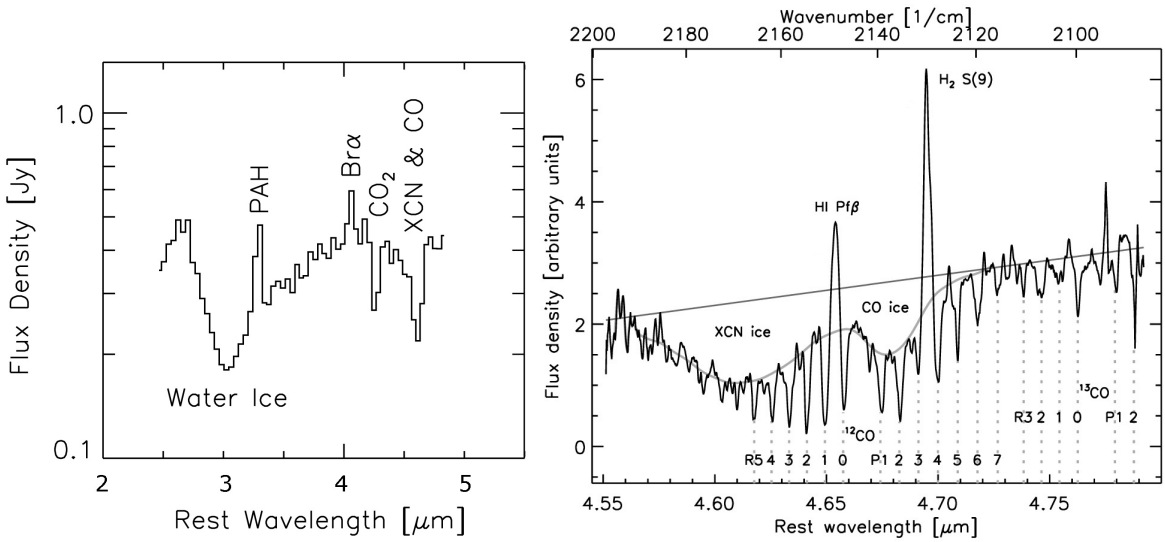

Figure 1.12 NIR and MIR spectra of the nearby galaxy NGC 4945 (Spoon et al. 2000, 2003). (left) ISO/PHT-S spectrum for the central $24'' \times 24''$ (430×430 pc^2) region of NGC 4945. (right) VLT/ISAAC M band spectrum of the central $2'' \times 1''$ (36×18 pc^2) of NGC 4945.

1.4 Ices in nearby galaxies

Interstellar ices in nearby galaxies have been detected in several past studies since about 10 years ago. Huge differences between galactic sources and nearby galaxies lie in spatial scales of observations. In the case of Galactic sources, targets are spatially well resolved, and the geometry of a continuum emitter and absorber is relatively clear. In the case of nearby galaxies, however, observed spectra have information only for a wide area ($\gtrsim 100 \times 100$ pc^2), and the geometry of a continuum emitter and absorber is not clear in a line of sight. The effects originating in the difference have not yet been intensively studied.

It was the ISO satellite that initiated the studies of ices in nearby galaxies. An intensive study of ices in nearby galaxies was performed by Spoon et al. (2000, 2003) (Fig 1.12). They observed the nearby dusty starburst/AGN galaxy NGC 4945 with the ISO/PHT-S, and reported the detection of H_2O, CO_2, XCN, and CO ices in the central region, for the first time in extragalactic sources (Spoon et al. 2000). After the report, they performed the spatially-resolved follow-up observations in the L and M bands with VLT (Spoon et al. 2003). As a result, they clearly detected XCN ice and polar CO ice. Since the ices are widely extended in the observed regions, they conclude that the processing of the ices is induced not by AGN activity but by on-going massive star formation.

With ISO, Spitzer, and AKARI, detections of ices in NIR and MIR spectra have been reported by many authors, although the main topics of the studies do not necessarily focus on ices. In a field of nearby galaxies, Sturm et al. (2000) observed four nearby galaxies (NGC 253, NGC 1068, M 82, and Circinus) with the ISO/SWS, and detected H_2O ice at 3.05 μm in M 82 and NGC 253 (Fig. 1.13). With the ISO/PHT-S, Spoon et al. (2002) systematically searched H_2O ice at 6 μm in galactic nuclei. As a result, they found that the ice is detected for a substantial fraction of ULIRGs (12 out of 19) and the minority of Seyfert (2 out of 62) and starburst (4 out of 21) galaxies (Fig. 1.14). With the AKARI NIR slit-less spectroscopy, Imanishi et al. (2010) observed 114 (U)LIRGs at $z = 0 - 0.4$ and studied the PAH 3.3 μm feature in AGNs. In their spectra, H_2O ice at 3.05 μm and CO_2 ice at 4.27 μm are detected in

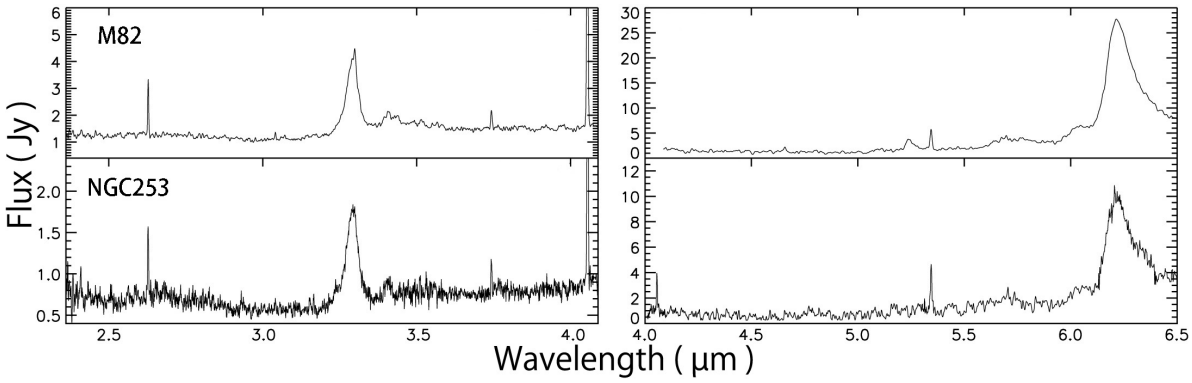

Figure 1.13 NIR spectra of the nearby galaxies M 82 and NGC 253 taken with the ISO/SWS (Sturm et al. 2000). The optical depths of H_2O ice in M 82 and NGC 253 are estimated to be 0.2 and 0.25, respectively.

35 and 20 (U)LIRGs, respectively. Sources with detection of CO_2 ice often accompany clear detection of H_2O ice, supporting the formation scenario for CO_2 ice through the photolysis of ice-covered dust grains. Furthermore with the AKARI NIR slit-less spectroscopy, Yamada et al. (2013) systematically analyzed the NIR spectra for 184 star forming galaxies and AGNs including those of in Imanishi et al. (2010), and investigated a global relation between the PAH 3.3 μm emission and total infrared luminosity. As a result, they detected H_2O ice at 3.0 μm from 108 galaxies out of 184 galaxies, although they did not discuss the presence or absence of CO_2 ice at 4.27 μm. Ices are also detected in more distant galaxies. Sajina et al. (2009) observed 7 ULIRGs at $z \sim 2$ with the Spitzer/IRS, and detected H_2O ice at 3.05 μm in 3 galaxies. They found that ratios of the optical depth of H_2O ice to that of silicate absorption feature ($\tau_{\mathrm{H_2Oice}}/\tau_{\mathrm{silicate}}$) in the galaxies are not significantly different from those of YSOs in our Galaxy, suggesting similarity in the ice mantle thickness relative to the size of a dust grain.

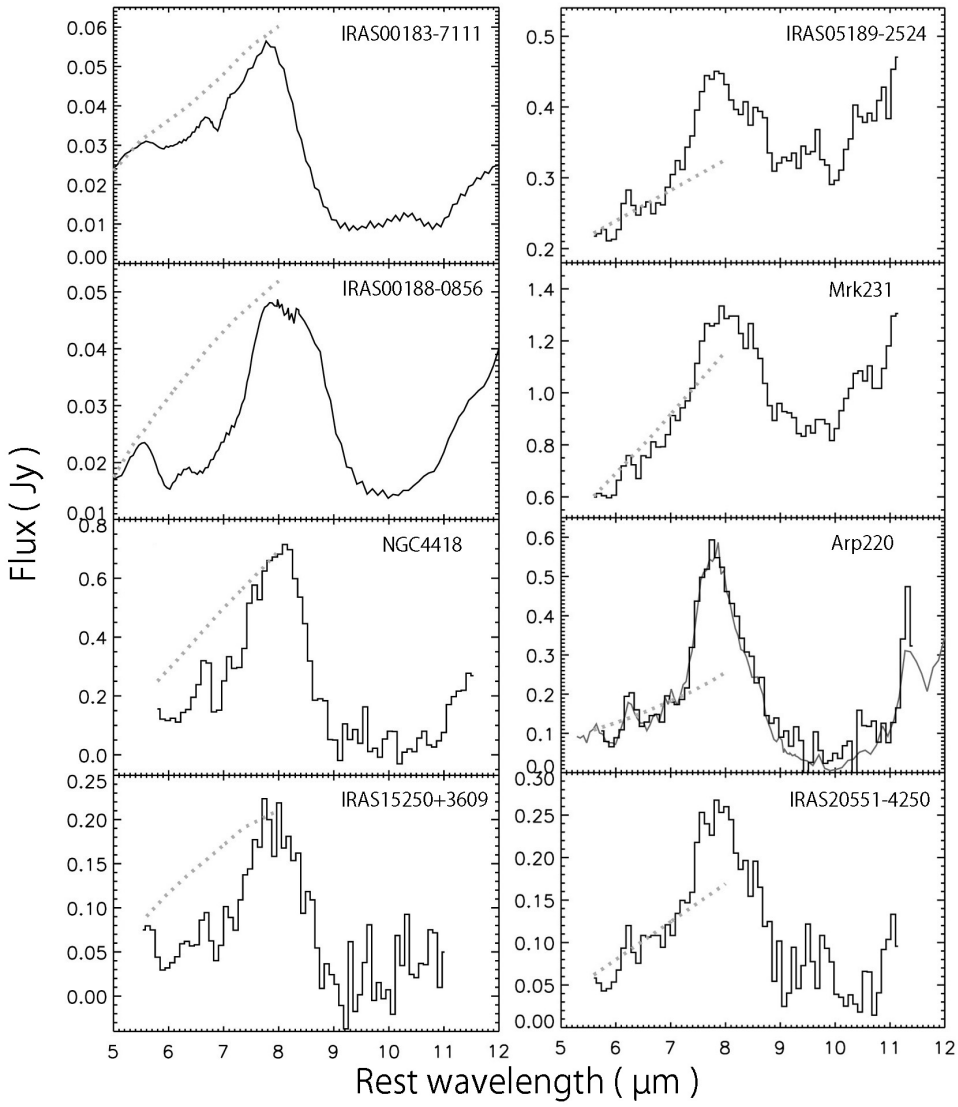

Figure 1.14 Examples of the spectra which show H_2O ice at 6.0 μm (Spoon et al. 2002). The dotted lines in 5.5–8.0 μm indicate the continuum levels adopted for estimating the strength of the absorption feature.

1.5 Purpose of this thesis

Interstellar ices have been widely detected even from nearby galaxies. In the past studies, however, ice features have not been fully utilized as probes of the interstellar environment. Furthermore, multiple ice features were not substantially discussed together due to the limit of the wavelength coverage and sensitivity of the instruments. As mentioned in the previous section, ratios of the column densities of ices, particularly those of H_2O ice to CO_2 ice, are important to utilize the ice features. Additionally, spatial information on ices in a galaxy is still unclear. This is because the spatial resolutions of the instruments are not high enough to resolve nearby galaxies. For example, the beam sizes of the ISO/SWS and ISO/PHT-S are $14'' \times 20''$ and $24'' \times 24''$, respectively.

The goal of this thesis is to overcome the difficulties which the past studies encountered, and to establish ices as probes of the interstellar environment. In order to achieve this goal, the datasets of 158 nearby galaxies obtained with the AKARI NIR slit spectroscopic observations are systematically analyzed, which are the most extensive NIR spectroscopic survey of nearby galaxies. The advantages of the AKARI slit spectroscopy compared to the previous spectroscopy with ISO and Spitzer are high sensitivity and high spatial resolution in the NIR. Among the ice features in the NIR, H_2O and CO_2 ices are focused on, which show prominent features as clearly shown in Figs. 1.1 and 1.5. Utilizing both statistical and spatial information on the ices and the other emission features in the NIR spectra, the relations are investigated between the abundances of the ices and the interstellar environment in a galaxy.

In chapter 2, details of the observations with AKARI and spectral analysis methods are described. In the former half of chapter 3, the result of the search for the ices in 158 nearby galaxies are described. The characteristics of the regions with detection of the ices and essential parameters to determine the abundances of the ices are statistically examined based on the results obtained from all the sample galaxies. In the latter half of chapter 3, spatial distributions of the ices and their connection with the interstellar environment are examined for particular galaxies (NGC 253, M 82, and NGC 1097). In chapter 4, discussions are made about the applicability of the ices as probes of the interstellar environment, and the effects originating in the differences between galactic and extragalactic observations. Finally, a summary is given in chapter 5.

Chapter 2

Observations and data analysis

2.1 AKARI near-infrared spectroscopy

AKARI is a Japan-led infrared astronomy satellite, which was launched on 21 February 2006 (Murakami et al. 2007). The diameter of the telescope is 71 cm. AKARI has two focal-plane instruments, the IRC (infrared camera; Onaka et al. 2007) and the FIS (far-infrared surveyor; Kawada et al. 2007), which cover the wavelength ranges of 2–27 and 50–180 μm, respectively. In space IR observations, it is important to achieve low photon background levels. Therefore, in order to reduce the thermal radiation, the whole telescope system including the instruments is cooled down to 6 K by liquid helium, which enables us to detect faint IR emission from various objects with high sensitivity. AKARI was put into a sun-synchronous polar orbit at an altitude of about 700 km, and flew along the day-night border with an orbital period of about 100 min. During 1.5 years after the launch, all-sky observations in the 6 photometric bands at wavelengths of 9, 18, 65, 90, 140, and 160 μm were performed as well as pointed imaging and spectroscopic observations at 2–180 μm (Phases 1 and 2). After the boil-off of liquid helium in August 2007, only the NIR (2–5 μm) imaging and spectroscopic observations were performed while the temperature of the telescope was kept at $\sim$ 40 K by using mechanical coolers (Phase 3).

The AKARI/IRC consists of the NIR, MIR-S, and MIR-L channels which cover 2–5, 6–13, and 13–27 μm ranges, respectively (Onaka et al. 2007). Each channel has a capability of performing both imaging and spectroscopic observations. In this study, a grism spectroscopic mode in the NIR channel was used to obtain 2.5–5.0 μm spectra, which has a spectral resolution of $R \sim$120 and two slits ($5'' \times 37''$ for Ns and $3'' \times 44''$ for Nh; Ohyama et al. 2007). Figure 2.1 shows the field-of-view location of the IRC NIR channel, where one pixel corresponds to the angular scale of $1\farcs46$ (Onaka et al. 2007). The grism mode spatially disperses the whole IR light in the upward direction in Fig. 2.1. Thanks to the masked regions on the top and bottom sides of the slits, we can extract dispersed spectra of the slit apertures without overlapping with those of other objects. Since there are two slits located $2'$ away from each other, two independently dispersed images are obtained simultaneously. If the signal-to-noise ratios (S/Ns) of a spectrum are high enough, it is possible to divide the slit aperture into sub-aperture areas and extract multiple spectra along the slit. This merit enables us to discuss spatial variations of spectral features within a slit aperture. An example of observed images is shown in Fig. 2.2, in which the nearby galaxy IC 3370 is observed by using the Ns slit. The observational sequence of a spectroscopic observation is shown in Fig. 2.3. One pointed observation takes about 30 minutes (10 minutes for an observing time

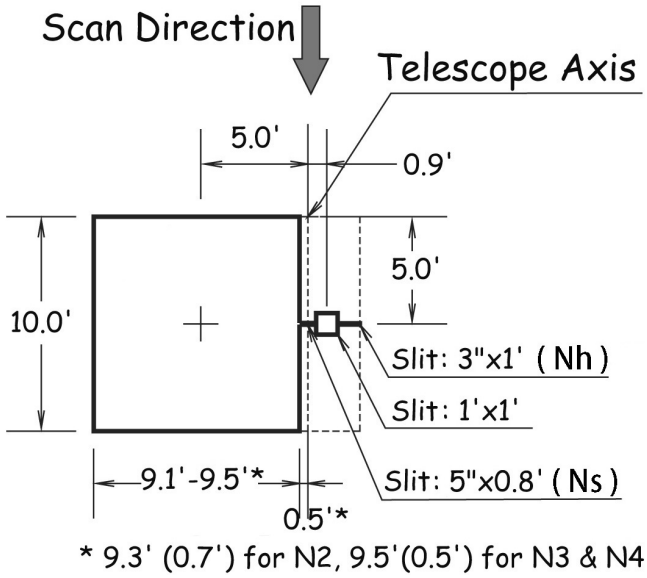

Figure 2.1 Field-of-view location of the IRC NIR channel (Onaka et al. 2007). The vertical arrow indicates the scan direction in the survey mode.

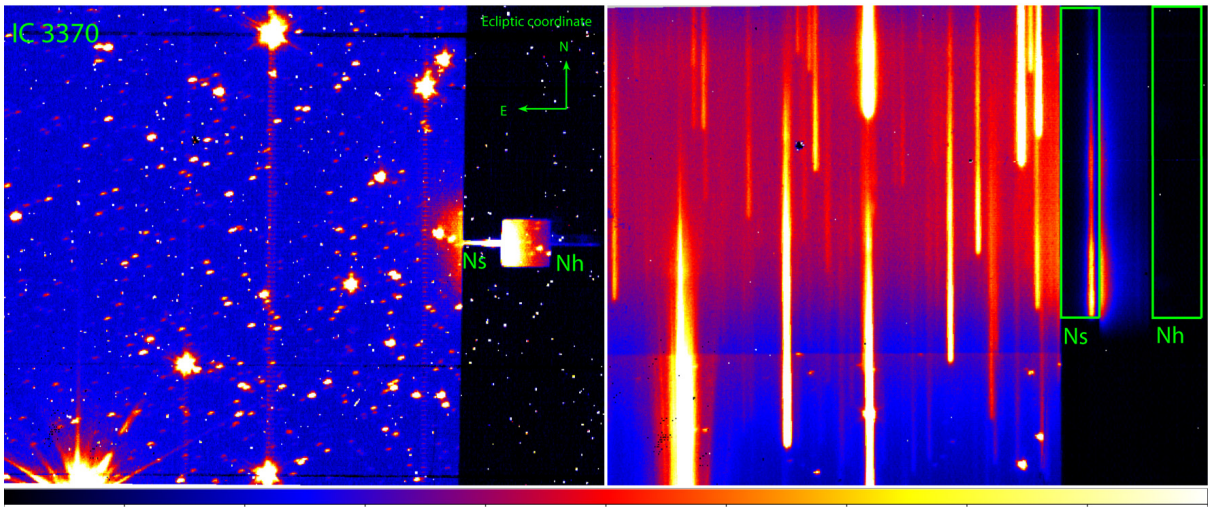

Figure 2.2 Field-of-view (left) and dispersed (right) images for the nearby galaxy IC 3370. The positions of the Ns and Nh slits are indicated. The regions from which we can extract spectra are also indicated with the boxes in the right panel.

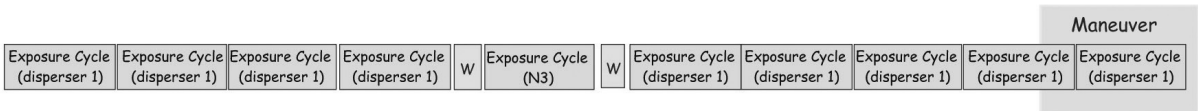

Figure 2.3 Observational sequence of a spectroscopic observation (Onaka et al. 2007). The boxes labeled as "Exposure cycle" and "W" indicate exposure frames and filter wheel rotations, respectively. The shaded area on the right side is an extra observation time.

and 20 minutes for a maneuvering time), in which 7–9 exposure frames are taken. In between the fourth and fifth exposures, a field-of-view image in the 3 μm band is observed, which is used to confirm the observational position.

2.2 Targets

With AKARI NIR slit spectroscopy, 411 pointed observations (19 in Phase 2 and 392 in Phase 3) were performed for 158 nearby galaxies ($z < 0.03$). However all the spectral data are not independent. This is because observers were officially required to observe the same target more than once in Phase 3 since the data quality in Phase 3 is worse than that in Phase 2 due to increase in the number of hot pixels. The hot pixels are defined as pixels which show significantly ($> 3\sigma$) higher signals than the average in a dark image. Figures 2.4 (a) and (b) show time variation in temperature of the AKARI/NIR detector and the fraction of hot pixels, respectively. In Phase 3, the temperature of the NIR detector was increasing slowly as well as the number of hot pixels. In multiple observations, insufficient pointing accuracy of AKARI ($< 30''$) poses a problem; the observed positions can be slightly different from observation to observation even if the intended target positions are the same. In this study, if the observed area of one pointing overlaps with that of another pointing, only one of the areas was analyzed, unless otherwise stated in Table 2.1. As a result, independent 280 observed data were analyzed in this thesis.

In the NIR slit spectroscopy, a targeted region was observed by either Ns or Nh slit. Since observations are simultaneously performed in the Ns and Nh slits, it is possible to detect signals from the other slit, if a target galaxy is extended by an angular size larger than $2'$. In order to judge whether the other slit observed the same galaxy or not, the optical diameter (D_{25}) and the position angle of each galaxy (de Vaucouleurs et al. 1991) were taken into account. If the targeted galaxy was covered by the other slit, spectra were also extracted from the other slit. Finally, 369 slit positions in 158 galaxies are analyzed. The observed galaxies and regions are summarized in Table. 2.1.

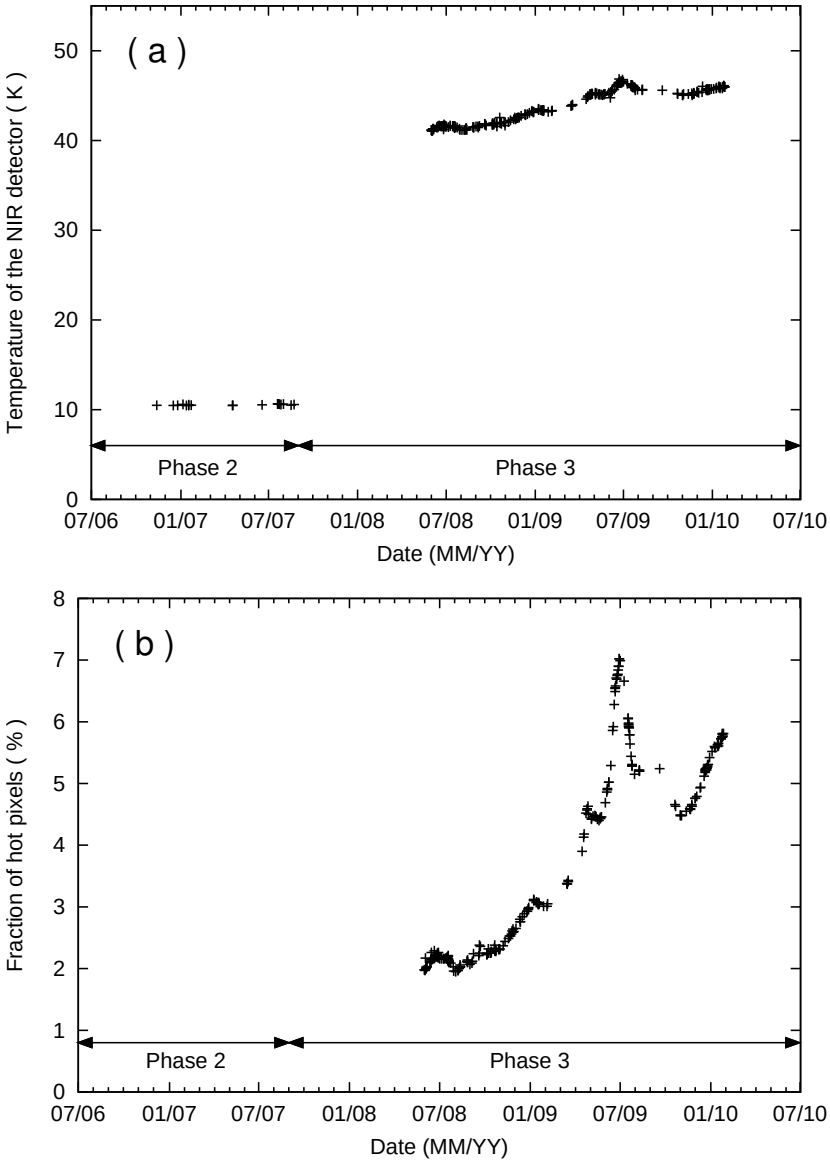

Figure 2.4 Time variation in (a) temperature of the AKARI/NIR detector and (b) the fraction of hot pixels. The number of hot pixels in Phase 2 is negligible.

Table 2.1 Summary of the NIR spectroscopic observations

Obs. ID[a]	Target name	Redshift[b]	Type[b,c]	Obs. date	RA, DEC[d], $N_{\rm sub}$[e] (Ns)			RA, DEC[d], $N_{\rm sub}$[e] (Nh)		
1422195.1	Cen A	0.0018	L	26/01/2010	201.3664 ,	-43.0227	8	201.3285 ,	-43.0093	2
1420103.1	Cen A	0.0018	L	29/07/2008	201.3680 ,	-43.0183	5	201.4060 ,	-43.0318	2
1420104.1	Cen B	0.0122	?	12/08/2008	206.7066 ,	-60.4059	3			
1420105.1	Cen B	0.0122	?	13/08/2008	206.7066 ,	-60.4063	3			
5125033.1	Circinus	0.0014	S	23/08/2007	213.2865 ,	-65.3383	8			
1420387.1	ESO 034-11	0.0223	S	26/08/2008	100.7851 ,	-74.2270	2			
5200013.1	ESO 244-12	0.0228	S	14/06/2008				19.5321 ,	-44.4663	2
5200013.2	ESO 244-12	0.0228	S	14/06/2008				19.5323 ,	-44.4634	2
5200011.1	ESO 264-36	0.0236	S	27/06/2008				160.7873 ,	-46.2152	2
1420395.1	ESO 350-38	0.0210	I	14/06/2008	9.2207 ,	-33.5581	2			
1420363.1	ESO 495-21	0.0029	I	11/11/2008	129.0644 ,	-26.4128	2			
1422158.1	ESO 495-21	0.0029	I	13/11/2009	129.0651 ,	-26.4119	3			
3221004.1	HCG 15e	0.0240	L	24/07/2007	31.8564 ,	2.1181	2			
1422151.1	IC 0010	-0.0012	I	25/01/2010	5.0676 ,	59.3039	2	5.1159 ,	59.3224	2
1422651.1	IC 0010	-0.0012	I	25/01/2010	5.1055 ,	59.2939	2	5.1537 ,	59.3124	2
1420094.1	IC 1459	0.0056	E	22/11/2008	344.2910 ,	-36.4621	6	344.3258 ,	-36.4490	2
1420095.1	IC 1459	0.0056	E	20/05/2009	344.2958 ,	-36.4639	3	344.2611 ,	-36.4771	2
5200015.1	IC 1623	0.0205	S	29/06/2008				16.9464 ,	-17.5096	2
1422157.1	IC 3258	-0.0015	I	22/12/2009	185.9346 ,	12.4763	2			
1400056.1	IC 3370	0.0098	E	13/01/2007	186.9099 ,	-39.3389	4			
1420375.1	IC 4662	0.0011	I	20/09/2008	266.7614 ,	-64.6199	2			
1420376.1	IC 4662	0.0011	I	20/09/2008	266.7826 ,	-64.6363	2			
1420380.1	IC 4870	0.0028	I	05/10/2008	294.3990 ,	-65.8113	2			
1420299.1	IIZw 40	0.0027	I	19/03/2009	88.9246 ,	3.3944	2			
1420399.1	IIZw 40	0.0027	I	20/09/2009	88.9307 ,	3.3906	2			
5125002.1	M 031	-0.0010	S	20/07/2007	10.2485 ,	41.0602	2			
1420001.1	M 031	-0.0010	S	18/07/2008	10.3470 ,	41.1807	2	10.3104 ,	41.1668	2
1420002.1	M 031	-0.0010	S	17/01/2009	10.3588 ,	41.2070	2	10.3953 ,	41.2211	2
1422222.1	M 031	-0.0010	S	17/01/2010	10.5002 ,	41.0734	3	10.5367 ,	41.0873	3
1420044.1	M 031	-0.0010	S	20/07/2009	10.5067 ,	41.0717	6	10.4703 ,	41.0576	6
1420023.1	M 031	-0.0010	S	19/07/2009	10.6054 ,	41.2652	8	10.5688 ,	41.2511	6
1420028.1	M 031	-0.0010	S	19/07/2008	10.6057 ,	41.2568	6	10.5691 ,	41.2428	3
1420018.1	M 031	-0.0010	S	19/07/2008	10.6059 ,	41.2744	6	10.5693 ,	41.2604	3
1420042.1	M 031	-0.0010	S	18/01/2009	10.6388 ,	40.9656	8			
1420017.1	M 031	-0.0010	S	18/01/2009	10.6635 ,	41.2747	3	10.6998 ,	41.2889	3
1420022.1	M 031	-0.0010	S	19/07/2008	10.6682 ,	41.2654	6	10.6317 ,	41.2513	6
1420027.1	M 031	-0.0010	S	20/07/2009	10.6692 ,	41.2564	5	10.6327 ,	41.2423	3
5125003.1	M 031	-0.0010	S	21/07/2007	10.6863 ,	41.2708	6	10.6500 ,	41.2565	3
1420047.1	M 031	-0.0010	S	19/07/2008	10.6889 ,	41.1408	2	10.6524 ,	41.1268	2
1420007.1	M 031	-0.0010	S	19/07/2008	10.6978 ,	41.5640	2			
1420041.1	M 031	-0.0010	S	19/07/2008	10.7235 ,	41.0366	2	10.6870 ,	41.0227	2
1420021.1	M 031	-0.0010	S	18/01/2009	10.7262 ,	41.2676	2	10.7627 ,	41.2819	2
1420026.1	M 031	-0.0010	S	19/07/2008	10.7300 ,	41.2568	2	10.6935 ,	41.2428	2
1420016.1	M 031	-0.0010	S	19/07/2008	10.7311 ,	41.2734	2	10.6949 ,	41.2594	2
1420008.1	M 031	-0.0010	S	17/01/2009	10.7542 ,	41.4426	2	10.7908 ,	41.4568	2
1422228.1	M 031	-0.0010	S	17/01/2010	10.7967 ,	41.4217	3	10.8332 ,	41.4357	3
1420052.1	M 031	-0.0010	S	21/07/2009	10.8019 ,	41.4201	3	10.7655 ,	41.4059	3
1420048.1	M 031	-0.0010	S	18/01/2009	10.8053 ,	41.3107	2	10.8419 ,	41.3249	2
1420039.1	M 031	-0.0010	S	18/01/2009	10.8386 ,	41.1137	2	10.8749 ,	41.1278	2
1420049.1	M 031	-0.0010	S	21/07/2009	10.8654 ,	41.3855	2	10.8290 ,	41.3713	2
1420038.1	M 031	-0.0010	S	20/07/2008	10.8943 ,	41.1618	2	10.8579 ,	41.1476	3
1420036.1	M 031	-0.0010	S	18/01/2009	10.9837 ,	41.2472	3			
1420035.1	M 031	-0.0010	S	20/07/2008	11.0186 ,	41.2869	8	10.9822 ,	41.2728	6
5125004.1	M 031	-0.0010	S	22/07/2007	11.1619 ,	41.7059	3			
5200824.1	M 032	-0.0007	E	19/07/2009	10.7085 ,	40.8772	2	10.6721 ,	40.8633	4
1400388.1	M 051	0.0016	S	17/12/2006	202.4533 ,	47.2257	3			
1420472.1	M 058	0.0050	S	25/06/2009	189.4074 ,	11.8308	2	189.4361 ,	11.8180	3

Table 2.1 Continued

Obs. ID[a]	Target name	Redshift[b]	Type[b,c]	Obs. date	RA, DEC[d], N_{sub}[e] (Ns)		RA, DEC[d], N_{sub}[e] (Nh)	
1422170.1	M 058	0.0050	S	25/12/2009	189.4310 , 11.8165	3	189.4023 , 11.8293	2
5200845.1	M 061	0.0052	S	24/06/2009	185.4808 , 4.4743	3		
1422178.1	M 063	0.0017	S	19/12/2009	198.9561 , 42.0274	4	198.9209 , 42.0438	2
1422176.1	M 064	0.0013	S	26/12/2009	194.1728 , 21.6855	4	194.1429 , 21.6987	2
1422173.1	M 064	0.0013	S	26/12/2009	194.1821 , 21.6797	3	194.1522 , 21.6930	2
1420435.1	M 066	0.0023	S	06/06/2008	170.0641 , 12.9930	6		
5125030.1	M 077	0.0038	S	01/08/2007	40.6714 , -0.0125	8	40.6421 , -0.0218	2
5124077.1	M 082	0.0008	I	18/04/2007	148.7614 , 69.8429	2		
3390002.2	M 082	0.0008	I	19/04/2009	148.9060 , 69.7015	2	148.9796 , 69.6842	6
3390003.1	M 082	0.0008	I	22/10/2008	149.0280 , 69.6587	2	148.9547 , 69.6760	6
3390001.1	M 082[f]	0.0008	I	21/10/2008	149.0390 , 69.6614	2	148.9658 , 69.6788	9
3390002.1	M 082	0.0008	I	23/10/2008	149.0536 , 69.6643	2	148.9796 , 69.6813	6
1420415.1	M 083	0.0017	S	26/07/2009	204.2580 , -29.8644	4	204.2907 , -29.8762	2
5201399.1	M 086	-0.0009	E	22/12/2009	186.5493 , 12.9440	3	186.5205 , 12.9568	2
1420101.1	M 087	0.0042	E	23/06/2009	187.7063 , 12.3915	4		
1420100.1	M 087	0.0042	E	22/06/2009	187.7073 , 12.3923	4		
1422169.1	M 089	0.0009	E	24/12/2009	188.9167 , 12.5536	3		
1420458.1	M 090	-0.0008	S	24/06/2008	189.2091 , 13.1643	3		
1422174.1	M 090	-0.0008	S	24/12/2009	189.2120 , 13.1721	2		
1420445.1	M 094	0.0010	S	12/12/2008	192.7069 , 41.1220	3		
1422152.1	M 094	0.0010	S	12/12/2009	192.7223 , 41.1186	3		
1420446.1	M 094	0.0010	S	12/06/2008	192.7365 , 41.1194	3		
1420446.2	M 094	0.0010	S	12/12/2008	192.7380 , 41.1154	5	192.7034 , 41.1319	2
1420389.1	M 101	0.0009	S	13/06/2008	210.8048 , 54.3508	2	210.8423 , 54.3291	2
1422171.1	M 104	0.0040	S	04/01/2010	189.9978 , -11.6246	5	189.9690 , -11.6122	2
1422159.1	M 106	0.0015	S	01/12/2009	184.7393 , 47.3035	3	184.7020 , 47.3212	2
1420372.1	M 106	0.0015	S	01/06/2008	184.7419 , 47.3061	4	184.7796 , 47.2890	2
1420054.1	M 110	-0.0008	E	19/07/2009	10.0928 , 41.6838	2	10.0561 , 41.6696	2
1420053.1	M 110	-0.0008	E	19/07/2009	10.0938 , 41.7002	2	10.0572 , 41.6860	2
1420056.1	M 110	-0.0008	E	20/07/2009	10.0946 , 41.6676	2	10.0580 , 41.6533	2
1422147.1	Mink galaxy	0.0187	?	09/01/2010	21.4312 , -1.3794	2		
1422147.3	Mink galaxy	0.0187	?	10/01/2010	21.4314 , -1.3778	2		
1420396.1	Mink galaxy	0.0187	?	10/07/2008	21.4355 , -1.3811	2		
1420318.1	Mrk 0033	0.0048	I	07/11/2008	158.1345 , 54.3988	2		
1421318.1	Mrk 0034	0.0048	I	05/05/2009	158.1333 , 54.4033	2		
1420319.1	Mrk 0059	0.0026	?	17/06/2008	194.7531 , 34.8478	2		
1420330.1	Mrk 0162	0.0213	I	17/05/2009	166.2850 , 44.7485	2		
1420421.1	Mrk 0206	0.0037	?	08/05/2009	186.0694 , 67.4417	2		
1420419.1	Mrk 0331	0.0187	S	29/06/2008	357.8625 , 20.5848	2		
1421419.1	Mrk 0332	0.0187	S	28/12/2008	357.8588 , 20.5866	2		
1420351.1	NGC 0053	0.0153	S	18/11/2008	3.6716 , -60.3282	2		
1420334.1	NGC 0055	0.0004	S	04/06/2008	3.7251 , -39.1978	2	3.6905 , -39.2131	2
1422187.1	NGC 0253[g]	0.0008	S	21/12/2009	11.8847 , -25.2881	5	11.9153 , -25.2746	3
1422197.1	NGC 0253	0.0008	S	21/12/2009	11.8858 , -25.2854	2	11.9165 , -25.2720	2
1422190.1	NGC 0253	0.0008	S	22/12/2009	11.8858 , -25.2590	5	11.9166 , -25.2458	3
1422196.1	NGC 0253[h]	0.0008	S	21/12/2009	11.8859 , -25.2898	4	11.9166 , -25.2763	2
3390006.1	NGC 0253	0.0008	S	20/06/2009	11.9173 , -25.2775	3	11.8865 , -25.2910	4
1422229.1	NGC 0315	0.0164	E	15/01/2010	14.4500 , 30.3517	3		
5200826.1	NGC 0315	0.0164	E	18/07/2009	14.4554 , 30.3517	3		
5200827.1	NGC 0404	-0.0001	L	22/07/2009	17.3644 , 35.7164	3	17.3297 , 35.7037	2
5200470.1	NGC 0514	0.0083	S	13/01/2009	21.0128 , 12.9161	2		
1420482.1	NGC 0584	0.0061	E	10/07/2008	22.8370 , -6.8695	3		
1420097.1	NGC 0612	0.0299	L	25/12/2008	23.4853 , -36.4926	2		
1420096.1	NGC 0612	0.0299	L	26/06/2008	23.4918 , -36.4962	2		
5200014.1	NGC 0633	0.0172	S	26/06/2008			24.0950 , -37.3253	2
5200830.1	NGC 0772	0.0083	S	26/07/2009	29.8339 , 19.0072	3		
5200472.1	NGC 0777	0.0167	E	28/01/2009	30.0592 , 31.4320	2		
1420388.1	NGC 0835	0.0130	S	17/07/2008	32.3535 , -10.1386	2		
1420132.1	NGC 0891	0.0018	S	10/08/2008			35.6175 , 42.3155	2

Table 2.1 Continued

Obs. ID[a]	Target name	Redshift[b]	Type[b,c]	Obs. date	RA, DEC[d], N_{sub}[e] (Ns)			RA, DEC[d], N_{sub}[e] (Nh)		
1420134.1	NGC 0891	0.0018	S	10/08/2009				35.6300 ,	42.3351	2
1420136.1	NGC 0891	0.0018	S	10/08/2009				35.6421 ,	42.3559	3
1420138.1	NGC 0891	0.0018	S	10/08/2009				35.6540 ,	42.3770	2
5200065.1	NGC 0959	0.0020	S	08/08/2008	38.1023 ,	35.4936	2			
5200066.1	NGC 1023	0.0021	L	11/08/2008	40.1026 ,	39.0616	6	40.0651 ,	39.0518	2
1402108.1	NGC 1052	0.0049	E	27/07/2007	40.2711 ,	-8.2547	6			
5200067.1	NGC 1058	0.0017	S	12/08/2008	40.8771 ,	37.3399	2			
1420462.1	NGC 1097[i]	0.0042	S	18/07/2008	41.5803 ,	-30.2751	9			
1422155.1	NGC 1140	0.0050	I	27/01/2010	43.6353 ,	-10.0266	2			
1420457.1	NGC 1269	0.0026	S	19/07/2008	49.3283 ,	-41.1105	6			
1420354.1	NGC 1313	0.0016	S	01/06/2008	49.5231 ,	-66.5101	2			
1420353.1	NGC 1313	0.0016	S	03/12/2008	49.5614 ,	-66.5003	2	49.5870 ,	-66.4712	2
1420355.1	NGC 1313	0.0016	S	02/06/2008	49.6043 ,	-66.4796	2	49.5777 ,	-66.5085	2
1422246.1	NGC 1316	0.0059	L	22/01/2010	50.6642 ,	-37.2005	6	50.6994 ,	-37.1874	2
1400125.1	NGC 1316	0.0059	L	23/01/2007	50.6687 ,	-37.2108	6	50.7038 ,	-37.1980	2
1422245.1	NGC 1316	0.0059	L	22/01/2010	50.6748 ,	-37.2141	3	50.7099 ,	-37.2011	2
1420439.1	NGC 1316	0.0059	L	24/07/2008	50.6762 ,	-37.2093	2	50.6413 ,	-37.2226	2
1400997.1	NGC 1546	0.0041	L	18/01/2007	63.6471 ,	-56.0641	4			
1400019.1	NGC 1549	0.0041	E	18/01/2007	63.9332 ,	-55.5949	6	63.9758 ,	-55.5757	2
1420467.1	NGC 1566	0.0050	S	21/07/2008	65.0035 ,	-54.9396	3			
1420331.1	NGC 1569	-0.0003	I	08/09/2008	67.7101 ,	64.8474	3			
1420398.1	NGC 1614	0.0159	S	27/08/2008	68.4961 ,	-8.5802	3			
5200049.1	NGC 1614	0.0159	S	27/08/2008				68.5021 ,	-8.5816	2
5200049.2	NGC 1614	0.0159	S	27/08/2008				68.5114 ,	-8.5815	2
1420323.1	NGC 1741	0.0134	I	05/09/2008	75.4088 ,	-4.2581	2			
1420323.2	NGC 1741	0.0134	I	06/09/2008	75.4095 ,	-4.2596	2			
1420357.1	NGC 1808	0.0033	S	01/09/2008	76.9296 ,	-37.5142	6			
5200185.1	NGC 1961	0.0131	S	19/09/2008	85.5281 ,	69.3776	3			
1420400.1	NGC 2146	0.0030	S	22/09/2008	94.6696 ,	78.3539	6			
1420436.1	NGC 2403	0.0004	S	05/10/2008	114.2089 ,	65.5932	2	114.1363 ,	65.6007	2
1420358.1	NGC 2403	0.0004	S	05/10/2008	114.2186 ,	65.6001	2	114.1462 ,	65.6078	2
1420360.1	NGC 2403	0.0004	S	05/10/2008	114.2324 ,	65.5940	2	114.1600 ,	65.6016	2
1420359.1	NGC 2403	0.0004	S	05/10/2008	114.2838 ,	65.6088	3	114.2113 ,	65.6164	2
5200304.1	NGC 2500	0.0017	S	14/10/2008	120.4781 ,	50.7361	2			
1401002.1	NGC 2768	0.0046	E	19/04/2007	137.8994 ,	60.0374	4	137.9557 ,	60.0250	2
1422243.1	NGC 2768	0.0046	E	22/10/2009	137.9078 ,	60.0332	2	137.8514 ,	60.0458	2
1420364.1	NGC 2782	0.0085	S	28/04/2009	138.5206 ,	40.1158	2			
1420124.1	NGC 2841	0.0021	S	26/04/2009	140.4979 ,	50.9904	3	140.5434 ,	50.9791	2
1420122.1	NGC 2841	0.0021	S	29/10/2008	140.5135 ,	50.9729	2			
1420123.1	NGC 2841	0.0021	S	26/04/2009	140.5229 ,	50.9649	2			
1420128.1	NGC 2976	0.0000	S	21/10/2008	146.7947 ,	67.9128	2			
1420126.1	NGC 2976	0.0000	S	23/10/2008	146.8204 ,	67.9132	2	146.7501 ,	67.9291	2
1420127.1	NGC 2976	0.0000	S	23/10/2008	146.8376 ,	67.9132	2	146.7674 ,	67.9291	2
5200783.1	NGC 3073	0.0039	L	29/04/2009	150.2172 ,	55.6218	2			
1420405.1	NGC 3077	0.0000	I	20/04/2009	150.8253 ,	68.7357	3			
1422185.1	NGC 3079	0.0038	S	01/11/2009	150.4875 ,	55.6851	3			
1422184.1	NGC 3079	0.0038	S	01/11/2009	150.4943 ,	55.6763	3			
1422186.1	NGC 3079	0.0038	S	03/11/2009	150.4984 ,	55.6627	2			
1420407.1	NGC 3125	0.0036	E	06/06/2009	151.6427 ,	-29.9351	2			
5200785.1	NGC 3147	0.0094	S	16/04/2009	154.2229 ,	73.4044	3			
5200306.1	NGC 3147	0.0094	S	20/10/2008	154.2373 ,	73.3976	3			
1422162.1	NGC 3189	0.0043	S	21/11/2009	154.5245 ,	21.8285	2			
5200009.2	NGC 3256	0.0084	S	23/06/2008	156.9342 ,	-43.8892	6	156.9696 ,	-43.9065	2
5200009.1	NGC 3256	0.0084	S	21/06/2008	156.9348 ,	-43.8880	2	156.9706 ,	-43.9048	2
1420420.1	NGC 3256	0.0084	S	21/06/2008	156.9658 ,	-43.9049	2	157.0016 ,	-43.9216	3
5201209.1	NGC 3344	0.0020	S	24/11/2009	160.8805 ,	24.9185	2	160.8492 ,	24.9308	2
5200370.1	NGC 3344	0.0020	S	24/11/2008	160.8852 ,	24.9176	2	160.8541 ,	24.9300	2
5200372.1	NGC 3377	0.0023	E	29/11/2008	161.9245 ,	13.9810	2			
5201213.1	NGC 3412	0.0029	L	01/12/2009	162.7233 ,	13.4095	3			

Table 2.1 Continued

Obs. ID[a]	Target name	Redshift[b]	Type[b,c]	Obs. date	RA, DEC[d], N_{sub}[e] (Ns)		RA, DEC[d], N_{sub}[e] (Nh)	
5200375.1	NGC 3486	0.0023	S	25/11/2008	165.1001 , 28.9723	2		
1420070.1	NGC 3557	0.0101	E	28/12/2008	167.4899 , -37.5425	3		
1420069.1	NGC 3557	0.0101	E	27/06/2008	167.4943 , -37.5395	3		
1420438.1	NGC 3621	0.0024	S	26/12/2008	169.5688 , -32.8174	3	169.5364 , -32.8028	2
1421438.1	NGC 3621	0.0024	S	27/06/2009	169.5741 , -32.8150	2	169.6062 , -32.8297	2
1420410.1	NGC 3628	0.0029	S	05/06/2009	170.0454 , 13.6002	2	170.0744 , 13.5878	2
1420145.1	NGC 3628	0.0029	S	06/06/2009	170.0560 , 13.5977	2	170.0850 , 13.5853	3
1420147.1	NGC 3735	0.0090	S	31/10/2008	173.9662 , 70.5378	2		
1420146.1	NGC 3735	0.0090	S	31/10/2008	173.9870 , 70.5319	2		
1420148.1	NGC 3735	0.0090	S	31/10/2008	174.0109 , 70.5271	2		
1420072.1	NGC 3894	0.0108	E	13/05/2009	177.2116 , 59.4182	2		
1420073.1	NGC 3894	0.0108	E	14/05/2009	177.2120 , 59.4175	2		
1420074.1	NGC 3904	0.0053	E	02/07/2008	177.3087 , -29.2759	3		
1420075.1	NGC 3904	0.0053	E	02/07/2009	177.3088 , -29.2764	3		
1422160.1	NGC 3921	0.0197	S	21/11/2009	177.7778 , 55.0764	2		
1400040.1	NGC 3962	0.0061	E	26/12/2006	178.6709 , -13.9766	4		
5201215.1	NGC 3998	0.0036	L	20/11/2009	179.4816 , 55.4501	3		
5200376.1	NGC 3998	0.0036	L	20/11/2008	179.4842 , 55.4503	2		
1420369.1	NGC 4041	0.0041	S	12/05/2009	180.5508 , 62.1393	3		
1400043.1	NGC 4125	0.0045	E	13/11/2006	182.0302 , 65.1722	6		
5201388.1	NGC 4138	0.0030	L	04/12/2009	182.3744 , 43.6826	3		
5200837.1	NGC 4138	0.0030	L	02/06/2009	182.3750 , 43.6870	2		
5200377.2	NGC 4157	0.0026	S	27/11/2008	182.7684 , 50.4804	3		
5200377.1	NGC 4157	0.0026	S	27/11/2008	182.7685 , 50.4823	2		
1422150.1	NGC 4194	0.0082	I	24/11/2009	183.5393 , 54.5236	2		
5200840.1	NGC 4203	0.0037	L	09/06/2009	183.7737 , 33.1998	3		
5200844.1	NGC 4261	0.0073	E	22/06/2009	184.8470 , 5.8252	4		
1420110.1	NGC 4278	0.0023	E	13/06/2009	185.0303 , 29.2820	3		
5200010.1	NGC 4355	0.0070	S	28/06/2008			186.7322 , -0.8783	2
1420430.1	NGC 4449	0.0007	I	05/06/2008	187.0466 , 44.0949	3		
5200854.1	NGC 4496B	0.0150	I	26/06/2009	187.9225 , 3.9269	2		
5200858.1	NGC 4618	0.0017	S	09/06/2009	190.3882 , 41.1524	2		
5201409.1	NGC 4618	0.0017	S	11/12/2009	190.3892 , 41.1479	2		
1422238.1	NGC 4636	0.0032	E	30/12/2009	190.7076 , 2.6862	3	190.6793 , 2.6987	2
1420078.1	NGC 4636	0.0032	E	29/06/2008	190.7098 , 2.6896	3	190.7380 , 2.6772	2
1420079.1	NGC 4636	0.0032	E	29/06/2008	190.7099 , 2.6894	3	190.7381 , 2.6770	2
1421307.1	NGC 4670	0.0036	S	20/12/2008	191.3221 , 27.1225	2		
1420307.1	NGC 4670	0.0036	S	18/06/2008	191.3222 , 27.1270	3		
5200862.1	NGC 4689	0.0054	S	27/06/2009	191.9417 , 13.7646	2		
1420081.1	NGC 4696	0.0098	E	20/07/2008	192.2097 , -41.3107	3		
1420080.1	NGC 4696	0.0098	E	20/07/2008	192.2114 , -41.3128	3		
1420098.1	NGC 4697	0.0040	E	06/07/2008	192.1509 , -5.8005	6		
1422240.1	NGC 5018	0.0094	E	15/01/2010	198.2545 , -19.5218	3		
1420083.1	NGC 5018	0.0094	E	16/07/2008	198.2561 , -19.5168	3		
1420082.1	NGC 5018	0.0094	E	15/07/2008	198.2563 , -19.5168	2		
1420086.1	NGC 5044	0.0090	E	15/07/2008	198.8519 , -16.3856	3		
1420087.1	NGC 5044	0.0090	E	15/07/2008	198.8519 , -16.3855	3		
5200864.1	NGC 5147	0.0037	S	10/07/2009	201.5834 , 2.1026	2		
5200514.1	NGC 5248	0.0038	S	08/01/2009	204.3838 , 8.8821	3	204.3552 , 8.8942	2
5200514.2	NGC 5248	0.0038	S	08/01/2009	204.3851 , 8.8837	3	204.3563 , 8.8959	2
1422153.1	NGC 5253	0.0013	I	24/01/2010	204.9855 , -31.6425	3		
5200866.1	NGC 5273	0.0034	L	28/06/2009	205.5359 , 35.6590	2		
1420119.1	NGC 5322	0.0061	E	04/06/2008	207.3155 , 60.1917	3		
1420118.1	NGC 5322	0.0061	E	03/06/2008	207.3157 , 60.1915	3		
5201418.1	NGC 5353	0.0076	L	27/12/2009	208.3610 , 40.2803	3		
5200517.1	NGC 5363	0.0038	I	14/01/2009	209.0303 , 5.2515	3		
5200868.1	NGC 5363	0.0038	I	18/07/2009	209.0312 , 5.2565	3		
5200869.1	NGC 5371	0.0086	S	29/06/2009	208.9162 , 40.4626	3		
1380065.1	NGC 5403	0.0096	S	01/07/2008	209.9633 , 38.1837	3		

Table 2.1 Continued

Obs. ID[a]	Target name	Redshift[b]	Type[b,c]	Obs. date	RA, DEC[d], $N_{\rm sub}$[e] (Ns)			RA, DEC[d], $N_{\rm sub}$[e] (Nh)		
1420373.1	NGC 5430	0.0100	S	04/06/2008	210.1931 ,	59.3307	2			
1420374.1	NGC 5430	0.0100	S	05/06/2008	210.1980 ,	59.3251	2			
1420390.1	NGC 5471	0.0012	?	15/06/2008	211.1243 ,	54.3990	2			
5200871.1	NGC 5668	0.0053	S	26/07/2009	218.3527 ,	4.4524	2			
5201422.1	NGC 5668	0.0053	S	25/01/2010	218.3533 ,	4.4490	2			
5200872.1	NGC 5669	0.0046	S	24/07/2009	218.1857 ,	9.8942	2			
5200873.1	NGC 5746	0.0058	S	31/07/2009	221.2341 ,	1.9562	3			
5200069.1	NGC 5813	0.0064	E	03/08/2008	225.2966 ,	1.7040	3			
1420416.1	NGC 5953	0.0067	S	08/08/2008	233.6330 ,	15.1969	2			
1420416.2	NGC 5953	0.0067	S	05/02/2009	233.6366 ,	15.1918	3			
1402684.1	NGC 6052	0.0150	S	17/08/2007	241.3014 ,	20.5425	3			
5200307.1	NGC 6340	0.0041	S	23/10/2008	257.5935 ,	72.3044	2			
5200686.1	NGC 6482	0.0131	E	16/03/2009	267.9577 ,	23.0696	3			
5200686.2	NGC 6482	0.0131	E	17/03/2009	267.9588 ,	23.0716	3			
1420377.1	NGC 6500	0.0100	S	19/03/2009	269.0037 ,	18.3352	2			
5200047.2	NGC 6621	0.0198	S	30/07/2008				273.2350 ,	68.3644	2
5200687.1	NGC 6689	0.0016	S	04/02/2009	278.7107 ,	70.5213	2			
5200256.1	NGC 6703	0.0079	L	13/10/2008	281.8228 ,	45.5513	3			
5200308.1	NGC 6703	0.0079	L	14/10/2008	281.8228 ,	45.5515	3			
1420378.1	NGC 6764	0.0080	S	24/04/2009	287.0694 ,	50.9331	2			
1420443.1	NGC 6946	0.0002	S	18/06/2009	308.7192 ,	60.1607	2	308.6806 ,	60.1366	2
1420440.1	NGC 6946	0.0002	S	17/06/2009	308.7580 ,	60.1756	2	308.7189 ,	60.1516	2
1400371.1	NGC 6951	0.0048	S	06/01/2007	309.3269 ,	66.1013	2			
1422242.1	NGC 7052	0.0158	E	24/11/2009	319.6338 ,	26.4484	2			
1420092.1	NGC 7052	0.0158	E	23/05/2009	319.6387 ,	26.4455	2			
1420093.1	NGC 7052	0.0158	E	23/05/2009	319.6399 ,	26.4454	2			
5200795.1	NGC 7080	0.0161	S	25/05/2009	322.5097 ,	26.7170	2			
3221001.1	NGC 7320	0.0195	S	18/06/2007	339.0155 ,	33.9501	2			
1420383.1	NGC 7582	0.0053	S	23/05/2009	349.5904 ,	-42.3561	2			
1420418.1	NGC 7714	0.0094	S	16/06/2008	354.0587 ,	2.1544	3			
1421418.1	NGC 7714	0.0094	S	16/12/2008				354.0575 ,	2.1563	2
1420386.1	NGC 7727	0.0061	S	11/12/2008	354.9710 ,	-12.2931	3			
5200874.1	NGC 7741	0.0025	S	29/06/2009	355.9744 ,	26.0741	2			
5200875.1	NGC 7742	0.0055	S	22/06/2009	356.0654 ,	10.7648	2			
5200527.1	NGC 7798	0.0082	S	29/12/2008	359.8529 ,	20.7493	2			
5200876.1	NGC 7798	0.0082	S	30/06/2009	359.8575 ,	20.7480	2			
5200876.2	NGC 7798	0.0082	S	30/06/2009	359.8589 ,	20.7503	2			
5200528.1	UGC 0128	0.0151	S	08/01/2009	3.4431 ,	35.9784	2			
1420361.1	UGC 4305	0.0005	I	08/10/2008	124.8082 ,	70.7162	2	124.7213 ,	70.7275	2
1420362.1	UGC 4305	0.0005	I	09/10/2008	124.8225 ,	70.7132	2	124.7355 ,	70.7243	2
1422149.1	UGC 4393	0.0071	S	21/10/2009	126.5217 ,	45.9647	2			
1420424.1	UGC 4703	0.0118	E	05/05/2009	134.6109 ,	6.3279	2			

[a] Observation IDs in seven digits and sub-IDs in one digit. Multiple observations in Phase 3 have sub-IDs of 2, 3, or 4.
[b] Taken from Third Reference Catalog of Bright Galaxies (de Vaucouleurs et al. 1991) or SIMBAD astronomical database.
[c] Morphological types of galaxies. E, L, S, I, and ? indicate elliptical, lens, spiral, irregular, and unidentified galaxies, respectively.
[d] Equatorial coordinates (J2000) of the center of the slit. The slit is located along with the ecliptic latitude.
[e] Number of sub-apertures in a slit.
[f] Combined with 3390001.2.
[g] Combined with 1422187.3.
[h] Combined with 1422196.3.
[i] 1420462.2 was also used for the detailed study in Section 3.2.3. 1420462.1 and 1420462.2 correspond to Slits A and B, respectively.

2.3 Data reduction and analyses

A flowchart of the data reduction and analyses is shown in Fig. 2.5. All the data analyzed in this thesis were taken from the AKARI archives[*1]. The basic spectral analysis was performed by using the standard IDL pipeline with a newly calibrated spectral response curve[*2]. The versions of the pipelines for Phases 2 and 3 data are 20110114 and 20110301, respectively. After the basic pipeline process, hot pixels were removed from the array image before creating a spectrum, where pixel intensities were replaced by the median values of contiguous 8 pixels. By using the hot-pixel-free array image, a spectrum was extracted from the maximum slit width (25 pixels for Ns, 30 pixels for Nh). Based on the spectrum and the reference image, the data affected by ghost images and detector anomaly were rejected. Next, wavelength-dependent background noise was considered for the spectra taken in Phase 3 in addition to the errors given by the pipeline; the background noise was evaluated as 1σ standard deviations every 0.2 μm wavelength range, using 298 NIR spectra for the blank sky which were taken in a framework of the AKARI mission program, MSAGN (PI: S. Oyabu). As a background emission, a spectrum of the

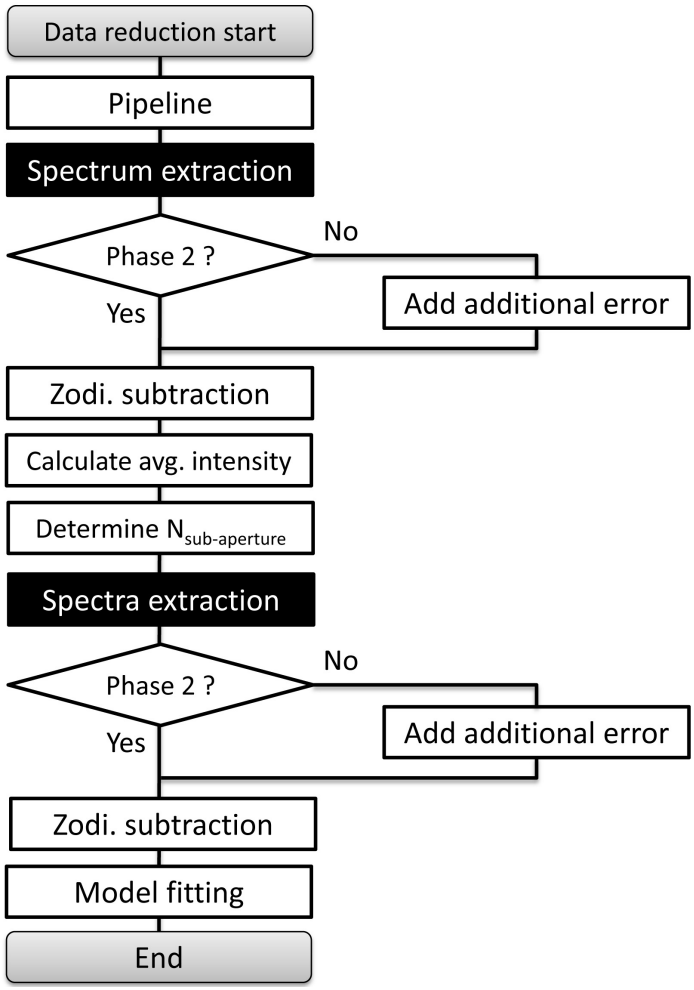

Figure 2.5 Flowchart of the data reduction and analysis.

[*1] http://darts.jaxa.jp/ir/akari/
[*2] http://www.ir.isas.jaxa.jp/ASTRO-F/Observation/

Table 2.2 Numbers and sizes of sub-apertures in a slit depending on the mean intensity and the fraction of hot pixels.

Mean intensity (MJy/str)	Phase 2	Phase 3 (< 3.7 %)	Phase 3 (> 3.7 %)
	Ns slit		
< 1.0	2 ($5'' \times 17.''5$)	2 ($5'' \times 17.''5$)	2 ($5'' \times 17.''5$)
1.0 – 3.2	3 ($5'' \times 11.''7$)	2 ($5'' \times 17.''5$)	2 ($5'' \times 17.''5$)
3.2 – 10	4 ($5'' \times 8.''8$)	3 ($5'' \times 11.''7$)	3 ($5'' \times 11.''7$)
10 – 32	6 ($5'' \times 5.''8$)	6 ($5'' \times 5.''8$)	4 ($5'' \times 8.''8$)
> 32	8 ($5'' \times 4.''4$)	8 ($5'' \times 4.''4$)	5 ($5'' \times 7.''3$)
	Nh slit		
< 1.0	2 ($3'' \times 21.''9$)	2 ($3'' \times 21.''9$)	2 ($3'' \times 21.''9$)
1.0 – 3.2	3 ($3'' \times 14.''6$)	2 ($3'' \times 21.''9$)	2 ($3'' \times 21.''9$)
3.2 – 10	4 ($3'' \times 10.''2$)	3 ($3'' \times 14.''6$)	3 ($3'' \times 14.''6$)
10 – 32	6 ($3'' \times 7.''3$)	6 ($3'' \times 7.''3$)	4 ($3'' \times 10.''2$)
> 32	10 ($3'' \times 4.''4$)	10 ($3'' \times 4.''4$)	6 ($3'' \times 7.''3$)

zodiacal light in each region was subtracted based on the spectral template in Tsumura et al. (2013). The template describes the zodiacal light emission as sum of two blackbody emissions with temperatures of 5800 K and 300 K. The intensity of the zodiacal emission is typically in a range of 0.1–1.0 MJy/str. For each background-subtracted spectrum, the mean intensity between 2.5–5.0 μm was calculated to determine the number of sub-apertures, which was used to extract multiple spectra from a slit. The criteria to determine the number are listed in Table. 2.2. In the table, a fraction of hot pixels of each observation was also used as a criterion, which determines the number of available pixels in an array image. The resultant numbers of the sub-apertures are listed in Table 2.1.

After determination of the sub-apertures, the corresponding number of spectra were extracted from the slit. Addition of the wavelength-dependent errors and subtraction of zodiacal light were performed for each spectrum as described above. Finally, smoothing was applied for each spectrum with a boxcar kernel of 3 pixels ($\sim$ 0.03 μm) in the direction of wavelength. As a result, 1031 spectra were extracted from the 369 observed regions. These spectra were evaluated by using the fitting model described in the next section. In order to establish a reliable sample of the NIR spectra with ices, presence or absence of the ices was evaluated only for the spectra which show S/N $\geq$ 10 for the continuum emission at a wavelength of 3.05 μm for H_2O ice and/or S/N $\geq$ 20 for the continuum emission at a wavelength of 4.27 μm for CO_2 ice. For the Phase 3 data, these thresholds correspond to $\geq$ 3 MJy/str and $\geq$ 10 MJy/str for H_2O and CO_2 ices, respectively. The thresholds ensure the detection of H_2O and CO_2 ices with an optical depth as small as $\tau = 0.05$, which is four times smaller than that in the past search for H_2O ice at 6 μm (Spoon et al. 2002). The detection of the ices was judged based on whether a spectrum shows the features with significance of $\geq 3\sigma$ or not.

For particular galaxies, spectral maps were created to examine the spatial distributions of the ices and other emission features. In order to make the maps, not only the spectra derived in the above procedure but also those from other slit sub-apertures of the same size at intermediate positions were evaluated. In order to extract spectra at intermediate positions, the slit sub-aperture position was shifted by 1 pixel one after the other to consecutively derive spectra along the slit.

2.4 Fitting model

In order to search for absorption features due to ices, a fitting model was used, which was created by the following procedures. The 2.5–5.0 μm range contains spectral features due to H_2O, NH_3, CO_2, CH_3OH, CO, ^{13}CO, and XCN ices are present. Among them, the absorption features due to NH_3, CH_3OH, and ^{13}CO are expected to be very weak; optical depths of these ices relative to that of H_2O ice are typically <0.1 (Gibb et al. 2004). Therefore, these features were not evaluated due to the limit of the sensitivity. Additionally, the wavelength range of 4.6–4.7 μm, which contains the absorption features due to XCN and CO ices, suffers contamination of the strong spectral lines due to CO gas, Pfβ, and H_2 S(9) as shown in Fig. 1.12. AKARI cannot spectroscopically resolve these features due to rather low spectral resolution ($R \sim 100$). Hence only H_2O and CO_2 ices were evaluated in the present thesis, considering the sensitivity and spectral resolution of AKARI/IRC.

In the fitting calculations for H_2O ice, a wide wavelength range is needed to determine the continuum because the absorption feature is broad between 2.7–3.3 μm. At the short and long wavelength ends, Brβ, the PAH 3.3 μm, aliphatic 3.4–3.6 μm features are present. Therefore, these features were included in the fitting model to determine the continuum accurately. Particularly, Brβ is important because the wavelength range available for the determination of continuum levels is very limited on the short wavelength side. Hence assuming that the hydrogen recombination lines in the NIR (Brα, Brβ, and Pfγ) come from the same region, the common width of the lines was determined. Eventually, a wavelength range of 2.5–4.1 μm was used for the calculation to estimate the intensity of the absorption feature of H_2O ice.

Details of the parameters used in the fitting calculations are summarized in Table 2.3. Continuum components in the NIR are typically described by blackbody emissions which are attributed to hot dust with temperatures of 100–1000 K and/or photospheres of cool stars with temperature of $\gtrsim$ 3000 K. Therefore, multi-temperature blackbody emissions were used to fit the continuum emission of H_2O ice. However, in the case that both amplitudes and temperatures were set to be free, the parameters did not converge properly. Hence, the temperatures were fixed and only amplitudes were fitted, since the derived temperatures are not important in this study. The temperatures of 200, 400, 800, 1600, and 3200 K were used, where the peak wavelengths were equally spaced. The former four temperatures typically represent emission from interstellar hot dust. The temperature of 1600 K roughly corresponds to the upper limit for dust sublimation. The last one typically corresponds to the photospheric emission of low-mass stars.

As to the absorption profiles of H_2O ice, two kinds of the absorption profiles obtained by laboratory measurement were tested to fit the spectra, and resultant χ^2/d.o.f values were evaluated; the absorption profile vary depending on the condition of icy mantles (Section 1.2.3). The tested ices are those with pure H_2O ice at 10 K and 80 K (Ehrenfreund et al. 1996). As for emission lines and features, Lorentzian functions were used to fit the PAH 3.3 μm and aliphatic hydrocarbon at 3.4 μm, and Gaussian functions were used to fit the hydrogen recombination lines and aliphatic hydrocarbon at 3.5 μm. The former and latter functions were used for resolved and unresolved spectral features, respectively. The fitting function is described as follows:

$$I = \left(\sum_i a_i {I_i}^{\mathrm{cont}} \right) \times \exp\left(-bI^{\mathrm{abs}}\right) + \sum_j c_j {I_j}^{\mathrm{em}}, \tag{2.1}$$

where ${I_i}^{\rm cont}$, $I^{\rm abs}$, and ${I_j}^{\rm em}$ represent spectral components of continuum, absorption, and emissions features, respectively, while a_i, b, and c_j are free parameters. In the spectral fitting, such geometry was assumed that sources of the continuum emission are located in the background of ices, while those of emission lines and features are in the foreground. Actually, even if the emission lines and features are located in the background, no significant difference is made in fitting results because the emission lines and features in the NIR are not significantly overlapped with H_2O ice feature. Although the profile of the PAH 3.3 μm slightly overlaps with that of H_2O ice, the contribution of the absorption to the continuum at 3.3 μm is less than 2 % relative to the continuum intensity, which is smaller than the typical noise level. As a result for the spectra with detection of H_2O ice, the fitting results obtained by using the profile of H_2O ice at 10 K show smaller χ^2/d.o.f values than those of H_2O ice at 80 K. With a 90 % confidence level, the χ^2/d.o.f values are unacceptable, which is possibly caused by the simple continuum functions. Based on one-sample t-tests, it is found that the difference in the χ^2/d.o.f value is significant. Hence, the fitting results obtained by using the profile of pure H_2O ice at 10 K were adopted.

As to the absorption profiles of CO_2 ice, local continuum levels are easily determined because the absorption feature is narrow as compared to that of H_2O ice. In order to avoid the contributions from Brα and the CO gas absorption feature, the wavelength range of 4.1–4.4 μm was used for the fitting calculation of CO_2 ice. In the case of CO_2 ice, therefore, a simple linear continuum was used instead of multiple blackbody; blackbody emission in such narrow wavelength range can be approximated by a linear function. Three kinds of the absorption profiles obtained by the laboratory measurement were tested to fit the spectra, and resultant χ^2/d.o.f values were evaluated. The tested ices are those with H_2O:CO_2=100:14 at 10 K, H_2O:CH_3OH:CO_2=9:1:2 at 10 K, and H_2O:CO_2:CO=100:20:3 at 20 K for CO_2 ice (Ehrenfreund et al. 1996). The fitting function is described as follows:

$$I = (a\lambda + b) \times \exp\left(-cI^{\rm abs}\right), \tag{2.2}$$

where a, b, and c are free parameters. As a result, the fitting results obtained by using the profile of H_2O:CH_3OH:CO_2 show smaller χ^2/d.o.f values than those of the other profiles, which were acceptable with a 90 % confidence level. Based on one-sample t-tests, it is found that difference in the χ^2/d.o.f value is significant. Hence, the fitting results obtained by using the profile of H_2O:CH_3OH:CO_2 ice at 10 K were adopted.

Based on the fitting results, the column density, N, of each ice is derived from the equation

$$N = \int \tau d\nu / A, \tag{2.3}$$

where A, τ, and ν are the band strength of each ice feature measured in a laboratory, an optical depth derived from the fitting, and a wavenumber (cm^{-1}), respectively. The band strengths of 2.0×10^{-16} cm/molecule and 7.6×10^{-17} cm/molecule were used for H_2O and CO_2 ices, respectively (Gerakines et al. 1995).

Table 2.3 Summary of the fitting parameters.

Feature	Profile	Free parameter	Fixed parameter
H_2O ice			
Absorption	pure H_2O 10 K[a]	amplitude	—
Continuum	black body	amplitude	temperature (200 K)
Continuum	black body	amplitude	temperature (400 K)
Continuum	black body	amplitude	temperature (800 K)
Continuum	black body	amplitude	temperature (1600 K)
Continuum	black body	amplitude	temperature (3200 K)
Brα	Gauss function	amplitude, width[b]	$\lambda_{\rm center}$ (4.05 μm)
Brβ	Gauss function	amplitude, width[b]	$\lambda_{\rm center}$ (2.63 μm)
Pfγ	Gauss function	amplitude, width[b]	$\lambda_{\rm center}$ (3.74 μm)
PAH 3.3 μm	Lorentz function	amplitude, width	$\lambda_{\rm center}$ (3.29 μm)
Aliphatic 3.4 μm	Lorentz function	amplitude, width	$\lambda_{\rm center}$ (3.40 μm)
Aliphatic 3.5 μm	Gauss function	amplitude, width, $\lambda_{\rm center}$	—
CO_2 ice			
Absorption	H_2O:CH_3OH:CO_2 10 K[a]	amplitude	—
Continuum	linear function	slope, intercept	—

[a] Laboratory measurement from Ehrenfreund et al. (1996).
[b] Common with.

Chapter 3

Results

3.1 Statistical results for all the galaxy sample

Overall results

As a result of the search for the ices in nearby galaxies, H_2O ice is significantly detected from 125 regions in 30 galaxies, while CO_2 ice is detected from 54 regions in 12 galaxies. Table 3.1 summarizes the parameters derived by the spectral fitting (Section 2.4), which include the column densities of the ices, the continuum intensities at 3.05 and 4.27 μm, and the intensities of the PAH 3.3 μm, Brα, and Brβ. Examples of the spectra in which the ices are detected are shown in Fig. 3.1, while all the spectra are shown in Appendix A. This search for the first time provides us with the systematic sample of galaxies with detection of CO_2 ice and the most sensitive sample of galaxies with detection of H_2O ice; H_2O ice is detected from regions with the column density as low as 5×10^{16} cm^{-2} which is about 2 orders of magnitude lower than that in the past search for H_2O ice at a wavelength of 6 μm (Spoon et al. 2002). It is notable that the ices are detected in multiple regions within galaxies, demonstrating that ices are also present in off-center regions of galaxies where past studies could not detect ices.

Figure 3.2 shows the column densities of H_2O ice plotted against those of CO_2 ice. The regions showing the CO_2 ice feature also shows the H_2O ice feature, supporting the formation scenario for CO_2 ice based on H_2O ice (Section 1.2.2). This search detects H_2O and CO_2 ices with the column densities of $\sim 10^{17}$ cm^{-2} and $\sim 10^{16}$ cm^{-2}, respectively. Typically, past ice studies for YSOs show the column densities of H_2O ice of $\sim 10^{18}$ cm^{-2} (Gerakines et al. 1999), while those for the diffuse ISM show the H_2O ice column densities of $\sim 10^{16}$–10^{17} cm^{-2} depending on the location of the continuum source (Whittet et al. 2007). Therefore the H_2O ice column densities in the present study are in a range similar to those for the Galactic diffuse ISM rather than the YSOs.

The CO_2/H_2O ice abundance ratios are in a range of 0.05–0.30 and the CO_2/H_2O ratio best-fitted by a linear relation is $CO_2/H_2O = 0.14 \pm 0.01$. Gerakines et al. (1999) and Shimonishi et al. (2010) showed that the CO_2/H_2O ice abundance ratios of massive YSOs in our Galaxy and the LMC to be 0.17 ± 0.03 and 0.36 ± 0.09, respectively. Therefore, the CO_2/H_2O ice abundance ratios obtained for our sample of nearby galaxies are similar to those of our Galaxy rather than those of the LMC. In this study, the superposition of the ices is detected in various kinds of clouds present along the line of sight, while the observations of the YSOs trace the local environments of individual star-forming clouds. Therefore it is interesting that the CO_2/H_2O ice ratios of the nearby galaxies are similar to those of the Galactic YSOs

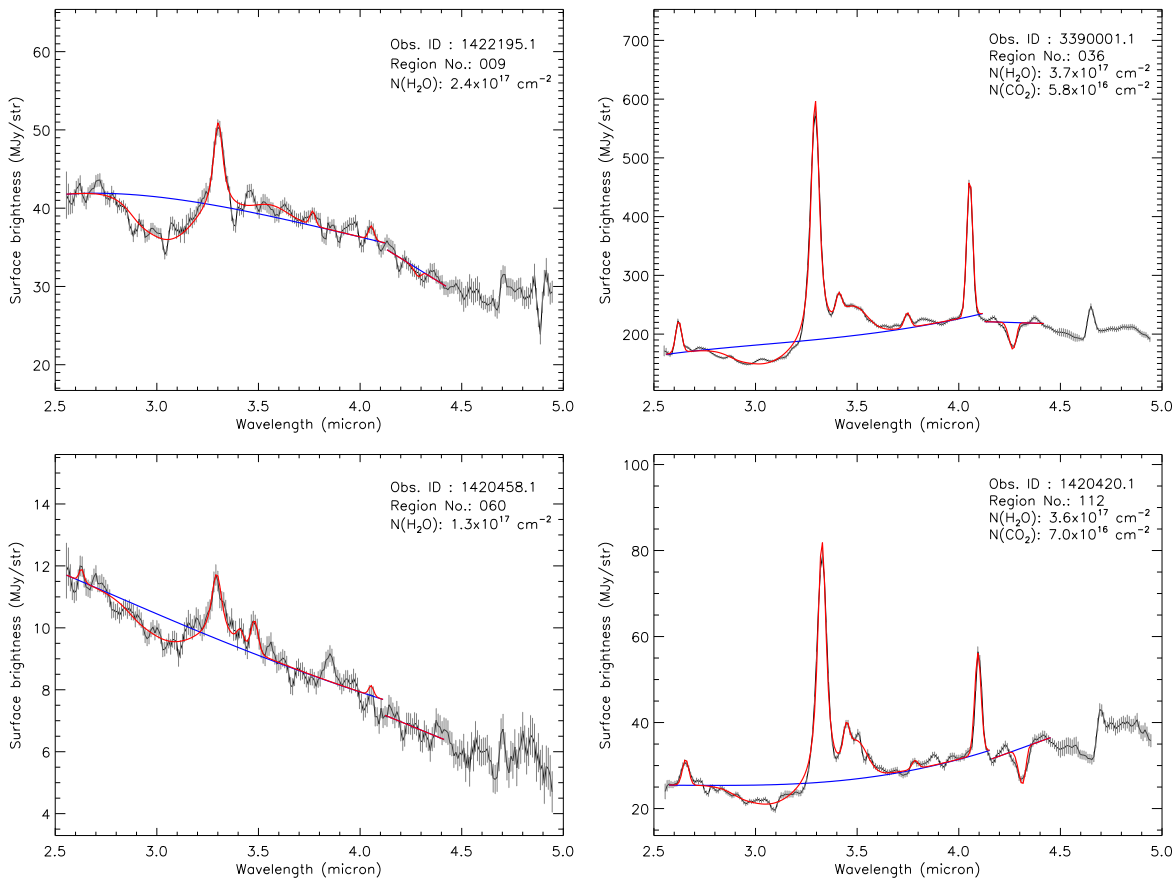

Figure 3.1 Examples of the spectra in which the ices are detected. The blue and red curves represent the best-fit continuum and overall profiles, respectively. The continua are determined separately for H_2O and CO_2 ices.

despite the different situations.

Characteristics of galaxies with detection of ices

Are there any trends for a type of galaxies in which the ices are detected? Figure 3.3 (left) shows the numbers of galaxies where the H_2O and CO_2 ices are detected, which are classified into the three morphological types of the galaxies: late type, early type, and irregular. As can be seen in the figure, the ices are detected in late type galaxies with a high rate, while those are rare in early type and irregular galaxies. As a global trend, late type galaxies have abundant dust and gas as compared to early type galaxies. Therefore, ices are likely to be present in the dust/gas-rich environment. For comparison, a similar presentation for the star forming (U)LIRGs sample (Imanishi et al. 2010) which do not possess any AGN signatures is shown in Fig. 3.3 (right). The (U)LIRGs also indicate a high detection rate of the ices, since (U)LIRGs are also expected to have the gas/dust-rich environment. This trend is consistent with the schematic view of the ice formation (Fig. 1.4); ices are formed on dust grains. Many of the galaxies where the ices are detected indeed show prominent dust lanes in optical images (e.g., M 66, M 104, NGC 2146, and NGC 3628). Thus the dust/gas-rich environment is likely to be important to form the ices.

Are there any differences in detectability of the ices between edge-on and face-on galaxies? In the case of an edge-on galaxy, the hydrogen column density in a line of sight is expected to be much larger than that in a face-on galaxy. Therefore it is likely that the ice features are more easily detected for

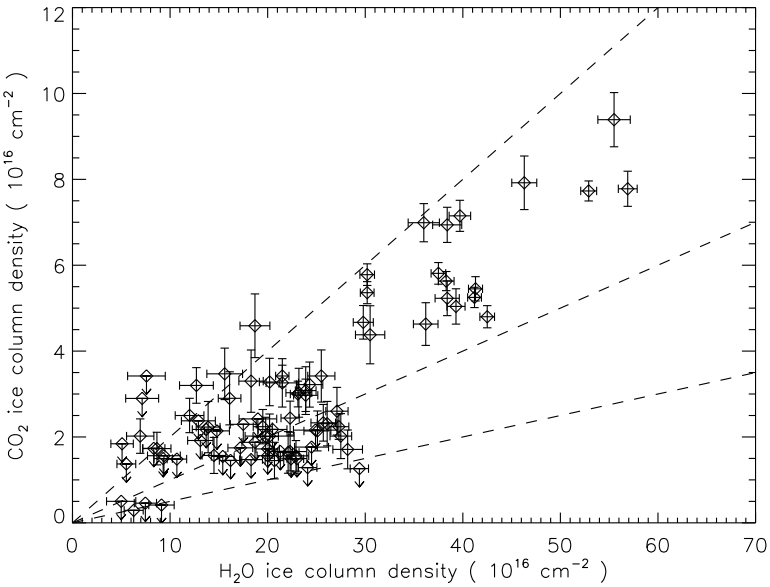

Figure 3.2 Column densities of CO_2 ice plotted against those of H_2O ice. The dashed lines indicate the CO_2/H_2O ice abundance ratios of 0.20, 0.10, and 0.05 from the top to the bottom.

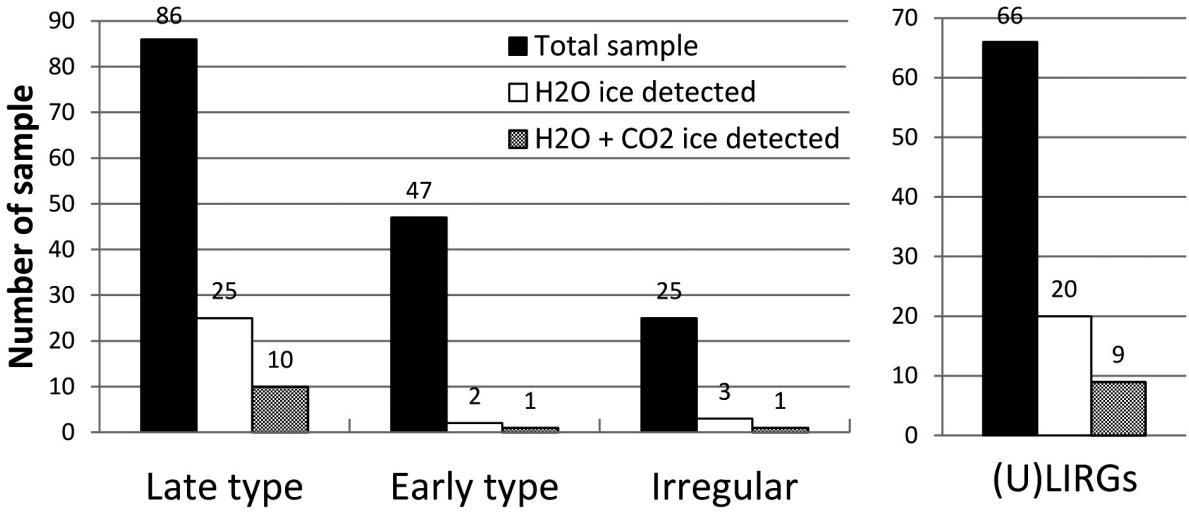

Figure 3.3 (left) Numbers of galaxies with the ices detected, in comparison with the total number of the sample. The sample galaxies are classified into late type, early type, and irregular ones. (right) Similar presentation for the (U)LIRG sample (Imanishi et al. 2010) which do not possess any AGN signatures.

edge-on galaxies than for face-on galaxies. Figure 3.4 shows the numbers of spiral galaxies where the H_2O and CO_2 ices are detected, classified into the two classes based on the disk inclination angles, i: 0–45° and 45–90°. In the figure, the detectability of the ices for the face-on (i=0–45°) galaxies are 0.23±0.08 for H_2O ice and 0.08±0.05 for CO_2 ice, while the detectability of the ices for the edge-on (i=45–90°) galaxies are 0.32±0.06 for H_2O ice and 0.13±0.04 for CO_2 ice. Hence no significant difference is found between edge-on and face-on galaxies, suggesting that the detectability of the ices does not depend on the hydrogen column density.

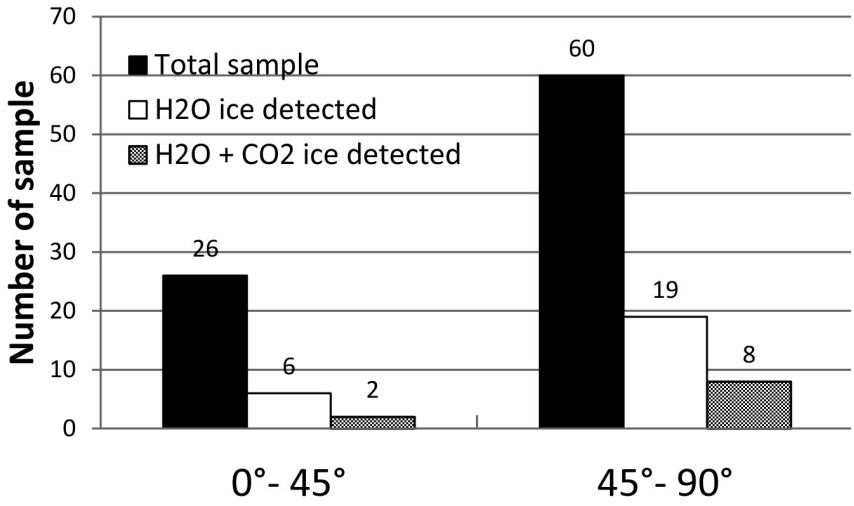

Figure 3.4 Numbers of spiral galaxies where the H_2O and CO_2 ices are detected. They are classified into face-on and edge-on galaxies based on the disk inclination angles (0–45° and 45–90°), which are derived from the minor to major axes ratio using the method in Tully (1988).

Abundances of the ices

The relation between the abundances of the ices and the amount of the ISM is examined. Figures 3.5 (a) and (b) show the column densities of H_2O and the CO_2 ices, respectively, plotted against the PAH 3.3 μm intensities. In the figure, the correlation coefficients are $R = +0.51$ for H_2O ice ($N = 124$) and $R = +0.20$ for CO_2 ice ($N = 53$). Hence, the column densities of H_2O ice significantly correlate with the PAH 3.3 μm intensities, while those of CO_2 ice do not. PAHs are generally thought to represent the neutral ISM mainly in PDRs (Section 1.1). Therefore, the figure indicates that the amount of the neutral ISM correlates with the column density of H_2O ice. This result is consistent with the formation process of H_2O ice; H_2O ice is thought to be formed on dust grains via surface reactions (Section 1.2.2), which suggests that the abundance of H_2O ice depends on the amount of the ISM. The correlation in Fig. 3.5(a) is, however, not tight ($R = +0.51$), indicating that better parameters exist to characterize the presence of H_2O ice than the PAH 3.3 μm intensities. As for the abundance of CO_2 ice, no correlation in Fig. 3.5(b) suggests that there are parameters other than the amount of the ISM to determine the column densities of CO_2 ice. For the CO_2 ice formation, energetic and non-energetic processes are proposed (Section 1.2.2). Therefore the UV radiation environment, which causes the energetic process, may be a key to the CO_2 ice formation. Alternatively, it is also possible that CO_2 ice is not present in PDRs.

Figure 3.6 shows the fractions of the regions with H_2O and CO_2 ices detected, only H_2O ice detected, and ice non-detected plotted against the Brα line intensities, which is a probe of the star-formation activity. In the figure, the 3σ upper limits of the Brα intensities are used to define the regions with non-detection of Brα. The figure clearly displays that the regions where CO_2 ice is detected show stronger Brα intensities than those where only H_2O ice is detected or ices are non-detected. This result suggests that star-formation activities may be essential to the formation process of CO_2 ice, and that the energetic process may be dominant in the CO_2 ice formation. Figures 3.7 (a) and (b) show the column densities of H_2O ice and CO_2 ice, respectively, plotted against the Brα intensities. Figure 3.7 (b), however, does not show a significant correlation between them ($R = +0.34$, $N = 49$), although the correlation coefficient is slightly better than that in Fig. 3.5 (b). Furthermore, the column densities of H_2O ice significantly

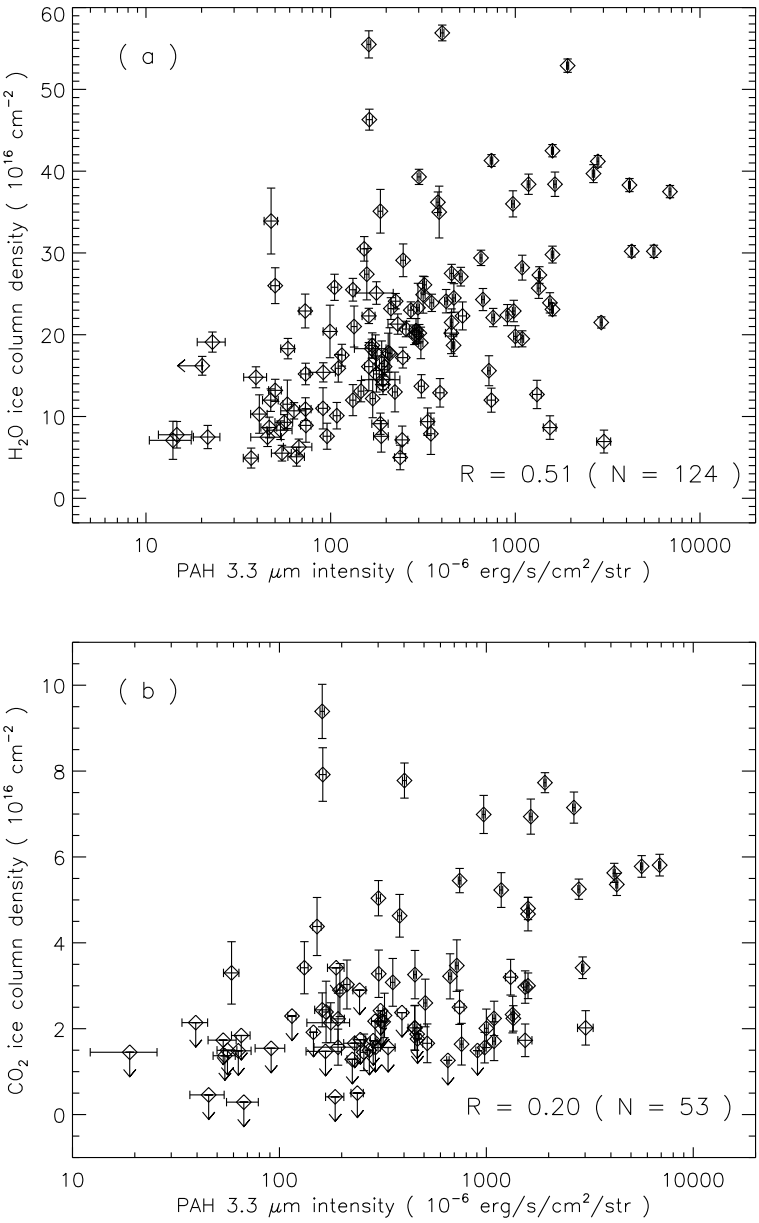

Figure 3.5 Column densities of (a) H_2O and (b) CO_2 ices plotted against the PAH 3.3 μm intensities. The correlation coefficient and the number of samples for each plot are shown at the bottom right.

correlate with the Brα intensities in Fig. 3.7 (a). This correlation, however, appears to be strange because Brα represents HII regions, which are harsh for the survival of H_2O ice. This situation may be interpreted indirectly via the gas density; H_2O ice is formed in a relatively dense region and star formation is likely to be associated with such a region. Figure 3.8 shows the PAH 3.3 μm intensities plotted against the Brα intensities, which shows an excellent correlation ($R = +0.84$, $N = 91$). This correlation explains the overall similarity between Figs. 3.5 and 3.7. In Fig. 3.3, early type and irregular galaxies with detection of CO_2 ice are Centaurus A (Cen A) and M 82, respectively. Cen A is known to be categorized as a peculiar early-type galaxy which has a prominent dust lane and star forming activities. M 82 is a well studied active starburst galaxy. The detections of CO_2 ice in these galaxies also support the importance of UV radiation for the CO_2 ice formation.

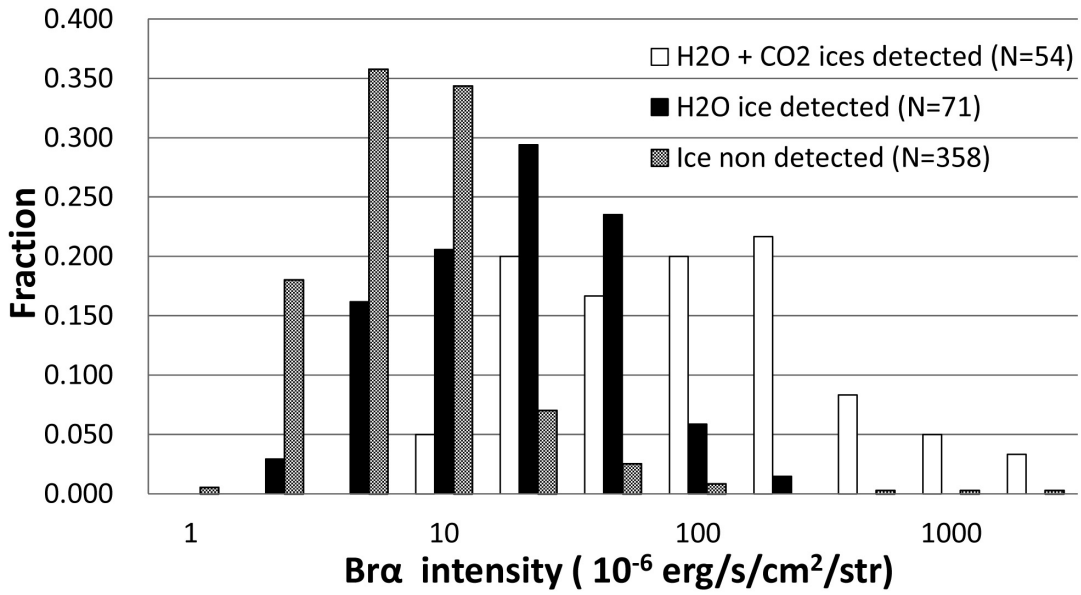

Figure 3.6 Fractions of the spectra with H_2O and CO_2 ices detected, only H_2O ice detected, and ice non-detected, plotted against the Brα intensities.

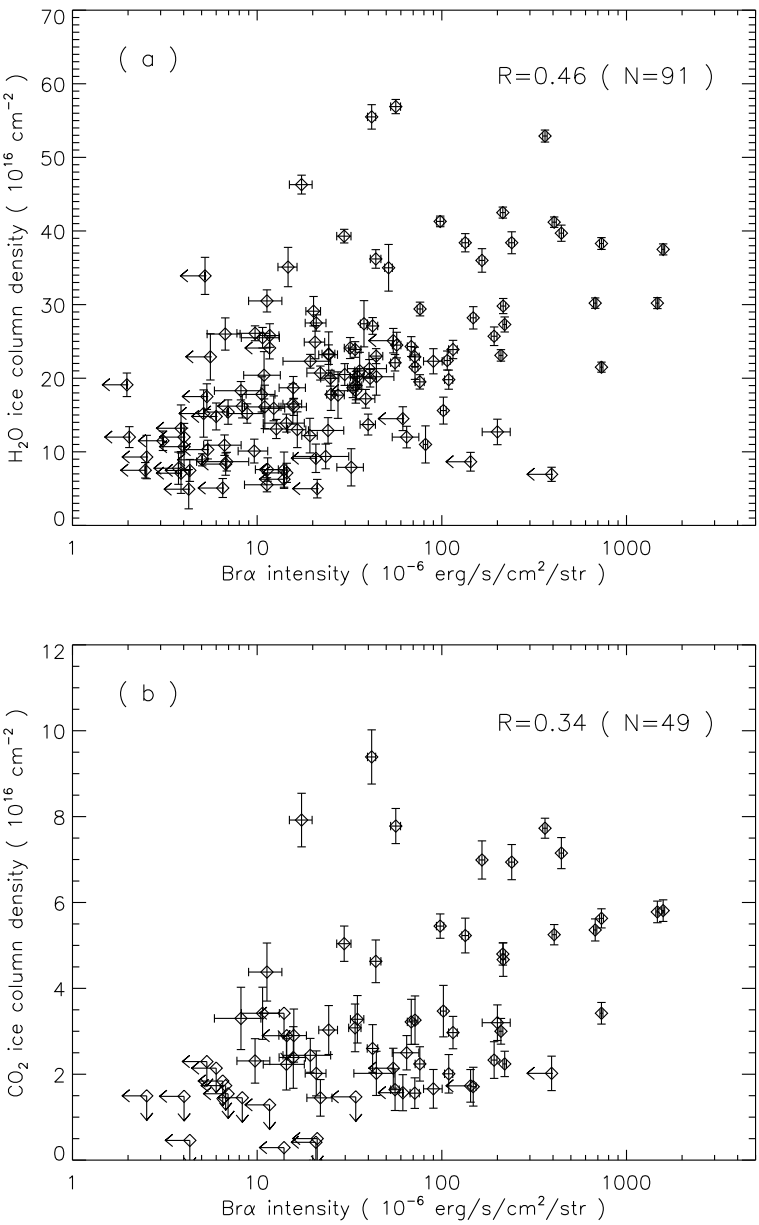

Figure 3.7 Column densities of (a) H_2O ice and (b) CO_2 ice plotted against the Brα line intensities. The correlation coefficient and the number of the sample for each plot are shown at the top right.

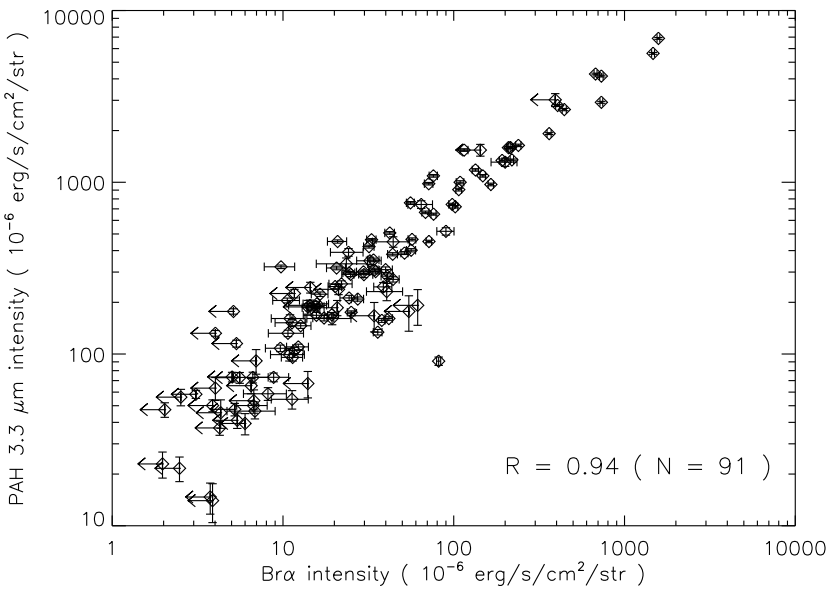

Figure 3.8 PAH 3.3 μm intensities plotted against the Brα intensities. The correlation coefficient and the number of the sample are shown at the bottom right.

Table 3.1 Summary of the spectral fitting results obtained for the regions where the ices are detected.

No.	Obs. ID	Name	RA , DEC	Size	Continuum 3.05 μm, 4.27 μm		$N(H_2O)$	$N(CO_2)$	PAH 3.3 μm	Brα	Brβ	Region[a]
				$'' \times ''$	MJy/str		10^{16} cm^{-2}		10^{-6} erg/s/cm^2/str			
1	1420103.1	Cen A	201.3735 , -43.02028	5 × 4.4	23.0 ± 0.9	17.2 ± 1.2	7.6 ± 1.9	< 3.4	188 ± 17	< 14	19 ± 6	
2	1420103.1	Cen A	201.37201 , -43.01975	5 × 4.4	28.6 ± 1.0	20.8 ± 1.2	7.1 ± 1.7	< 2.9	244 ± 18	< 14	< 85	
3	1420103.1	Cen A	201.37051 , -43.01922	5 × 4.4	37.1 ± 1.1	27.8 ± 1.3	5.0 ± 1.5	< 0.5	238 ± 16	< 21	< 79	
4	1420103.1	Cen A	201.369 , -43.01869	5 × 4.4	53.0 ± 1.3	38.8 ± 1.5	9.1 ± 1.3	< 0.4	186 ± 19	< 21	< 76	
5	1420103.1	Cen A	201.36751 , -43.01815	5 × 4.4	87.3 ± 1.9	71.9 ± 2.2	18.3 ± 1.2	< 1.5	167 ± 33	< 34	< 43	
6	1420103.1	Cen A	201.36601 , -43.01762	5 × 4.4	137.2 ± 2.8	157.6 ± 4.2	14.5 ± 1.2	1.6 ± 0.4	192 ± 45	< 62	< 137	
7	1420103.1	Cen A	201.36452 , -43.01709	5 × 4.4	132.8 ± 2.6	126.3 ± 3.4	25.1 ± 1.4	2.1 ± 0.5	177 ± 41	< 55	84 ± 24	
8	1420103.1	Cen A	201.36302 , -43.01656	5 × 4.4	74.4 ± 1.6	54.4 ± 1.8	21.3 ± 1.2	< 1.7	231 ± 27	41 ± 10	< 68	
9	1422195.1	Cen A	201.3614 , -43.02091	5 × 7.3	41.3 ± 0.7	32.4 ± 0.8	24.1 ± 0.9	< 1.3	225 ± 13	< 12	< 12	
10	1422195.1	Cen A	201.36391 , -43.02179	5 × 7.3	56.5 ± 0.9	46.0 ± 1.1	22.3 ± 0.9	2.4 ± 0.4	161 ± 13	19 ± 6	< 80	
11	1422195.1	Cen A	201.36639 , -43.02267	5 × 7.3	40.7 ± 0.7	31.0 ± 0.8	20.7 ± 1.0	1.5 ± 0.4	256 ± 11	22 ± 3	17 ± 6	
12	1422195.1	Cen A	201.3689 , -43.02355	5 × 7.3	26.9 ± 0.5	22.5 ± 0.7	23.0 ± 1.0	< 1.5	272 ± 10	44 ± 4	< 32	
13	1422195.1	Cen A	201.37138 , -43.02443	5 × 7.3	19.0 ± 0.4	16.1 ± 0.6	20.0 ± 1.2	< 1.7	284 ± 9	41 ± 3	< 9	
14	5125033.1	CIRCINUS	213.29572 , -65.34059	5 × 4.4	54.9 ± 1.5	60.1 ± 1.6	22.3 ± 1.7	1.7 ± 0.5	518 ± 26	90 ± 10	51 ± 7	
15	5125033.1	CIRCINUS	213.29321 , -65.33996	5 × 4.4	151.7 ± 4.1	237.4 ± 5.4	12.7 ± 1.7	3.2 ± 0.4	1310 ± 73	200 ± 35	< 363	
16	5125033.1	CIRCINUS	213.2907 , -65.33934	5 × 4.4	529.0 ± 14.4	1401.2 ± 32.9	6.9 ± 1.4	2.0 ± 0.4	3020 ± 262	< 393	< 117	
17	5125033.1	CIRCINUS	213.28819 , -65.33871	5 × 4.4	270.6 ± 7.3	471.2 ± 11.0	8.7 ± 1.4	1.7 ± 0.4	1540 ± 121	< 143	< 120	
18	5125033.1	CIRCINUS	213.28571 , -65.33808	5 × 4.4	79.9 ± 2.2	88.4 ± 2.1	12.0 ± 1.5	2.5 ± 0.4	742 ± 38	65 ± 11	42 ± 10	
19	5200011.1	ESO 264-36	160.78542 , -46.21429	3 × 21.9	5.2 ± 0.2	3.8 ± 0.3	11.5 ± 3.0		58 ± 3	< 3	7 ± 0	
20	1422158.1	ESO 495-21	129.06175 , -26.41076	5 × 11.7	6.0 ± 0.2	5.6 ± 0.4	27.4 ± 3.1		157 ± 4	38 ± 2	16 ± 1	
21	1422178.1	M 063	198.95193 , 42.0293	5 × 8.8	15.8 ± 0.3	10.8 ± 0.5	14.8 ± 1.3	< 2.1	39 ± 6	< 6	11 ± 2	
22	1422178.1	M 063	198.95471 , 42.02801	5 × 8.8	25.1 ± 0.5	16.3 ± 0.5	9.3 ± 0.9	< 1.5	56 ± 6	< 3	< 12	
23	1422178.1	M 063	198.95749 , 42.02671	5 × 8.8	11.9 ± 0.3	7.9 ± 0.4	12.0 ± 1.4		47 ± 5	< 2	< 42	
24	1422178.1	M 063	198.96027 , 42.02541	5 × 8.8	7.1 ± 0.3	5.2 ± 0.4	10.3 ± 2.4		41 ± 4	< 5	< 4	
25	1422173.1	M 064	194.18329 , 21.67914	5 × 8.8	12.5 ± 0.3	7.9 ± 0.4	8.7 ± 1.3		47 ± 5	7 ± 2	< 7	
26	1422176.1	M 064	194.17598 , 21.68406	5 × 11.7	11.3 ± 0.3	8.2 ± 0.4	15.2 ± 1.3		73 ± 4	9 ± 2	< 18	
27	1420435.1	M 066	170.06332 , 12.99328	5 × 5.8	24.1 ± 0.5	16.9 ± 0.6	8.3 ± 1.1	< 1.7	54 ± 8	< 7	< 15	
28	1420435.1	M 066	170.0618 , 12.99394	5 × 5.8	22.5 ± 0.5	15.1 ± 0.6	5.1 ± 1.2	< 1.8	65 ± 7	< 7	< 34	
29	5125030.1	M 077	40.66718 , -0.01384	5 × 4.4	54.7 ± 1.6	61.8 ± 1.8	20.2 ± 2.5	2.0 ± 0.5	450 ± 32	44 ± 11	< 56	
30	5125030.1	M 077	40.67298 , -0.01199	5 × 4.4	51.7 ± 1.6	59.0 ± 1.8	9.4 ± 1.7	< 1.6	335 ± 27	24 ± 8	< 32	
31	5125030.1	M 077	40.67413 , -0.01162	5 × 4.4	29.2 ± 1.1	26.4 ± 1.2	12.9 ± 1.7	< 2.4	391 ± 20	24 ± 5	19 ± 6	
32	5125030.1	M 077	40.67529 , -0.01125	5 × 4.4	17.1 ± 0.9	15.2 ± 1.1	7.9 ± 2.5		349 ± 18	32 ± 5	17 ± 5	
33	3390001.1	M 082	148.95615 , 69.68111	3 × 4.4	35.1 ± 0.5	37.7 ± 0.7	27.3 ± 1.0	2.2 ± 0.3	1350 ± 16	219 ± 5	80 ± 1	A1
34	3390001.1	M 082	148.95905 , 69.68042	3 × 4.4	94.6 ± 1.1	103.5 ± 1.5	21.5 ± 0.7	3.4 ± 0.3	2920 ± 38	732 ± 14	276 ± 1	A2

Table 3.1 Continued

No.	Obs. ID	Name	RA , DEC	Size	Continuum 3.05 μm, 4.27 μm		$N(H_2O)$	$N(CO_2)$	PAH 3.3 μm	Brα	Brβ	Region[a]
				$'' \times ''$	MJy/str		10^{16} cm^{-2}		10^{-6} erg/s/cm^2/str			
35	3390001.1	M 082	148.96194 , 69.67974	3 × 4.4	189.2 ± 2.0	213.3 ± 2.9	30.2 ± 0.7	5.8 ± 0.3	5630 ± 71	1470 ± 28	714 ± 2	A3
36	3390001.1	M 082	148.96484 , 69.67905	3 × 4.4	182.9 ± 1.9	219.7 ± 3.0	37.5 ± 0.7	5.8 ± 0.3	6880 ± 83	1580 ± 30	836 ± 2	A4
37	3390001.1	M 082	148.96773 , 69.67836	3 × 4.4	98.6 ± 1.1	111.6 ± 1.6	30.2 ± 0.7	5.4 ± 0.3	4270 ± 47	677 ± 14	371 ± 1	A5
38	3390001.1	M 082	148.97063 , 69.67767	3 × 4.4	40.7 ± 0.5	40.3 ± 0.7	23.1 ± 0.8	3.0 ± 0.3	1590 ± 18	209 ± 5	117 ± 1	A6
39	3390001.1	M 082	148.97351 , 69.67699	3 × 4.4	20.4 ± 0.3	18.0 ± 0.5	29.4 ± 0.9	< 1.3	652 ± 9	76 ± 3	43 ± 1	A7
40	3390001.1	M 082	148.97641 , 69.6763	3 × 4.4	11.5 ± 0.3	10.7 ± 0.4	18.7 ± 1.3	< 1.9	463 ± 7	33 ± 2	26 ± 1	A8
41	3390001.1	M 082	148.97929 , 69.67561	3 × 4.4	7.6 ± 0.3	7.1 ± 0.4	23.3 ± 3.0		297 ± 5	24 ± 2	14 ± 1	A9
42	3390002.1	M 082	148.96687 , 69.68422	3 × 7.3	17.5 ± 0.4	17.8 ± 0.6	24.3 ± 1.4	3.2 ± 0.5	668 ± 12	68 ± 3	45 ± 1	C1
43	3390002.1	M 082	149.02533 , 69.67082	3 × 7.3	36.9 ± 0.6	41.3 ± 0.9	29.8 ± 1.0	4.7 ± 0.4	1590 ± 24	215 ± 7	98 ± 1	C2
44	3390002.1	M 082	148.99026 , 69.67886	3 × 7.3	57.4 ± 0.9	70.4 ± 1.4	39.7 ± 1.1	7.2 ± 0.4	2650 ± 40	444 ± 12	187 ± 2	C3
45	3390002.1	M 082	149.00195 , 69.67618	3 × 7.3	37.0 ± 0.6	36.5 ± 0.8	38.4 ± 1.2	5.2 ± 0.4	1180 ± 20	134 ± 6	64 ± 2	C4
46	3390002.1	M 082	149.01364 , 69.6735	3 × 7.3	14.6 ± 0.4	11.5 ± 0.5	24.9 ± 2.3	< 2.2	317 ± 8	21 ± 3	22 ± 2	C5
47	3390002.1	M 082	149.02533 , 69.67082	3 × 7.3	7.8 ± 0.3	6.1 ± 0.4	15.2 ± 2.2		177 ± 6	< 5	6 ± 2	C6
48	3390002.2	M 082	148.9912 , 69.68149	3 × 10.2	20.5 ± 0.4	16.1 ± 0.5	26.1 ± 1.0	2.3 ± 0.5	322 ± 8	10 ± 2	20 ± 2	
49	3390002.2	M 082	148.97958 , 69.68422	3 × 10.2	40.2 ± 0.6	33.6 ± 0.7	22.9 ± 1.3	1.6 ± 0.4	981 ± 17	71 ± 4	42 ± 3	
50	3390002.2	M 082	148.96797 , 69.68694	3 × 10.2	17.2 ± 0.3	15.0 ± 0.5	27.1 ± 1.1	2.6 ± 0.6	507 ± 9	42 ± 3	22 ± 2	
51	3390002.2	M 082	148.95634 , 69.68967	3 × 10.2	7.3 ± 0.3	5.7 ± 0.4	29.1 ± 2.0		247 ± 7	20 ± 2	< 4	
52	3390003.1	M 082	148.94209 , 69.67899	3 × 7.3	21.7 ± 0.4	17.7 ± 0.5	27.5 ± 1.1	2.0 ± 0.5	452 ± 10	21 ± 3	< 33	B1
53	3390003.1	M 082	149.00002 , 69.66532	3 × 7.3	51.4 ± 0.8	46.5 ± 1.0	23.9 ± 1.2	3.0 ± 0.4	1540 ± 27	115 ± 6	61 ± 4	B2
54	3390003.1	M 082	148.96529 , 69.67352	3 × 7.3	35.6 ± 0.6	30.2 ± 0.7	19.5 ± 1.0	2.2 ± 0.4	1090 ± 20	76 ± 4	49 ± 2	B3
55	3390003.1	M 082	148.97685 , 69.67079	3 × 7.3	20.9 ± 0.4	18.6 ± 0.5	22.1 ± 1.1	1.6 ± 0.5	759 ± 13	56 ± 3	31 ± 1	B4
56	3390003.1	M 082	148.98843 , 69.66805	3 × 7.3	11.2 ± 0.3	9.9 ± 0.4	24.1 ± 1.4		422 ± 8	32 ± 2	13 ± 2	B5
57	3390003.1	M 082	149.00002 , 69.66532	3 × 7.3	6.1 ± 0.3	5.8 ± 0.4	13.0 ± 2.4		223 ± 7	17 ± 2	11 ± 1	B6
58	1420415.1	M 083	204.25671 , -29.86392	5 × 8.8	13.6 ± 0.3	10.1 ± 0.5	17.5 ± 1.3	< 2.3	115 ± 5	< 5	< 5	
59	1420415.1	M 083	204.25414 , -29.86298	5 × 8.8	22.3 ± 0.4	17.6 ± 0.5	20.2 ± 1.1	3.3 ± 0.6	302 ± 9	35 ± 3	19 ± 3	
60	1420458.1	M 090	189.20909 , 13.16432	5 × 11.7	10.3 ± 0.2	6.8 ± 0.4	13.2 ± 1.4		50 ± 4	< 4	8 ± 2	
61	1420458.1	M 090	189.20607 , 13.16567	5 × 11.7	7.2 ± 0.2	4.9 ± 0.3	7.8 ± 1.6		15 ± 3	< 4	7 ± 1	
62	1422152.1	M 094	192.71777 , 41.12083	5 × 7.3	38.4 ± 0.7	25.2 ± 0.8	10.7 ± 1.0	< 1.5	63 ± 10	< 4	25 ± 5	
63	1422171.1	M 104	189.994 , -11.62299	5 × 7.3	27.1 ± 0.6	16.8 ± 0.7	7.5 ± 1.1	< 0.5	46 ± 9	< 4	< 11	
64	1420372.1	M 106	184.74185 , 47.30609	5 × 11.7	10.1 ± 0.2	6.9 ± 0.3	4.9 ± 1.2		37 ± 3	< 4	< 8	
65	1422159.1	M 106	184.73779 , 47.30422	5 × 8.8	22.2 ± 0.4	18.0 ± 0.6	16.2 ± 1.2	< 1.5	< 20	< 8	< 25	
66	1422159.1	M 106	184.74074 , 47.30282	5 × 8.8	26.8 ± 0.5	19.6 ± 0.6	5.5 ± 1.0	< 1.4	55 ± 7	11 ± 3	< 33	
67	1422187.1	NGC 0253	11.88683 , -25.28732	5 × 5.8	91.4 ± 0.8	121.0 ± 1.5	52.9 ± 0.8	7.7 ± 0.2	1920 ± 25	362 ± 10	184 ± 2	N1
68	1422187.1	NGC 0253	11.88522 , -25.28803	5 × 5.8	47.2 ± 0.5	48.1 ± 0.7	41.3 ± 0.7	5.5 ± 0.3	743 ± 11	98 ± 4	68 ± 2	N2
69	1422187.1	NGC 0253	11.88361 , -25.28873	5 × 5.8	26.5 ± 0.4	23.5 ± 0.5	39.3 ± 0.9	5.0 ± 0.4	301 ± 7	30 ± 3	26 ± 1	N3

Table 3.1 Continued

No.	Obs. ID	Name	RA , DEC	Size	Continuum 3.05 μm, 4.27 μm		$N(H_2O)$	$N(CO_2)$	PAH 3.3 μm	Brα	Brβ	Region[a]
				$'' \times ''$	MJy/str		10^{16} cm^{-2}		10^{-6} erg/s/cm^2/str			
70	1422187.1	NGC 0253	11.882 , -25.28943	5 × 5.8	17.7 ± 0.3	13.9 ± 0.5	25.5 ± 1.4	3.4 ± 0.6	132 ± 6	11 ± 2	11 ± 3	N4
71	1422187.1	NGC 0253	11.88038 , -25.29014	5 × 5.8	14.6 ± 0.3	11.2 ± 0.5	18.3 ± 1.3	3.3 ± 0.7	59 ± 5	8 ± 2	< 7	N5
72	1422196.1	NGC 0253	11.88994 , -25.28805	5 × 5.8	107.2 ± 1.0	136.1 ± 1.7	41.2 ± 0.7	5.3 ± 0.2	2800 ± 33	406 ± 11	220 ± 2	S1
73	1422196.1	NGC 0253	11.88833 , -25.28876	5 × 5.8	152.5 ± 1.4	201.1 ± 2.5	38.3 ± 0.8	5.6 ± 0.2	4150 ± 49	732 ± 18	353 ± 3	S2
74	1422196.1	NGC 0253	11.88671 , -25.28948	5 × 5.8	72.7 ± 0.7	75.8 ± 1.1	42.5 ± 0.8	4.8 ± 0.3	1590 ± 21	214 ± 7	100 ± 2	S3
75	1422196.1	NGC 0253	11.8851 , -25.29019	5 × 5.8	30.1 ± 0.4	29.4 ± 0.6	56.9 ± 1.0	7.8 ± 0.4	402 ± 9	56 ± 3	43 ± 2	S4
76	1422196.1	NGC 0253	11.88349 , -25.29091	5 × 5.8	18.2 ± 0.4	16.8 ± 0.5	46.3 ± 1.3	7.9 ± 0.6	162 ± 6	17 ± 2	< 9	S5
77	1422196.1	NGC 0253	11.88187 , -25.29162	5 × 5.8	15.8 ± 0.3	14.0 ± 0.5	30.5 ± 1.5	4.4 ± 0.7	152 ± 7	11 ± 2	< 5	S6
78	1422197.1	NGC 0253	11.88943 , -25.28384	5 × 8.8	20.0 ± 0.4	16.5 ± 0.6	23.2 ± 1.3	3.0 ± 0.6	212 ± 8	24 ± 3	< 9	
79	1422197.1	NGC 0253	11.887 , -25.28489	5 × 8.8	22.3 ± 0.4	18.5 ± 0.6	20.0 ± 1.1	< 1.6	291 ± 9	25 ± 3	17 ± 3	
80	1422197.1	NGC 0253	11.88458 , -25.28595	5 × 8.8	18.9 ± 0.4	14.6 ± 0.5	16.1 ± 1.2	2.9 ± 0.6	196 ± 7	16 ± 3	< 61	
81	1422197.1	NGC 0253	11.88216 , -25.28701	5 × 8.8	15.0 ± 0.4	12.3 ± 0.5	18.7 ± 1.5	2.4 ± 0.7	168 ± 7	16 ± 3	< 8	
82	3390006.1	NGC 0253	11.88167 , -25.29307	3 × 10.2	7.4 ± 0.3	5.3 ± 0.4	33.9 ± 4.0		48 ± 4	< 5	17 ± 1	
83	3390006.1	NGC 0253	11.8849 , -25.29166	3 × 10.2	11.8 ± 0.3	9.5 ± 0.5	22.9 ± 2.1		73 ± 5	< 6	< 9	
84	3390006.1	NGC 0253	11.88814 , -25.29024	3 × 10.2	23.6 ± 0.4	20.7 ± 0.6	36.2 ± 1.3	4.6 ± 0.5	381 ± 8	44 ± 3	19 ± 2	
85	3390006.1	NGC 0253	11.89137 , -25.28883	3 × 10.2	21.4 ± 0.4	16.6 ± 0.5	23.9 ± 1.1	3.1 ± 0.6	353 ± 9	34 ± 3	28 ± 1	
86	3390006.1	NGC 0253	11.91401 , -25.27892	5 × 11.7	10.6 ± 0.3	7.6 ± 0.4	10.9 ± 1.4		73 ± 5	7 ± 2	7 ± 2	
87	3390006.1	NGC 0253	11.91725 , -25.27751	5 × 11.7	9.6 ± 0.3	8.1 ± 0.4	21.0 ± 2.5		134 ± 5	36 ± 2	< 15	
88	3390006.1	NGC 0253	11.92048 , -25.27609	5 × 11.7	9.0 ± 0.3	7.6 ± 0.4	12.2 ± 2.4		169 ± 6	19 ± 2	< 17	
89	1420462.1	NGC 1097	41.57941 , -30.27546	5 × 4.4	11.4 ± 0.4	8.5 ± 0.6	16.1 ± 3.0		161 ± 8	11 ± 2	13 ± 2	A3
90	1420462.1	NGC 1097	41.58112 , -30.27478	5 × 4.4	23.5 ± 0.6	17.3 ± 0.7	13.7 ± 1.4	< 2.2	310 ± 12	40 ± 4	< 19	A4
91	1420462.1	NGC 1097	41.58282 , -30.27411	5 × 4.4	34.8 ± 0.8	24.1 ± 0.9	17.2 ± 1.3	< 1.7	246 ± 15	39 ± 5	< 26	A5
92	1420462.1	NGC 1097	41.58282 , -30.27411	5 × 4.4	48.1 ± 1.0	33.1 ± 1.1	15.4 ± 1.2	< 1.5	91 ± 15	< 7	< 21	A6
93	1420462.1	NGC 1097	41.58282 , -30.27411	5 × 4.4	35.5 ± 0.8	25.6 ± 0.9	13.9 ± 1.2	2.2 ± 0.6	192 ± 14	14 ± 4	35 ± 4	A7
94	1420462.1	NGC 1097	41.58282 , -30.27411	5 × 4.4	22.1 ± 0.6	17.7 ± 0.7	20.5 ± 1.5	< 2.2	290 ± 11	30 ± 4	36 ± 2	A8
95	1420462.1	NGC 1097	41.58282 , -30.27411	5 × 4.4	10.7 ± 0.4	8.9 ± 0.6	20.4 ± 3.2		99 ± 8	11 ± 2	10 ± 3	A9
96	1420467.1	NGC 1566	65.00354 , -54.93955	5 × 11.7	9.0 ± 0.2	6.2 ± 0.4	7.5 ± 1.4		22 ± 4	< 2	< 12	
97	1420467.1	NGC 1566	65.00798 , -54.93756	5 × 11.7	6.1 ± 0.2	4.0 ± 0.4	7.1 ± 2.3		14 ± 4	< 4	< 9	
98	1420398.1	NGC 1614	68.4993 , -8.57971	5 × 11.7	12.7 ± 0.3	14.5 ± 0.5	21.5 ± 1.7	3.3 ± 0.6	452 ± 7	72 ± 3	35 ± 0	
99	1420357.1	NGC 1808	76.9245 , -37.51493	5 × 5.8	10.5 ± 0.3	9.0 ± 0.5	17.8 ± 2.4		205 ± 7	11 ± 2	19 ± 1	
100	1420357.1	NGC 1808	76.92652 , -37.51465	5 × 5.8	39.0 ± 0.7	36.6 ± 0.9	19.8 ± 1.3	2.0 ± 0.4	1000 ± 21	109 ± 6	66 ± 2	
101	1420357.1	NGC 1808	76.92854 , -37.51437	5 × 5.8	43.3 ± 0.8	41.4 ± 1.0	25.7 ± 1.3	2.3 ± 0.4	1340 ± 26	192 ± 7	108 ± 2	
102	1420357.1	NGC 1808	76.93055 , -37.51409	5 × 5.8	12.7 ± 0.4	10.6 ± 0.5	19.0 ± 1.9	< 2.4	308 ± 8	34 ± 3	19 ± 1	
103	5200185.1	NGC 1961	85.51889 , 69.37749	5 × 11.7	11.9 ± 0.2	7.7 ± 0.4	19.1 ± 1.2		23 ± 4	< 2	7 ± 2	
104	1420400.1	NGC 2146	94.6496 , 78.35429	5 × 5.8	7.8 ± 0.3	7.2 ± 0.4	35.1 ± 2.7		186 ± 6	15 ± 2	< 4	

Table 3.1 Continued

No.	Obs. ID	Name	RA , DEC	Size	Continuum 3.05 μm, 4.27 μm		$N(H_2O)$	$N(CO_2)$	PAH 3.3 μm	Brα	Brβ	Region[a]
				$'' \times ''$	MJy/str		10^{16} cm^{-2}		10^{-6} erg/s/cm^2/str			
105	1420400.1	NGC 2146	94.6576 , 78.35415	5 × 5.8	15.1 ± 0.4	15.7 ± 0.6	24.5 ± 1.7	< 1.8	465 ± 9	57 ± 3	35 ± 1	
106	1420400.1	NGC 2146	94.66559 , 78.35401	5 × 5.8	25.6 ± 0.5	29.2 ± 0.8	28.2 ± 1.5	1.7 ± 0.5	1090 ± 19	148 ± 5	87 ± 1	
107	1420400.1	NGC 2146	94.67358 , 78.35387	5 × 5.8	20.2 ± 0.4	21.8 ± 0.7	22.4 ± 1.3	< 1.5	906 ± 17	107 ± 4	50 ± 1	
108	1420400.1	NGC 2146	94.68158 , 78.35373	5 × 5.8	9.4 ± 0.3	8.9 ± 0.5	35.0 ± 3.2		387 ± 8	52 ± 2	31 ± 1	
109	1422184.1	NGC 3079	150.48918 , 55.67777	5 × 11.7	9.7 ± 0.2	7.8 ± 0.4	25.8 ± 1.6		105 ± 4	12 ± 1	8 ± 1	
110	1422184.1	NGC 3079	150.49426 , 55.67625	5 × 11.7	7.0 ± 0.2	5.1 ± 0.4	12.0 ± 1.9		132 ± 5	< 4	< 8	
111	1420420.1	NGC 3256	156.96674 , -43.9053	5 × 5.8	6.0 ± 0.3	7.2 ± 0.5	17.7 ± 3.2		209 ± 6	27 ± 2	17 ± 1	
112	1420420.1	NGC 3256	156.96484 , -43.90441	5 × 5.8	25.5 ± 0.5	34.0 ± 0.9	36.0 ± 1.6	7.0 ± 0.4	971 ± 17	165 ± 6	87 ± 1	
113	1420420.1	NGC 3256	156.96297 , -43.90353	5 × 5.8	41.2 ± 0.7	49.5 ± 1.2	38.4 ± 1.5	6.9 ± 0.4	1640 ± 27	239 ± 8	145 ± 1	
114	1420420.1	NGC 3256	156.96107 , -43.90265	5 × 5.8	14.6 ± 0.4	16.5 ± 0.6	15.6 ± 1.8	3.5 ± 0.6	720 ± 12	102 ± 4	71 ± 0	
115	5200009.1	NGC 3256	156.96873 , -43.90392	3 × 21.9	4.5 ± 0.2	4.4 ± 0.3	17.8 ± 2.2		175 ± 3	25 ± 1	18 ± 0	
116	1420410.1	NGC 3628	170.07359 , 13.58808	3 × 14.6	6.1 ± 0.2	4.8 ± 0.3	28.0 ± 2.2		50 ± 3	7 ± 1	< 3	
117	1420410.1	NGC 3628	170.06903 , 13.59005	3 × 14.6	12.9 ± 0.3	12.7 ± 0.4	55.5 ± 1.7	9.4 ± 0.6	161 ± 4	42 ± 2	27 ± 1	
118	1420369.1	NGC 4041	180.55576 , 62.13704	5 × 11.7	7.6 ± 0.2	6.0 ± 0.4	15.9 ± 1.7		110 ± 4	12 ± 2	< 9	
119	1420369.1	NGC 4041	180.55083 , 62.13931	5 × 11.7	8.0 ± 0.2	5.9 ± 0.4	10.1 ± 1.6		108 ± 5	10 ± 2	< 8	
120	5200377.1	NGC 4157	182.7644 , 50.48415	5 × 11.7	10.1 ± 0.2	7.3 ± 0.3	8.9 ± 2.1		74 ± 5	< 5	8 ± 2	
121	1420098.1	NGC 4697	192.15015 , -5.80019	5 × 5.8	51.5 ± 1.0	31.1 ± 0.9	6.3 ± 1.0	< 0.3	67 ± 12	< 14	< 23	
122	5200514.2	NGC 5248	204.38203 , 8.88497	5 × 11.7	14.1 ± 0.3	10.2 ± 0.4	13.1 ± 1.3	< 1.9	146 ± 5	13 ± 2	16 ± 2	
123	5200514.2	NGC 5248	204.38506 , 8.88369	5 × 11.7	8.7 ± 0.2	6.1 ± 0.4	7.6 ± 1.6		96 ± 5	11 ± 2	18 ± 1	
124	1422153.1	NGC 5253	204.98193 , -31.64125	5 × 11.7	6.5 ± 0.2	9.8 ± 0.4	11.0 ± 2.5		91 ± 5	82 ± 2	40 ± 0	
125	1420416.2	NGC 5953	233.63341 , 15.19276	5 × 11.7	7.8 ± 0.2	6.4 ± 0.4	16.5 ± 2.7		189 ± 5	16 ± 2	12 ± 1	

[a] Names of the regions used in Section 3.2.

3.2 Detailed results for particular galaxies

In the previous section, it is found for the whole sample galaxies that H_2O ice and CO_2 ice are detected in regions where the ISM is abundant and star formation is active, respectively. In this section, the relation between the abundances of the ices and the local interstellar environment is examined in more detail. Spatially-resolved NIR spectra with detection of ices are used, and the relation is discussed between the spatial distributions of the ices and those of other ISM components. Appropriate targets for this study are the nearby starburst galaxies NGC 253 and M 82. Since they are very close to us (NGC 253: 3.5 Mpc, Rekola et al. 2005; M 82: 3.5 Mpc, Karachentsev et al. 2002), it is easy to obtain spatially-resolved spectra of the ices. Moreover, thanks to good visibility of these galaxies for AKARI, multiple pointed observations were performed, which is important to discuss the spatial distributions of the ices in the galaxies. In addition, NGC 1097 (19.1 Mpc; Willick et al. 1997) is studied in detail to discuss the spatial distribution of the ices; the galaxy is characterized as a starburst galaxy with a low-luminosity AGN.

3.2.1 NGC 253

Spatial distributions of H_2O and CO_2 ices

NGC 253 is a well-studied starburst galaxy. The central peak in the NIR is thought to be a young superstar cluster (Keto et al. 1999; Kornei & McCrady 2009). The kinematic center of NGC 253, TH2, is a compact radio source at a wavelength of 2 cm, which is spatially separated from the peak of the NIR by 4″ (see Fig. 3.9). AKARI observed the north and south sides of the NIR peak. Details of the results for NGC 253 are published by Yamagishi et al. (2011).

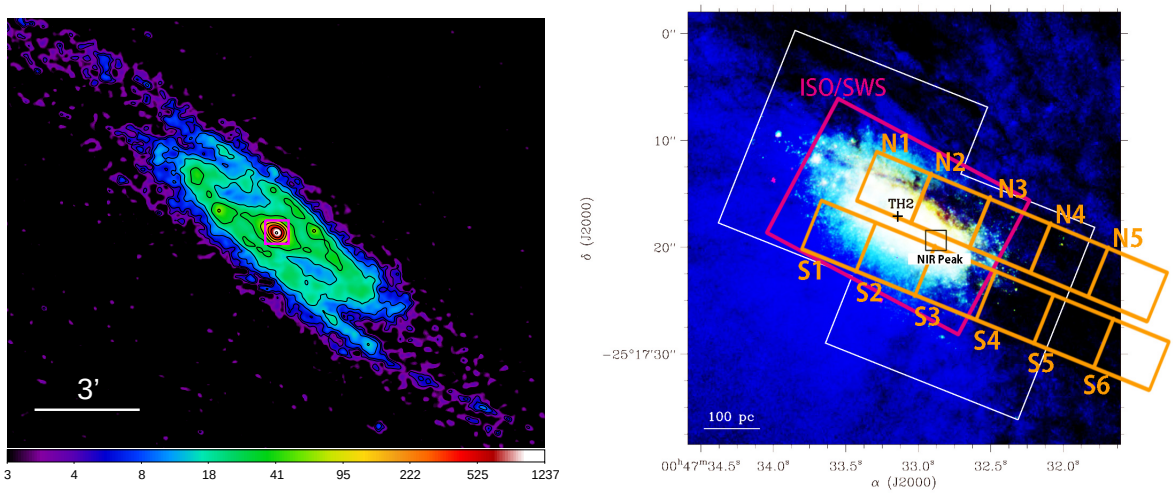

Figure 3.9 (left) AKARI 9 μm image of NGC 253. The contours are drawn at logarithmically-spaced 10 levels from 95% to 0.4% (5σ level) of the peak surface brightness (1237 MJy/str). The region shown in the right panel is represented with the magenta box. (right) Slit sub-aperture regions with their names, which are overlaid on the Hubble Space Telescope NIR three color image of NGC 253 taken from Kornei & McCrady (2009). The color scale of the image is changed from the original one to show low surface brightness area more clearly. Each sub-aperture (N1–5, S1–6) has a size of 5″ × 5.″8, from which the spectra are created. The magenta box indicates the slit aperture observed with ISO/SWS (Sturm et al. 2000).

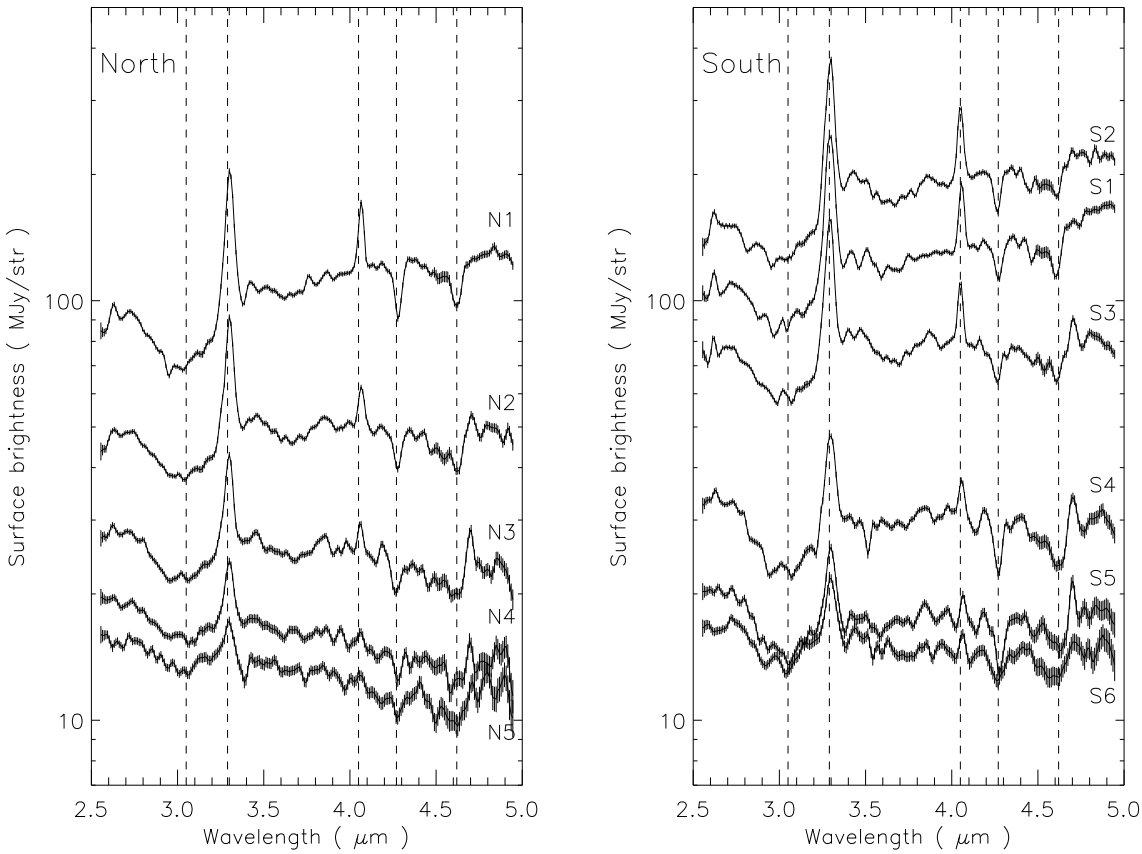

Figure 3.10 Spectra obtained for NGC 253 with the names of the regions indicated in Fig. 3.9 (right). The left and the right panels show the spectra observed in the north and the south regions, respectively. The dashed lines indicate the wavelengths of H_2O ice (3.05 μm), PAH 3.3 μm (3.29 μm), Brα (4.05 μm), CO_2 ice (4.27 μm), and XCN ice (4.62 μm).

Figure 3.9 shows the slit positions of the observations and the regions from which the spectra are created in NGC 253. The obtained NIR spectra are shown in Fig. 3.10. In the spectra, the absorption features due to H_2O and CO_2 ices are detected from all the spectra. Some spectra also show the absorption feature due to XCN ice at 4.62 μm. In addition, several strong features are detected in the spectra; the PAH 3.3 μm, Brα, and $H_2S(9)$. In the past study with ISO, Sturm et al. (2000) reported the detection of only H_2O ice in the galactic center of NGC 253. Hence this is the first detection of CO_2 and XCN ices in NGC 253. The derived optical depth of H_2O ice in the S2 region (Fig. 3.10, τ=0.25 $\pm$ 0.01) is consistent with that previously measured by ISO ($\tau \sim 0.25$; Sturm et al. 2000) within the error; the S1–S3 and N1–N3 regions overlap with the slit aperture of Sturm et al. (2000) (Fig. 3.9 (right)).

Figure 3.11 shows the column densities of H_2O and CO_2 ices, the integrated line intensities of PAH 3.3 μm and Brα, and the surface brightness at 3.05 μm and 4.27 μm, which are obtained by the spectral fitting (Section 2.4). The spectral maps of the features/lines are shown in Fig. 3.12. In the figures, the profiles and spatial distributions of H_2O and CO_2 ices are similar to each other, suggesting a good correlation between their column densities. In addition, the spatial distributions of the ices are different from those of the other features; the integrated line intensity and the surface brightness have peaks in the N1 and S2 regions and decrease rapidly to the N5 and S6 regions, while the column densities of the ices show much smaller changes from region to region. Furthermore, on the south side, the ices show peaks

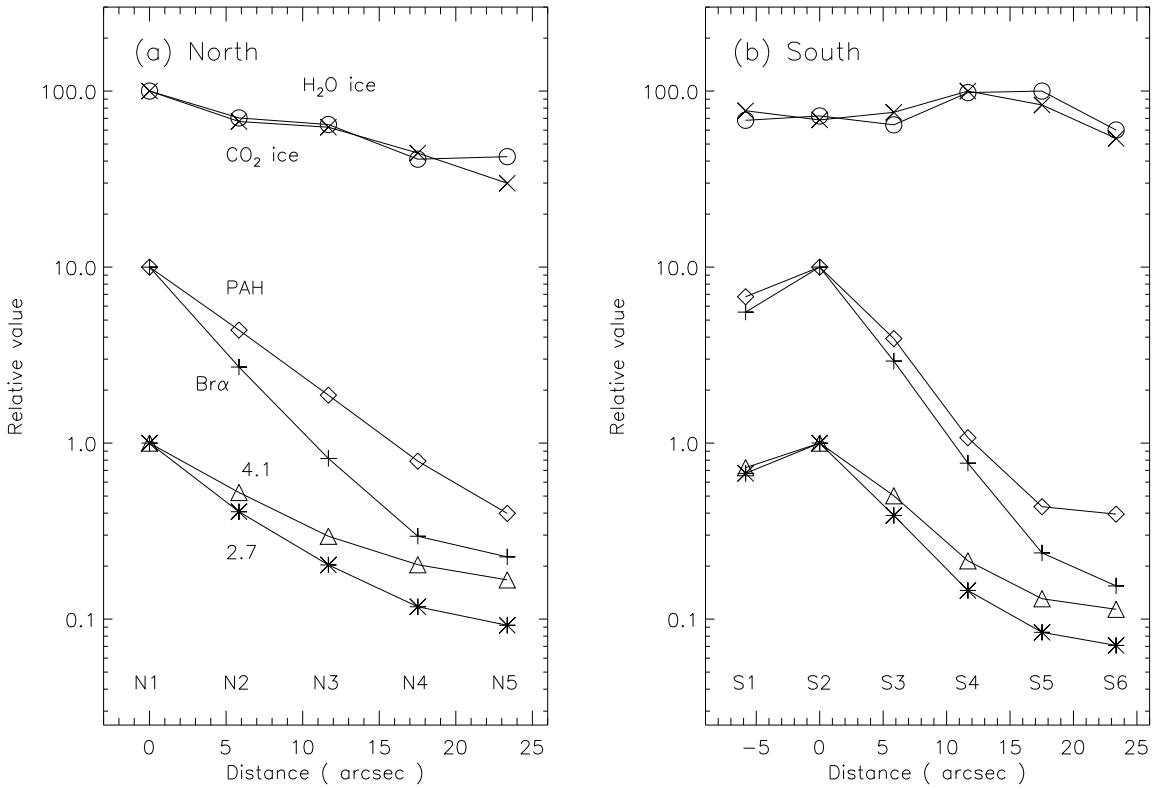

Figure 3.11 Changes of the ice column densities as well as the intensities of the PAH feature, Brα, and continuum emissions with the distance from N1 for the north region (left) and S2 for the south region (right). The cross, circle, diamond, plus, square, triangle, and asterisk symbols indicate the column densities of the H_2O ice (peak values of 6.2×10^{17} cm^{-2} for the north side and 6.3×10^{17} cm^{-2} for the south side) and CO_2 ice (7.9×10^{16} cm^{-2} and 8.1×10^{16} cm^{-2}), the integrated intensities of the PAH 3.3 μm (2.0×10^{-3} erg/s/cm^2/str and 4.2×10^{-3} erg/s/cm^2/str) and Brα (3.6×10^{-4} erg/s/cm^2/str and 7.3×10^{-4} erg/s/cm^2/str), and the surface brightness at 2.7 μm (92 MJy/str and 149 MJy/str) and 4.1 μm (121 MJy/str and 200 MJy/str), respectively. Each profile is normalized by its peak value. The column densities of the ices and the integrated intensities of the line and feature emissions are multiplied by 100 and 10, respectively for display purpose.

in the S4 and S5 regions which are located far from the NIR peak. Therefore, these profiles suggest that the spatial distributions of the ices are different from those of PDRs, HII regions, and the continuum emitters. The profiles also suggest that the absorbers responsible for the ice features are more widely distributed than the line and the continuum emitters.

Connections with the interstellar environment

The N1 and N2 spectra show weaker continuum emission than the S2 and S3 spectra probably due to the presence of a dust lane on the north side of the NIR peak (Fig. 3.9). In the S5 region, another prominent dust lane is visible, which presumably contributes significantly to the column densities of the ices. Figure 3.13 shows the ^{12}CO (J=1–0) map of NGC 253 obtained with the Nobeyama 45 m telescope (Kuno et al. 2007). The CO map reveals a centrally-concentrated distribution which presumably contribute to the large column densities of the ices in the galactic center. The map, however, does not have a local maximum around the S5 region, which may be caused by the difference in the spatial scale between the CO map ($\sim 15''$) and the AKARI/NIR spectroscopic slit sub-apertures ($\sim 5''$). Figure 3.14 shows the AKARI slit sub-apertures overlaid on the ^{12}CO(2–1), ^{12}CO(3–2), ^{13}CO(2–1), and ^{13}CO(2–

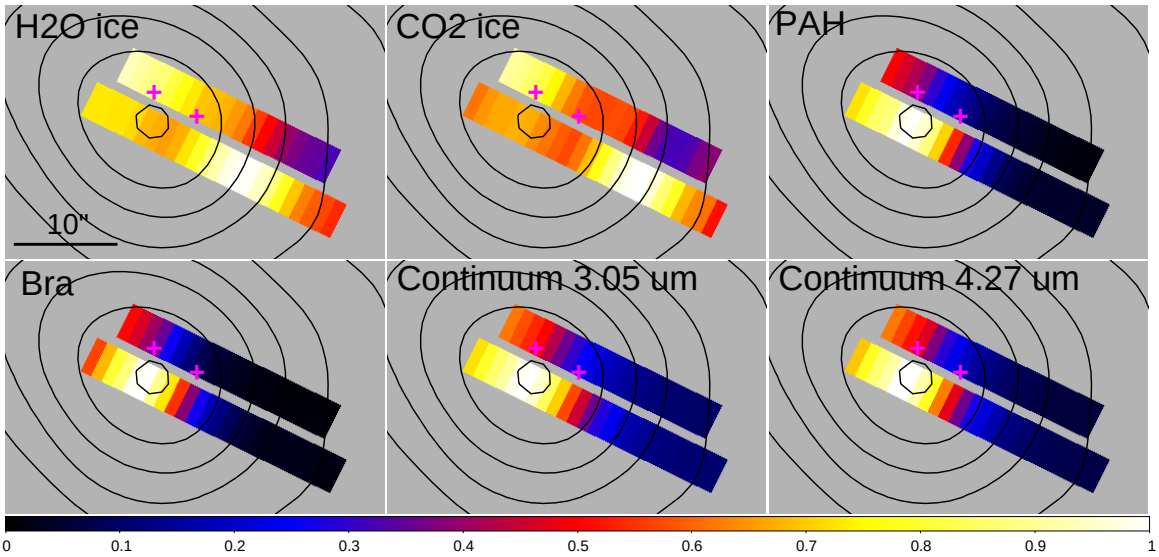

Figure 3.12 Spectral maps of the H_2O ice, CO_2 ice, PAH 3.3 μm, Brα, and the surface brightness at 3.05 μm and 4.27 μm, overlaid on the contour map of the AKARI 9 μm image (Fig. 3.9). Each map is normalized by its peak value. The peak values are 5.7×10^{17} cm^{-2} for the H_2O ice, 8.5×10^{16} cm^{-2} for the CO_2 ice, 3.9×10^{-3} erg/s/cm^2/str for the PAH 3.3 μm, 7.2×10^{-4} erg/s/cm^2/str for Brα, 148 MJy/str for the surface brightness at 3.05 μm, and 196 MJy/str for the surface brightness at 4.27 μm. The color scales are common among the maps. The two crosses represent the positions of the galactic center (TH2) and the NIR peak in Fig. 3.9.

1)/^{12}CO(2–1) maps of NGC 253 obtained with SMA (Sakamoto et al. 2011), the spatial resolution of which is $\sim 1''$. The ^{12}CO(2–1), ^{12}CO(3–2), and ^{13}CO(2–1) maps overall reveal centrally-concentrated distributions similarly to the map in Fig. 3.13. Furthermore, five prominent peaks are resolved in the galactic center due to the high spatial resolution, but these peaks do not correspond to the S5 region. In contrast to the former three maps, there is a prominent peak at the position of S5 in the ^{13}CO(2–1)/^{12}CO(2–1) isotopologue map, which suggests that there are molecular clouds with high densities and low temperature in the S5 region. Since the intensities in the ^{13}CO(2–1) and ^{12}CO(2–1) maps themselves are weak in the S5 region, the total amount of the gas in the S5 region seems to be much smaller than that of the galactic center. These results suggest that there are actually corresponding molecular clouds where the ices are detected, and that the molecular gas density is important to determine the abundances of ices rather than the total amount of gas.

Figure 3.15 shows the correlation plot between the column densities of H_2O and CO_2 ices, which shows an overall linear correlation as expected from Fig. 3.11. Therefore, this result suggests no systematic difference in the CO_2/H_2O ice abundance ratios in the galaxy. From the slope of the best-fit line to the data, the averaged CO_2/H_2O ice abundance ratio is 0.14 ± 0.01, which is consistent with the ratio obtained from the Galactic massive YSOs (0.17 ± 0.03, Gerakines et al., 1999; Gibb et al., 2004). Shimonishi et al. (2010) interpreted that the high CO_2/H_2O abundance ratio in the LMC (0.36 ± 0.09) is caused by a relative increase in CO_2 ice possibly due to either strong interstellar UV photon irradiation to H_2O-CO ice mixtures (e.g., Watanabe & Kouchi 2002) or relatively high dust temperatures (Bergin et al. 1999; Ruffle & Herbst 2001). In the center of NGC 253, nuclear starburst has occurred (Dudley & Wynn-Williams 1999), which indicates the existence of strong interstellar UV radiation field. The slopes of the NIR continuum spectra suggest the presence of hot dust. Therefore this result suggests that intense interstellar UV radiation field and high dust temperatures may not be important factors to determine

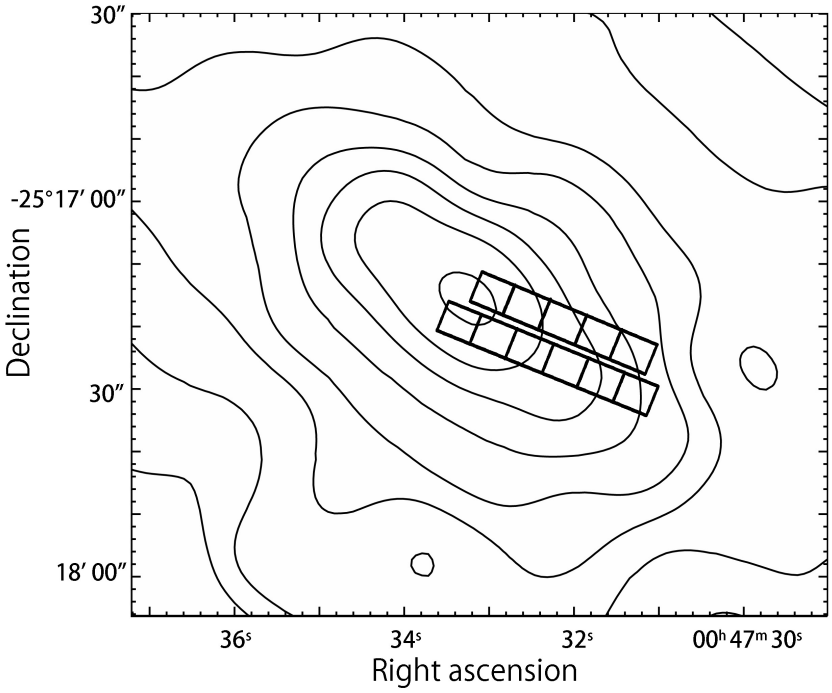

Figure 3.13 AKARI slit sub-apertures overlaid on the integrated ^{12}CO (J=1–0) map of NGC 253 (Kuno et al. 2007). The contours are drawn at logarithmically-spaced eight levels from 95 % to 5 % of the peak intensity (1.08×10^3 K km/s).

the ice abundance ratio. Metallicity in NGC 253 is known to be close to a solar value, $Z \sim 1Z_\odot$ (Webster & Smith 1983), while $Z \sim 0.3Z_\odot$ for the LMC (Luck et al. 1998). Therefore, the interstellar metallicity might be an important chemical condition to affect the CO_2/H_2O abundance ratio.

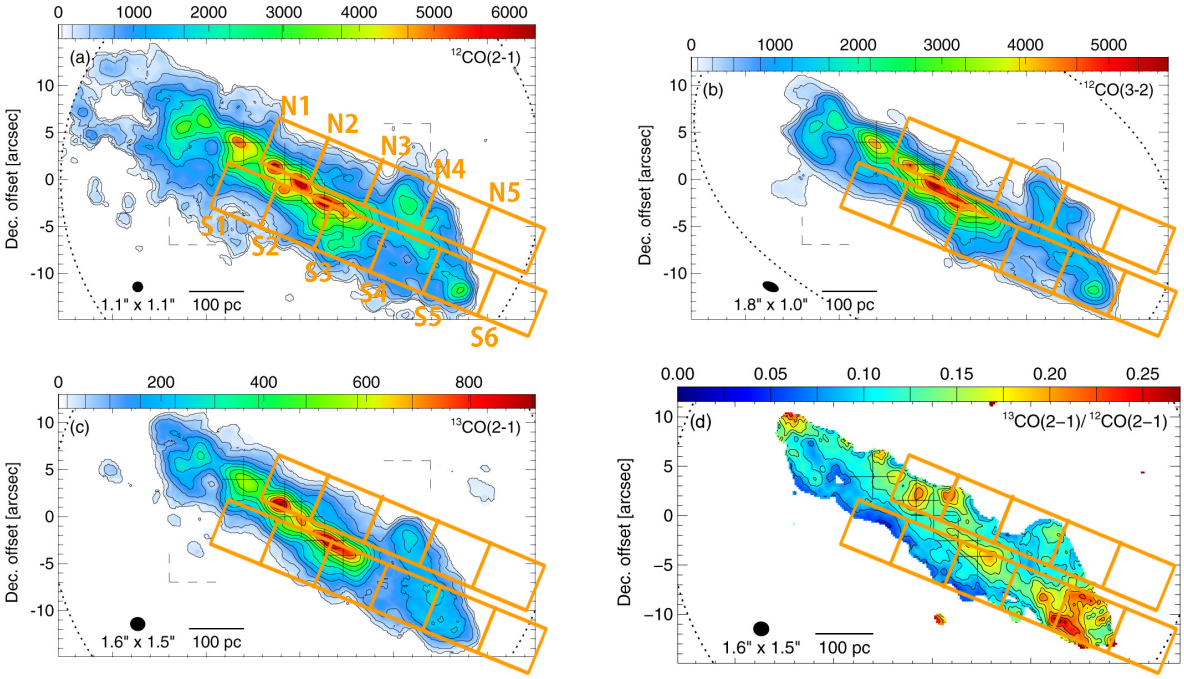

Figure 3.14 AKARI slit sub-apertures overlaid on the integrated intensity maps ^{12}CO(2–1), ^{12}CO(3–2), ^{13}CO(2–1), and the ^{13}CO(2–1)/^{12}CO(2–1) ratio map of NGC 253 obtained with SMA (Sakamoto et al. 2011). The color levels in the former three maps are given in units of K km/s. The beam size of each map is shown at the left bottom corner.

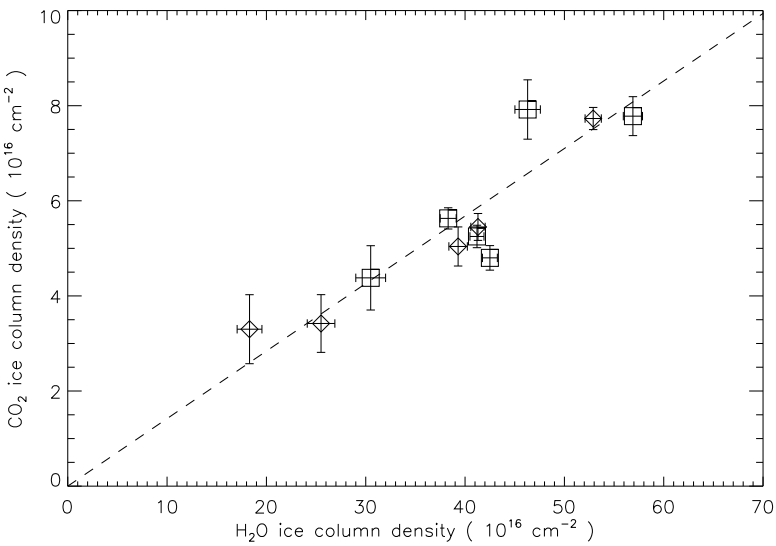

Figure 3.15 Column densities of the CO_2 ice plotted against those of the H_2O ice in NGC 253. The diamonds and squares represent the results from the north and south regions, respectively. The dashed line represents the best-fit linear relation between the CO_2 ice and H_2O ice column densities.

3.2.2 M 82

Spatial distributions of H_2O and CO_2 ices

M 82 is a nearby edge-on starburst galaxy, which shows prominent galactic superwind. The starburst activity in M 82 was presumably triggered by close encounter with M 81 about 100 Myrs ago (Yun et al. 1993). Figure 3.16 shows the observed slit positions around the galactic center of M 82. AKARI covered three regions of the galactic disk including the galactic center. Details of the results for M 82 are published by Yamagishi et al. (2012, 2013).

Figure 3.17 shows examples of the spectra extracted from the center of M 82, which reveal variations of the spectra in the direction from the galactic center to the south east. In the figure, H_2O ice is significantly detected in all the observed regions. The optical depth of H_2O ice in the galactic center ($\tau = 0.23 \pm 0.01$) is roughly consistent with that ($\tau \sim 0.2$) reported by Sturm et al. (2000). In contrast, CO_2 ice is not detected in regions distant from the galactic center, where H_2O ice is still clearly detected. In order to quantify the spatial distributions of the ices, their column density maps are created for the three observed regions which cover a ~1 kpc region of the galactic center.

Figures 3.18 (a) and (b) show the resultant column density maps of H_2O and CO_2 ices which indicate that the ices are abundant near the galactic center. The spatial distributions of the ices are clearly different from that of PAHs (Kaneda et al. 2010), which is similar to the situation in NGC 253 (Fig. 3.11). The spatial distribution of PAHs has a very sharp peak in the galactic center, and it is close to symmetry with respect to the galactic center and disk. Whereas the spatial distributions of the ices are biased

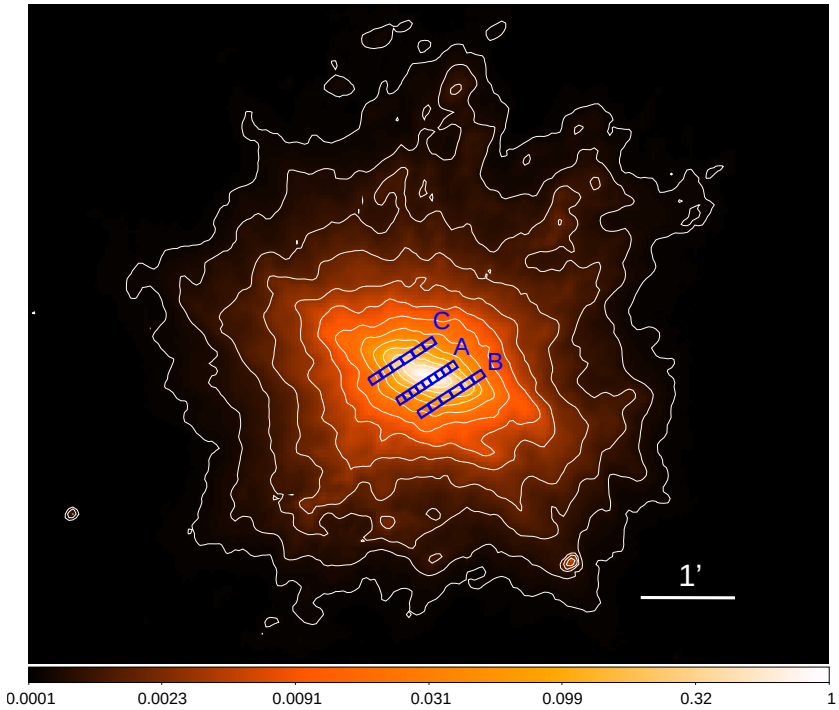

Figure 3.16 Slit sub-apertures in M 82 overlaid on the normalized AKARI 7 μm map (Kaneda et al. 2010). The names of the regions defined in Yamagishi et al. (2012) (A, B, and C) are indicated together, where the incremental order of the number is from the north to the south. The peak surface brightness at 7 μm is 5130 MJy/str.

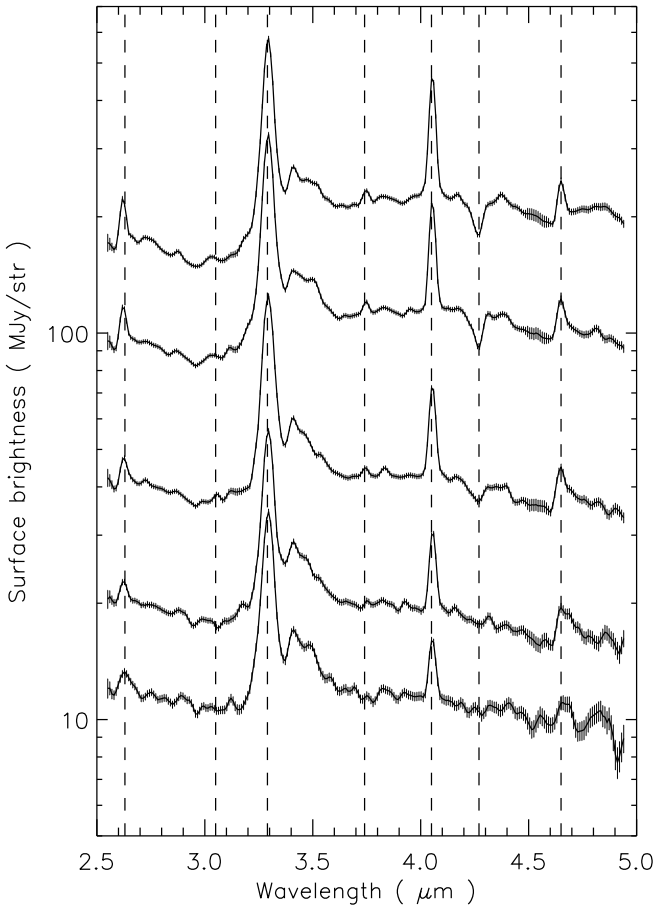

Figure 3.17 Variations of the NIR spectra in the center of M 82 (region A, defined in Fig. 3.16(a)). The spectra are obtained from the sub-apertures placed at an interval of 4.″4 along the slit from the galactic center (top) to the south-east direction (bottom). The dashed lines indicate the wavelengths of Brβ (2.63 μm), H_2O ice (3.05 μm), PAH 3.3 μm (3.29 μm), Pfγ (3.74 μm), Brα (4.05 μm), CO_2 ice (4.27 μm), and Pfβ (4.65 μm).

toward the northeast from the center. Such biased distributions of the ISM in the center of M 82 were also reported in the ^{12}CO (J=1–0) emission (Walter et al. 2002). A comparison of the spatial distribution of the total (H_2O+CO_2) ice with that of CO is shown in Fig. 3.18(c). The figure shows that the spatial distribution of the total ice is globally correlated with that of CO and the peak position of the ice corresponds to the bright ridge seen in the CO map. Thus, it is clear that the spatial distributions of the ices are similar to that of the CO emission rather than that of the PAH emission, reflecting that ices are mainly present in dense molecular clouds, but not in PDRs.

Connections with the interstellar environment

In Figs. 3.18(a) and 3.18(b), there is a clear difference in the spatial distribution of the ices; H_2O ice is significantly detected in all the observed regions, while CO_2 ice is detected only in smaller areas near the galactic center. These trends are consistent with the changes of the spectra seen in Fig. 3.17. In NGC 253 (Fig. 3.11), there is no clear difference in the spatial distribution between H_2O and CO_2 ices. Figures. 3.18(a) and 3.18(b) for the first time reveal variations in the CO_2/H_2O ice abundance ratio on a galactic scale, suggesting that the ice-forming interstellar environment changes within a galaxy.

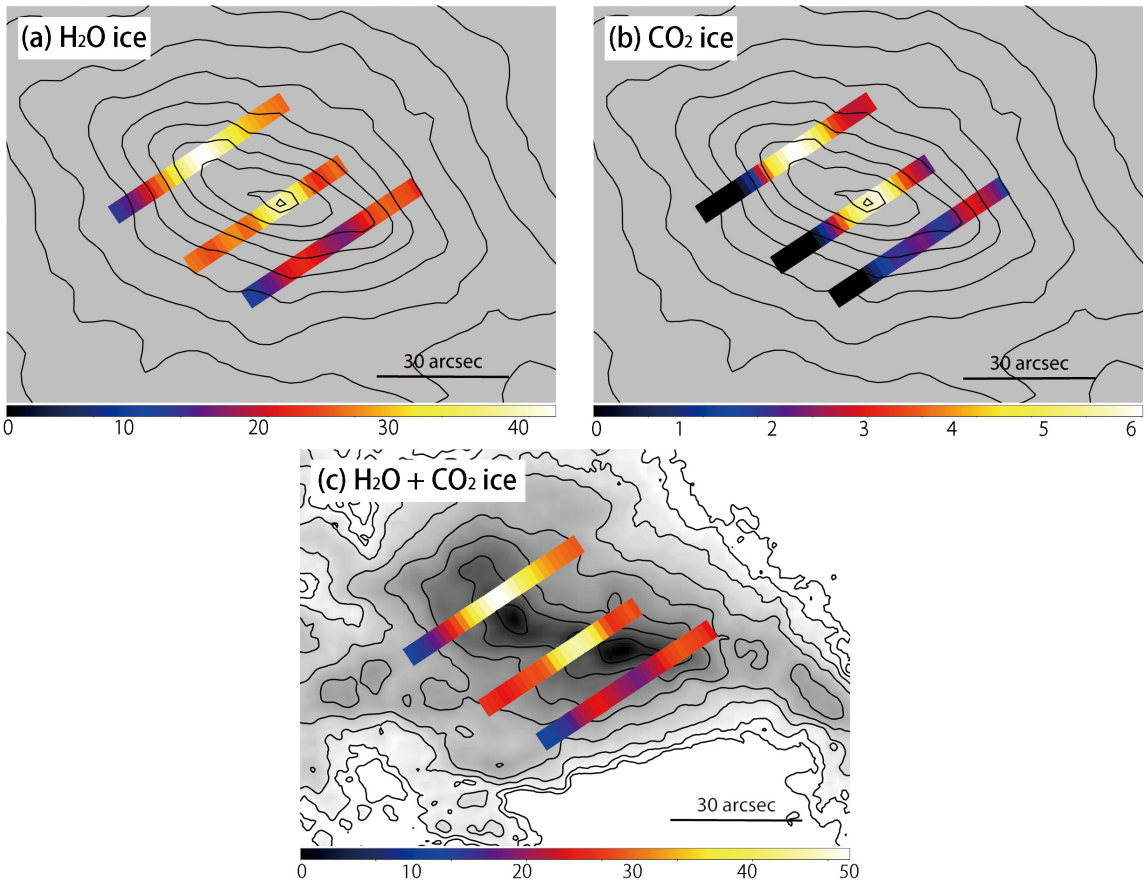

Figure 3.18 Maps of the column densities of (a) H_2O ice, (b) CO_2 ice, and (c) H_2O+CO_2 ice for M 82. The color levels are given in units of 10^{16} cm^{-2}. North is up and east is to the left. The contours in Figs. 3.18(a) and 3.18(b) are taken from the AKARI 7 μm image (Kaneda et al. 2010). The background image in Fig. 3.18(c) is the ^{12}CO (J=1-0) map from Walter et al. (2002).

Figures 3.19(a) and 3.19(b) show the column densities of the total ice plotted against the PAH 3.3 μm intensities and ^{12}CO (J=1–0) intensities, respectively. The former shows a rather loose correlation ($R = +0.52$, $N = 14$), while the latter shows a relatively tight correlation ($R = +0.72$, $N = 14$), as can also be expected from Fig. 3.18. Thus these figures, again, confirm the coexistence of the ices with molecular clouds. In Fig. 3.19(b), the solid line indicates the relation in our Galaxy (Eqs. 1.11 and 1.12), where $N_{\rm H} = 2 \times 10^{21}$ mag/cm^2 and $N({\rm H_2})/I({\rm CO}) = 1 \times 10^{20}$ cm^{-2}/(K km/s) are assumed. It is found that the CO intensities are much larger than those expected from the column densities of the ices, suggesting that there are many clouds where the ices are not detected. Furthermore, there are significant variations in the CO intensities along the horizontal axis, which possibly reflect regional variations in the fraction of clouds where ices are formed.

Figure 3.20 shows the CO_2/H_2O ice abundance ratios plotted against the PAH 3.3 μm intensities in M 82. In the figure, there is a tight correlation between them ($R = +0.80$, $N = 14$). As shown in Fig. 3.18, the spatial distribution of the PAHs has a sharp peak and monotonically decreases from the galactic center. Thus the result suggests that the spatial distribution of the ices is clearly different between H_2O and CO_2 ices, and the abundance of CO_2 ice relative to H_2O ice decreases significantly with the galactocentric distance. Here it is notable that CO_2/H_2O ratios are strongly correlated with the PAH intensities, whereas the total ice column densities are not (Fig. 3.19), indicating that CO_2 ice is more efficiently formed in the galactic center.

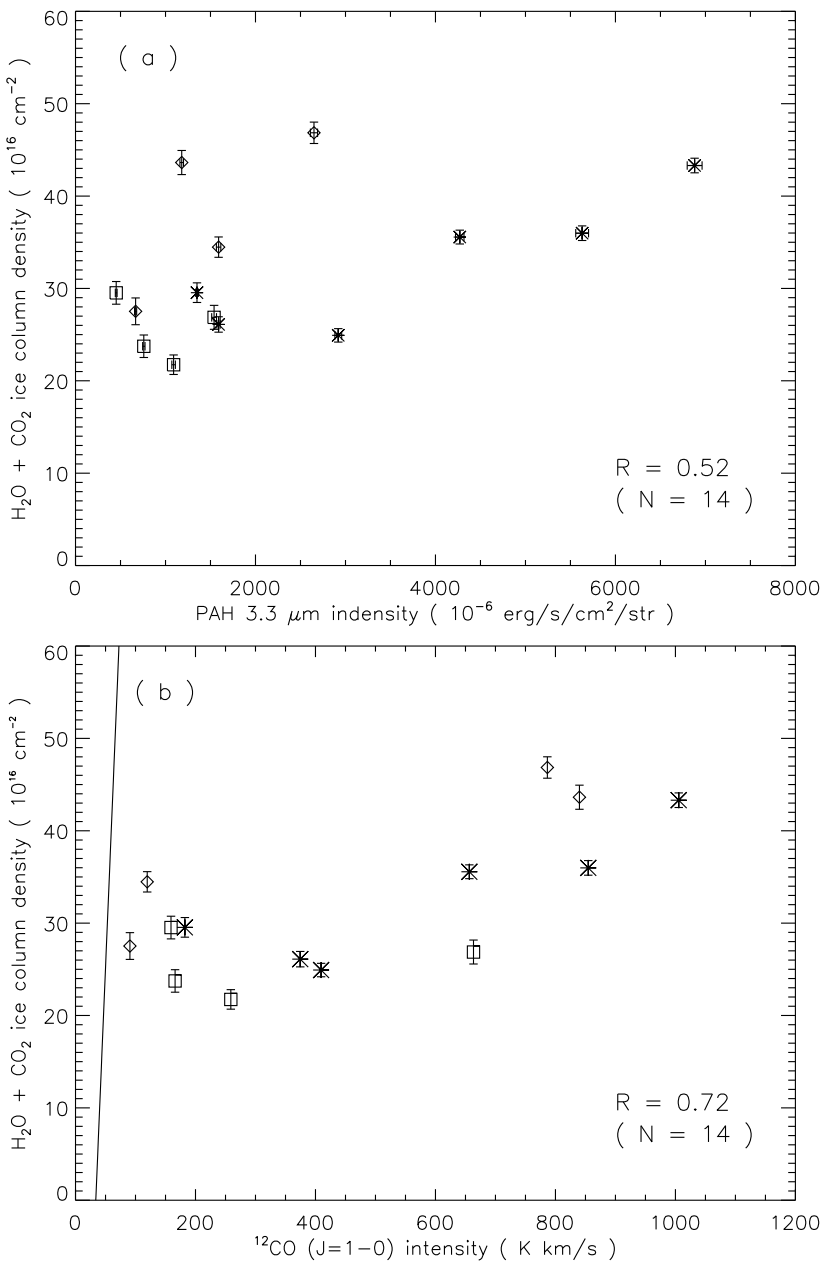

Figure 3.19 H_2O+CO_2 ice column densities plotted against (a) the PAH 3.3 μm feature intensities and (b) ^{12}CO (J=1–0) intensities. The asterisks, squares, and diamonds represent the data points in regions A, B, and C in Fig. 3.16, respectively. The correlation coefficient for each plot is shown at the bottom right. The solid line in Fig. 3.19 (b) indicates the relation in our Galaxy (Eqs. 1.11 and 1.12).

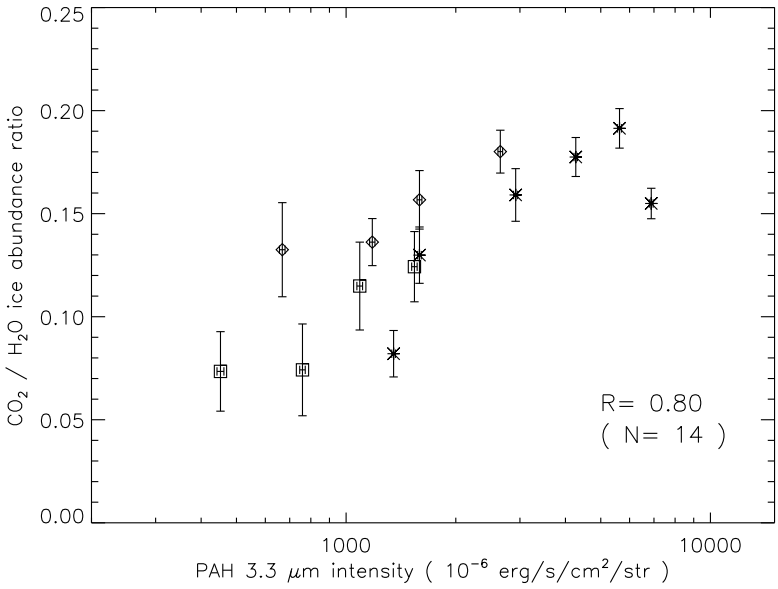

Figure 3.20 CO_2/H_2O ice abundance ratios plotted against the PAH 3.3 μm intensities in M 82. The correlation coefficient and the number of samples are shown at the bottom right. The definitions of the symbols are the same in Fig. 3.19.

3.2.3 NGC 1097

Spatial distributions of H_2O and CO_2 ices

NGC 1097 is a nearby barred spiral galaxy, which is categorized as Seyfert 1 with a starburst ring of ∼2 kpc in diameter and primary and second bars of ∼15 kpc and ∼1 kpc in length, respectively (Gerin et al. 1988; Shaw et al. 1993; Storchi-Bergmann et al. 1993; Kohno et al. 2003; Hsieh et al. 2008). Hence NGC 1097 is an ideal laboratory to study the ISM in galaxies showing both active galactic nucleus and circumnuclear starburst activities. AKARI observed two regions covering about a half of the ring and the galactic center. Details of the results for NGC 1097 are published by Kondo et al. (2012).

Figure 3.21 shows the slit positions of the two observations and the slit sub-aperture regions, from which the spectra in Fig. 3.22 are created. The second slit position (slit B) is shifted by $\sim 4''$ from the first slit (slit A), as shown in Fig. 3.21. In this section, the observed data in the slits A and B are used to show the spatial distributions of the ISM components in the starburst ring, although the latter one is not used in the statistical study. Most of the spectra in Fig. 3.22 show the absorption features due to H_2O ice (3.05 μm), SiO gas (4.3 μm), and CO (4.6 μm) gas. The spectra also show strong PAH emission with aliphatic features and Brα. The continuum brightness is highest in the A6 region, which is closest to the galactic center, monotonically decreasing with distance from the center. All the spectra have negative slopes against the wavelength, suggesting that cool stars of old populations make a significant contribution to the continuum emission.

Figure 3.23 shows the spatial variations in the fluxes of the spectral components along the slits, which are calculated not only for the spectra in Fig. 3.22 but also for those from other slit sub-apertures of the same size at intermediate positions. In order to better visualize the spatial distribution of each spectral component, the two-dimensional spectral maps are shown in Fig. 3.24, which are overlaid on the contour map of the Spitzer/IRAC 3.6 μm band. The spectral maps were created by regridding the discrete data

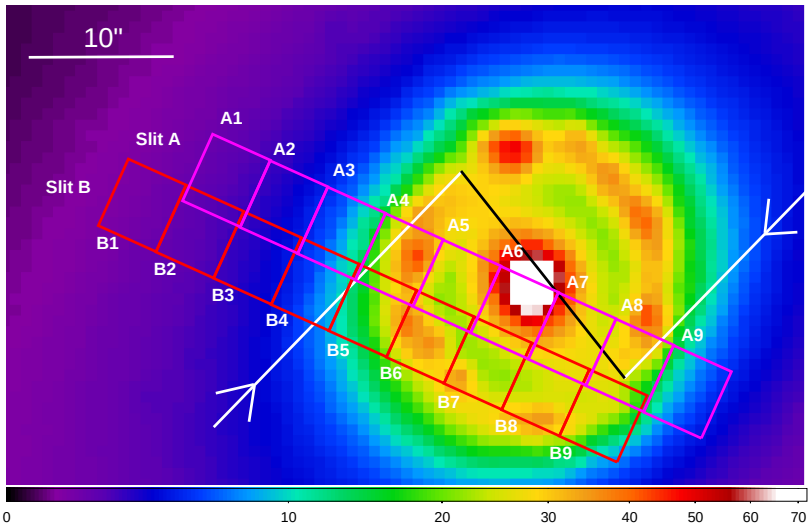

Figure 3.21 Positions of the slit sub-apertures used to create the spectra in Fig. 3.22, overlaid on the Spitzer/IRAC 3.6 μm image of the central region of NGC 1097. The color levels are given in units of MJy/str. Each slit sub-aperture (A1–A9, B1–B9) has a size of $5'' \times 4\farcs4$. The approximate locations of the primary and the second bar are indicated by the white and the black line, respectively (Quillen et al. 1995; Prieto et al. 2005). The arrows indicate the expected motion of the gas in the primary bar.

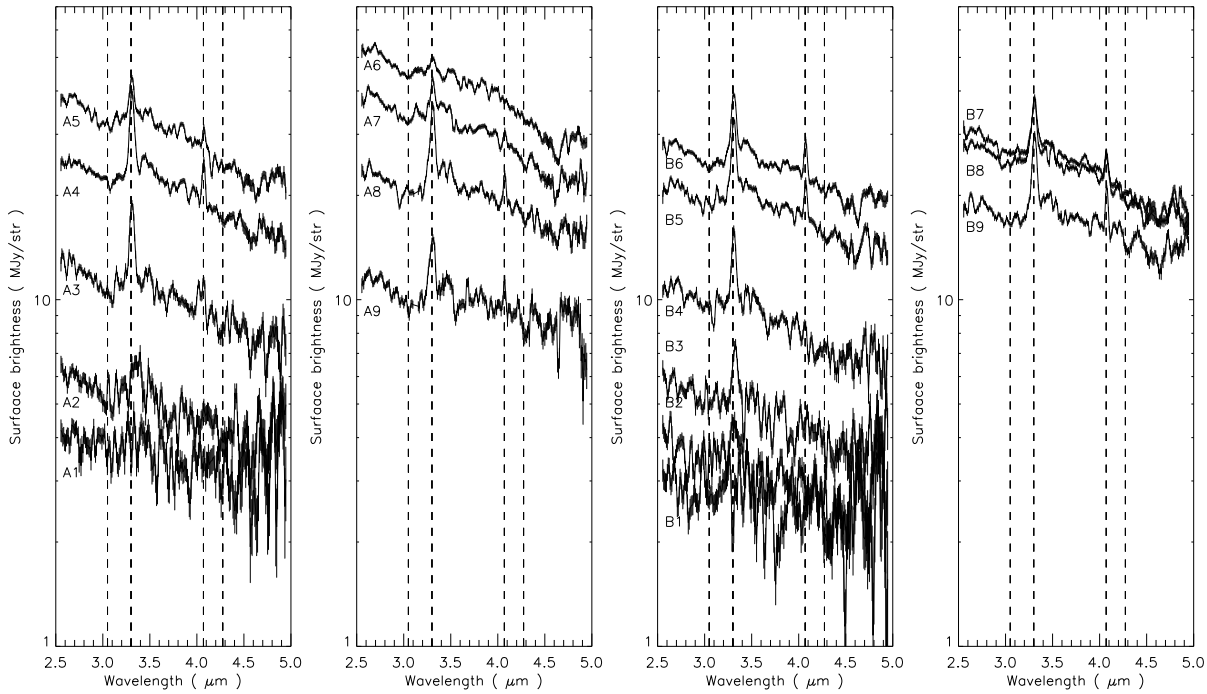

Figure 3.22 NIR spectra together with the names of the slit sub-apertures indicated in Fig. 3.21. The left two and the right two panels show the spectra observed in slits A and B, respectively. The dashed lines indicate the wavelengths of H_2O ice (3.05 μm), PAH 3.3 μm (3.29 μm), Brα (4.05 μm), and CO_2 ice (4.27 μm).

points in Fig. 3.23 to the spatial bin of $1''.7 \times 1''.7$ on the equatorial coordinate plane. As can be seen in Figs. 3.23 and 3.24, the spatial distributions are different from component to component. The PAH and Brα exhibit double-peaked structures, which appear to be associated with the starburst ring (Fig. 3.21). The continuum intensities at 3.05 μm are broadly distributed with a peak toward the galactic center, while H_2O and CO_2 absorption features are not apparently associated with either ring or center.

Connections with the interstellar environment

In NGC 1097, the spatial distributions of H_2O and CO_2 ices are entirely different from those of the other components, suggesting that ices are not associated with PDRs, HII regions, and stars. Figure 3.25 shows the AKARI slit sub-apertures overlaid on the ^{12}CO(2–1) integrated intensity map (Hsieh et al. 2011). The spectral maps of the ices show local maxima at positions similar to the peak in the CO (J =2–1) emission, which is, again, reasonable because ices are likely to be formed in dense gas regions. In particular, the enhancement is located at the CO clump near the contact point of the primary bar with the ring, where the CO gas has relatively low excitation temperatures but high velocity dispersion (Hsieh et al. 2011). The result suggests that an ice formation mechanism may work efficiently in such a condition.

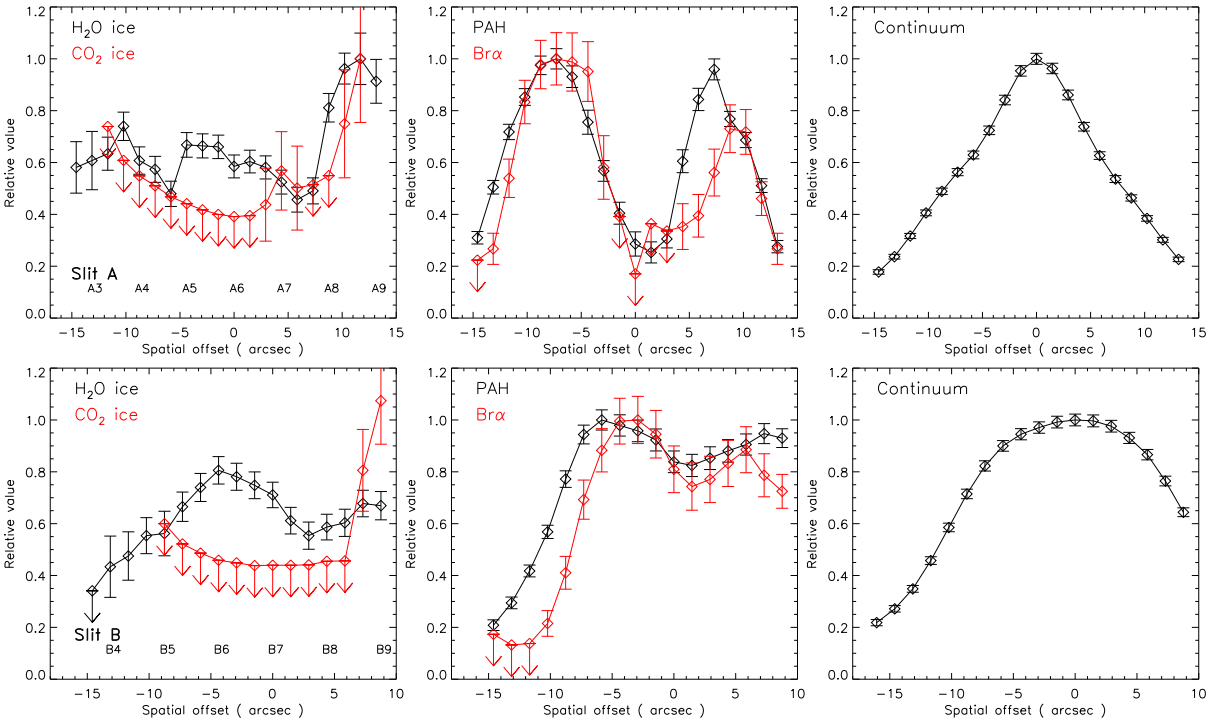

Figure 3.23 Changes of the spectral components with the offsets from A6 to A1–A9 (top) and from B7 to B1–B9 (bottom). (left panels) H_2O ice (peak: 26×10^{16} cm^{-2}) and CO_2 ice (4.2×10^{16} cm^{-2}). (center panels) PAH 3.3 μm feature (3.2×10^{-4} erg/s/cm^2/str) and Brα (4.4×10^{-5} erg/s/cm^2/str). (right panels) continuum brightness at 3.05 μm (48 MJy/str). Each profile is normalized to unity at the peak.

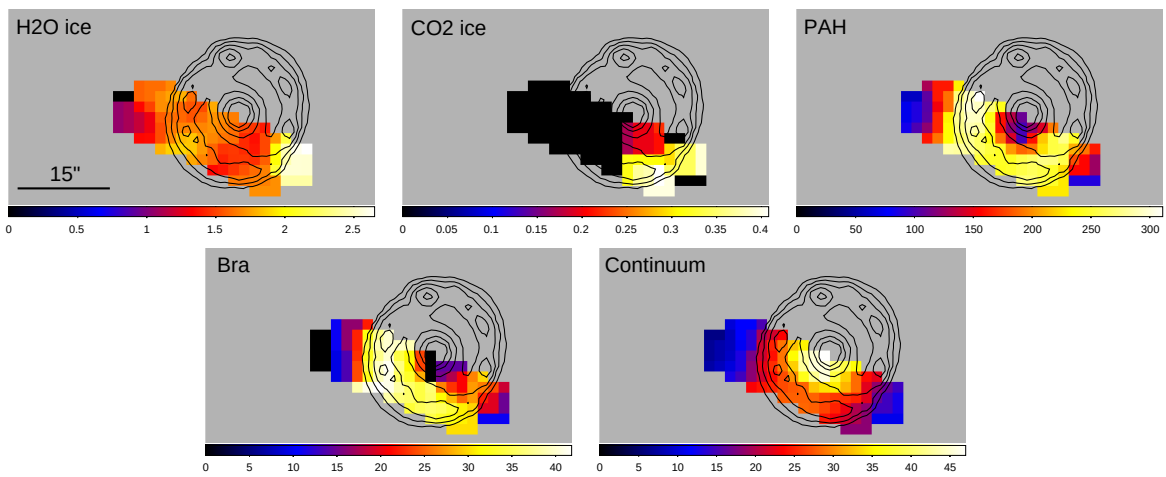

Figure 3.24 Spectral maps of the H_2O and CO_2 ice absorption features (unit; 10^{17} cm^{-2}), PAH 3.3 μm feature (10^{-6} erg/s/cm^2/str), Brα (10^{-6} erg/s/cm^2/str), and the continuum brightness at 3.05 μm (MJy/str), overlaid on the contour map of the Spitzer/IRAC 3.6 μm band (Fig. 3.21). The contours are drawn at logarithmically spaced six levels from 50 % to 15 % of the peak. A linear color scale from zero to the maximum is adopted for each map.

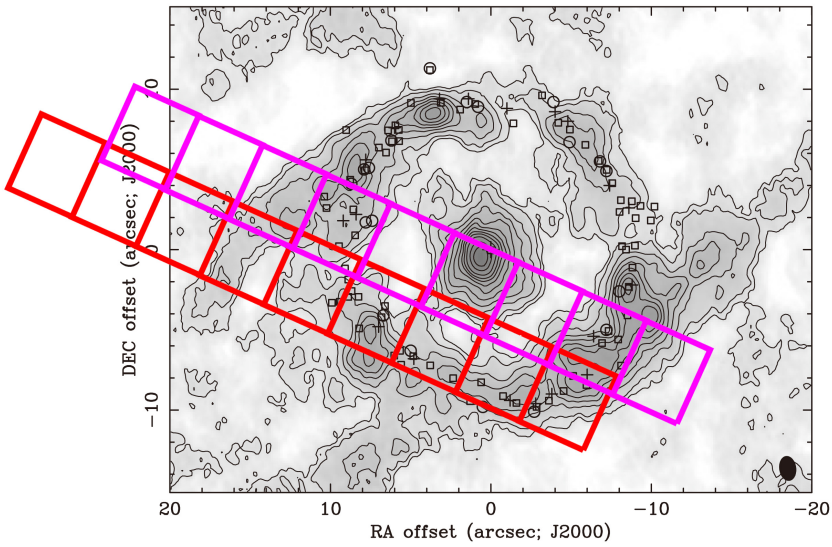

Figure 3.25 AKARI slit sub-apertures overlaid on the ^{12}CO(2–1) integrated intensity map (Hsieh et al. 2011). The contour levels are 2σ, 3σ, 5σ, $\cdots$, 20σ, 25σ, and 30σ, where 1σ=2.3 Jy km/s/beam. The beam size ($1\farcs5 \times 1\farcs0$) is shown in the bottom right. The positions of star clusters probed by Paα, 6 cm radio continuum, and V band are plotted in squares, crosses, and circles, respectively.

Chapter 4

Discussion

4.1 Application of ices as probes of the interstellar environment

In this section, relations between the abundances of ices and various parameters related to the interstellar environment are statistically examined, and the applicability of ices is investigated as probes of the interstellar environment.

4.1.1 Trends of the galaxies with detection of ices

The contents in this section are omitted because they have not been published in a refereed paper.

4.1.2 Column densities of ices as a dense ISM tracer

The contents in this section are omitted because they have not been published in a refereed paper.

4.1.3 CO_2/H_2O ice abundance ratios and the galaxy evolution

In this section, applicability of CO_2/H_2O ice abundance ratios is examined as a probe of the ice-forming interstellar environment. Figure 4.1 shows the CO_2/H_2O ice abundance ratios plotted against the column densities of H_2O ice. As already shown in Section 3.1, the data points are distributed around the CO_2/H_2O ice abundance ratio of 0.14. However, there is a large scatter between 0.05 and 0.3. Which physical parameters determine the CO_2/H_2O ice abundance ratio in each region?

The contents here are omitted because they have not been published in a refereed paper.

In M 82, the spatial distributions of H_2O and CO_2 ices are different from each other (Section 3.2.2, Fig. 3.18). To understand the cause of the large variation in the CO_2/H_2O ice abundance ratios, enhancement of the CO_2/H_2O ice abundance ratio in the galactic center of M 82 is investigated in detail. Considering that the CO_2 ice is formed around active star-forming regions (Section 3.1, Fig. 3.6), the UV radiation environment is likely to important for the CO_2 ice formation. Additionally, CO_2/H_2O ice abundance ratios decrease with the galactocentric distance (Section 3.2.2, Fig. 3.20), suggesting that the ratios may be related to the activity of the galactic center. The galactic center of M 82 is indeed characterized by intense starburst (Westmoquette et al. 2007; Keto et al. 1999). Therefore, the CO_2/H_2O ice

abundance ratio is examined in terms of the hardness of the UV radiation field. Figure 4.2 shows the CO_2/H_2O ice abundance ratios plotted against the PAH 3.3 μm/Brα flux ratios. Since the minimum photon energy to ionize hydrogen ($>$ 13.6 eV) is higher than that to excite PAHs ($<$ 13.6 eV), hardness of the UV radiation field is likely to be reflected to the PAH 3.3 μm/Brα ratios. In the figure, there is a negative correlation between the CO_2/H_2O ice abundance ratios and the PAH 3.3 μm/Brα ratios ($R = -0.73$, $N = 14$). Hardness of the UV radiation field depends on massive star-formation activity, which can be enhanced by the intense starburst in the galactic center. Hence the result implies that massive stars are important to enhance the CO_2/H_2O ice abundance ratios.

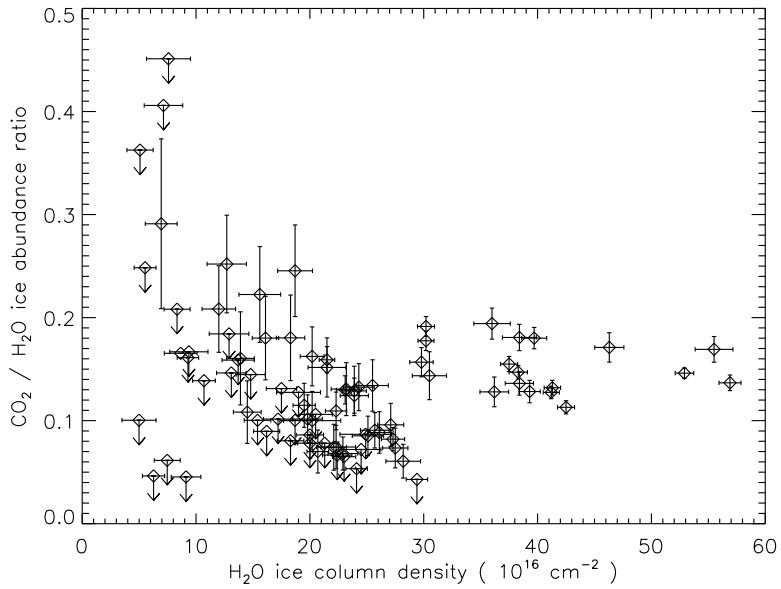

Figure 4.1 CO_2/H_2O ice abundance ratios plotted against the column densities of H_2O ice.

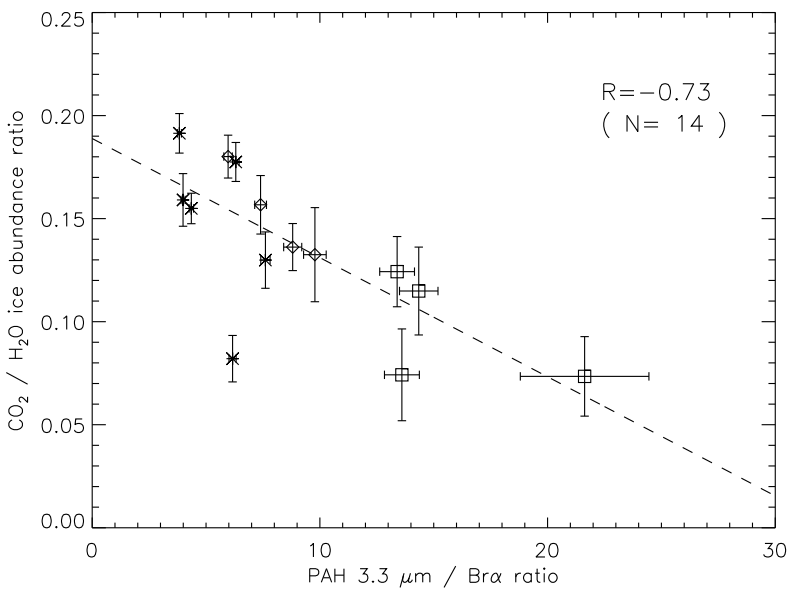

Figure 4.2 CO_2/H_2O ice abundance ratios plotted against the PAH 3.3 μm/Brα ratios in M 82. The correlation coefficient and the number of samples are shown at the top right. The definitions of the symbols are the same as in Fig. 3.19. The dashed line indicates the best-fit linear relation.

As to the formation process of CO_2 ice, energetic processes are favorable rather than non-energetic ones, because the CO_2 ice formation seems to be enhanced by the intense radiation environment from massive stars (Figs. 3.6 and 4.2). However it should be noted that interstellar UV photons cannot penetrate into molecular clouds, where ices are formed. Even in such a situation, however, UV photons can be induced by cosmic-rays penetrating deep inside clouds through their interactions with molecular hydrogen (Prasad & Tarafdar 1983). Importance of cosmic-ray induced UV photons to the ice chemistry has been pointed out in past studies for our Galaxy (e.g., Whittet et al. 1998). Shen et al. (2004) estimated that the cosmic-ray induced UV intensity exceeds the interstellar UV intensity attenuated by the extinction in dense regions with A_V >5 mag and >7 mag for the environments of $G_0 = 1$ and 10^2, respectively, where G_0 is a FUV (6–13.6 eV) intensity relative to that in the solar neighborhood. The typical dust temperature for the galaxies where the ices are detected is ∼30 K (Figs. **??** and **??**) which corresponds to $G_0 \sim 10^2$ (Tielens 2005). Additionally, CO_2 ice is expected to be formed in dense molecular clouds with a typical extinction of $A_V > 10$ mag (Section 4.1.2). Therefore, cosmic-ray induced UV photons probably act on the CO_2 ice formation more importantly than interstellar UV photons. Although the acceleration process of cosmic-rays has not yet been fully understood, it is likely that many supernova remnants due to the starburst activities increase the cosmic-ray energy density in the galactic center. In our Galaxy, significant increases in cosmic-ray ionization rate by a factor of 5–100 are reported for molecular clouds near the Galactic center and some supernova remnants (Goto et al. 2008; Indriolo et al. 2010; Geballe & Oka 2010; Ceccarelli et al. 2011), which support the CO_2 ice formation using cosmic-ray induced UV photons.

In our Galaxy, a typical cosmic-ray ionization rate and cosmic-ray-induced UV flux in a molecular cloud are 3×10^{-17} s^{-1} (Webber 1998) and 1×10^4 photons/s/cm^2 (Shen et al. 2004), respectively. Watanabe et al. (2007) experimentally examined the CO_2 ice formation via UV irradiation. They showed that the resultant abundances of CO_2, HCOOH, H_2CO, and CH_3OH ices relative to CO ice after irradiation of 6.5×10^{17} photons/cm^2 reproduce those observed in the Galactic diffuse ISM and YSOs. Considering the typical cosmic-ray-induced UV flux, the result indicates that CO_2 ice can be produced in 2×10^6 yr which is less than the typical life time of a molecular cloud (< a few $\times 10^7$ yr; Blitz & Shu 1980). Hence, their result clearly demonstrates the importance of cosmic-ray-induced UV photons in the formation process of CO_2 ice. Although the cosmic-ray ionization rate in nearby galaxies is unclear, if supernova rates are higher than a typical value in our Galaxy (0.02 yr^{-1}; Abdo et al. 2010), CO_2 ice should be formed more easily.

The contents here are omitted because they have not been published in a refereed paper.

4.2 Origins and geometry of ices in galaxies

In the previous section, it is assumed that the ices are of interstellar origin, and that all of them are located in the foreground of continuum emitters. This section discusses the origin of the ices (i.e. circumstellar or interstellar) and their geometry in a galaxy, by comparing Galactic and extragalactic cases.

4.2.1 Origins of the ices

The contents in this section are omitted because they have not been published in a refereed paper.

4.2.2 Geometry

The contents in this section are omitted because they have not been published in a refereed paper.

Chapter 5

Summary

Ices have many pieces of information on the interstellar environment. In our Galaxy, ices have been used as a useful probe of the interstellar environment in studies of YSOs and the diffuse ISM. However, in the past studies for nearby galaxies, ice features have not been fully utilized as probes of the interstellar environment. In particular, multiple ice features were not substantially discussed together due to the limit of the wavelength coverage and sensitivity of the instruments. Moreover, spatial information on ices in a galaxy is still unclear, because the spatial resolutions of the instruments are not high enough to resolve nearby galaxies. Hence, the goal of this thesis is to establish interstellar ices as probes of the interstellar environment in nearby galaxies by using both statistical and spatial information on the ices.

In order to achieve this goal, the spectra for 1031 regions in 158 nearby galaxies obtained with the AKARI NIR (2.5–5.0 μm) slit spectroscopy are systematically analyzed, which include absorption features due to H_2O and CO_2 ices at wavelengths of 3.05 and 4.27 μm, respectively. The NIR spectra also show prominent spectral features due to the PAH 3.3 μm and the hydrogen recombination lines (Brα and Brβ), which are helpful probes to investigate the ice-forming interstellar environment. This is the most extensive NIR spectroscopic survey of nearby galaxies. The advantages of the AKARI slit spectroscopy are high sensitivity and high spatial resolution in the NIR. A spectral fitting model, which consists of laboratory ice absorption profiles, Gaussian/Lorentzian emission lines, and multi-temperature blackbody continuum, is created to derive the column densities of the ices as well as the emission intensities.

As a result, H_2O ice is significantly detected from 125 regions in 30 galaxies, while CO_2 ice is detected from 54 regions in 12 galaxies. This search for the first time provides us with the sample of galaxies with detection of CO_2 ice and the most sensitive sample of galaxies with detection of H_2O ice. Comparing the column densities of the ices with the PAH 3.3 μm and Brα intensities, it is found that H_2O and CO_2 ices are detected in regions where PAHs are abundant and Brα is bright, respectively. This result suggests that H_2O ice and CO_2 ice are present in regions where the ISM is abundant and star formation is active, respectively. The averaged CO_2/H_2O ice abundance ratios for the sample galaxies is 0.14 ± 0.01, which is similar to the Galactic values reported in the past studies (Gerakines et al. 1999; Gibb et al. 2004).

In addition to the statistical study, the ices in NGC 253, M 82, and NGC 1097 are analyzed in detail, and the relation is investigated between the spatial distributions of the ices and those of other ISM components. In the galaxies, the spatial distributions of the ices are similar to that of the CO emission rather than that of the PAH emission, reflecting that ices are mainly present in dense molecular clouds, but not in PDRs. Most importantly, it is found that the spatial distributions of the ices are systematically different between H_2O and CO_2 ices in a galaxy. The difference is clearer in M 82; H_2O ice is widely

distributed in the galaxy, while CO_2 ice is concentrated near the galactic center, suggesting that the ice-forming interstellar environment changes in a galaxy.

Based on the statistical and spatially-resolved studies, the properties of the ices are discussed in terms of the interstellar environment. First, correlation between the column densities of the ices and the NIR $J-K_s$ colors is confirmed, which demonstrates that the column densities of the ices indeed increase with the amount of the ISM in a line of sight. The correlation also shows that CO_2 ice is present in denser regions than H_2O ice. Next, it is revealed that there is a negative correlation between the CO_2/H_2O ice abundance ratios and the PAH 3.3 μm/Brα ratios, which indicates that the hard UV radiation due to massive stars are important to enhance the CO_2/H_2O ice abundance ratios. The UV photons from massive stars, however, cannot penetrate into dense molecular clouds, where ices are formed. Therefore, the present study proposes that supernova remnants due to the massive star formation activities increase the cosmic-ray energy density, and cosmic-ray induced UV photons contribute to the CO_2 ice formation inside clouds, which are generated through interactions between cosmic-rays and molecular hydrogen. Additionally, it is found that the CO_2/H_2O ice abundance ratios are systematically different between relatively active galaxies and passive galaxies, and that there is a strong positive correlation between the CO_2/H_2O ice abundance ratios and the specific star formation rates of the galaxies. This result suggests that the evolutionary stage of a galaxy is also an important factor to determine the CO_2/H_2O ice abundance ratio of a galaxy. Thus it is concluded that the CO_2/H_2O ice abundance ratio depends on not only the hardness of the UV radiation field but also the evolutionary stage of a galaxy.

Finally, the origin of the ices in the nearby galaxies (i.e., circumstellar or interstellar) is discussed, by comparing the observed spectra with those for YSOs in our Galaxy in terms of the ice column densities, ice abundance ratios, continuum shapes, and absorption profiles. In terms of the CO_2/H_2O ice abundance ratios, high-mass YSOs would likely contribute to the ice absorption features observed for the nearby galaxies, because the CO_2/H_2O ice abundance ratio averaged for the nearby galaxies is close to that for high-mass YSOs. However, circumstellar ices in high-mass YSOs cannot reproduce the dependence of the CO_2/H_2O ice abundance on the hardness of radiation field, the ice column densities, and continuum shapes observed for the nearby galaxies. Furthermore, the profiles of the absorption features show that they are not saturated as expected for the spectra of YSOs. Hence all the observational results support the interstellar origin for the ices detected in the nearby galaxies.

This study has for the first time systematically discussed the properties of interstellar ices in the nearby galaxies, and investigated the relations between the abundances of the ices and the interstellar environment. Hence the past studies of ices for Galactic sources are successfully expanded into those for extra-galactic sources. This study indicates that spatial information is critical to discuss the relation between the abundance of the ices and the interstellar environment. Therefore, in future observations, spectral mapping observations are crucial to explore the spatial variation of the ice-forming interstellar environment within a galaxy in detail by using large telescopes in the NIR and MIR such as SPICA, JWST, and TMT.

Appendix

Appendix A Summary of the spectra with detection of ices

All the spectra where ices are detected are shown in Fig. A.1.

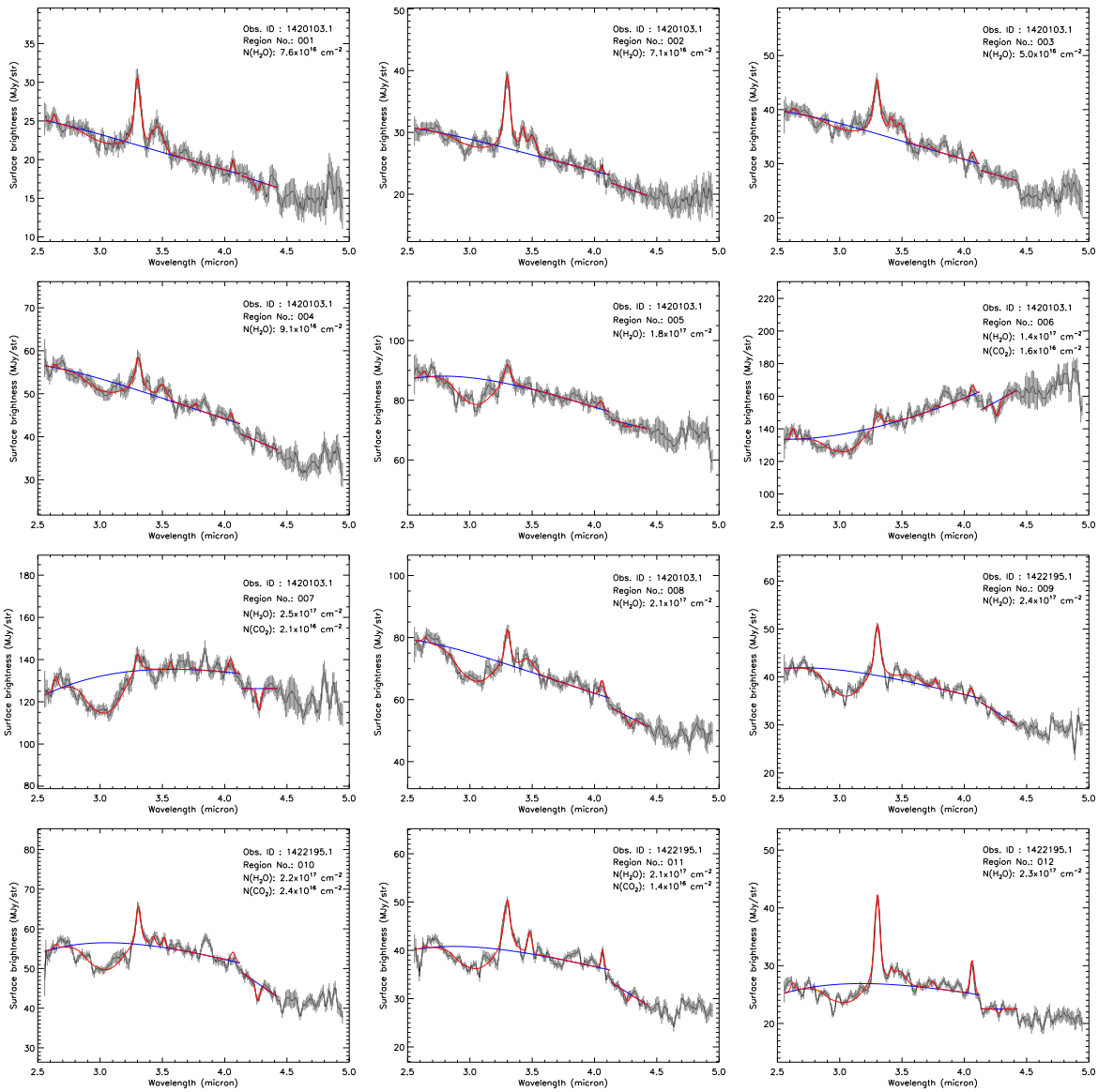

Figure A.1 All the spectra where ices are detected. The blue and red curves represent the best-fit continuum emission and overall profiles, respectively. The region numbers correspond to the numbers listed in the first column of Table 3.1.

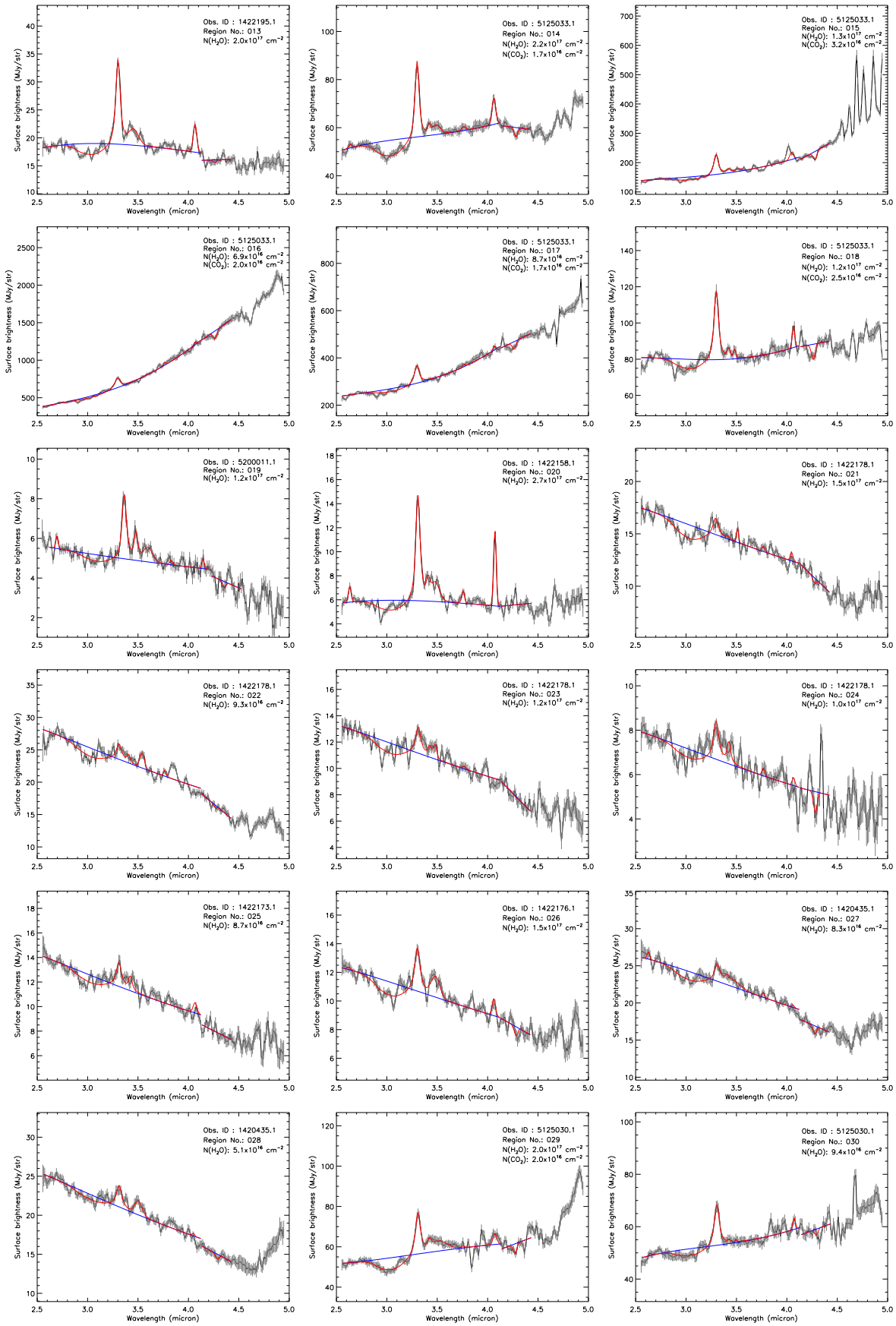

Figure A.1 Continued

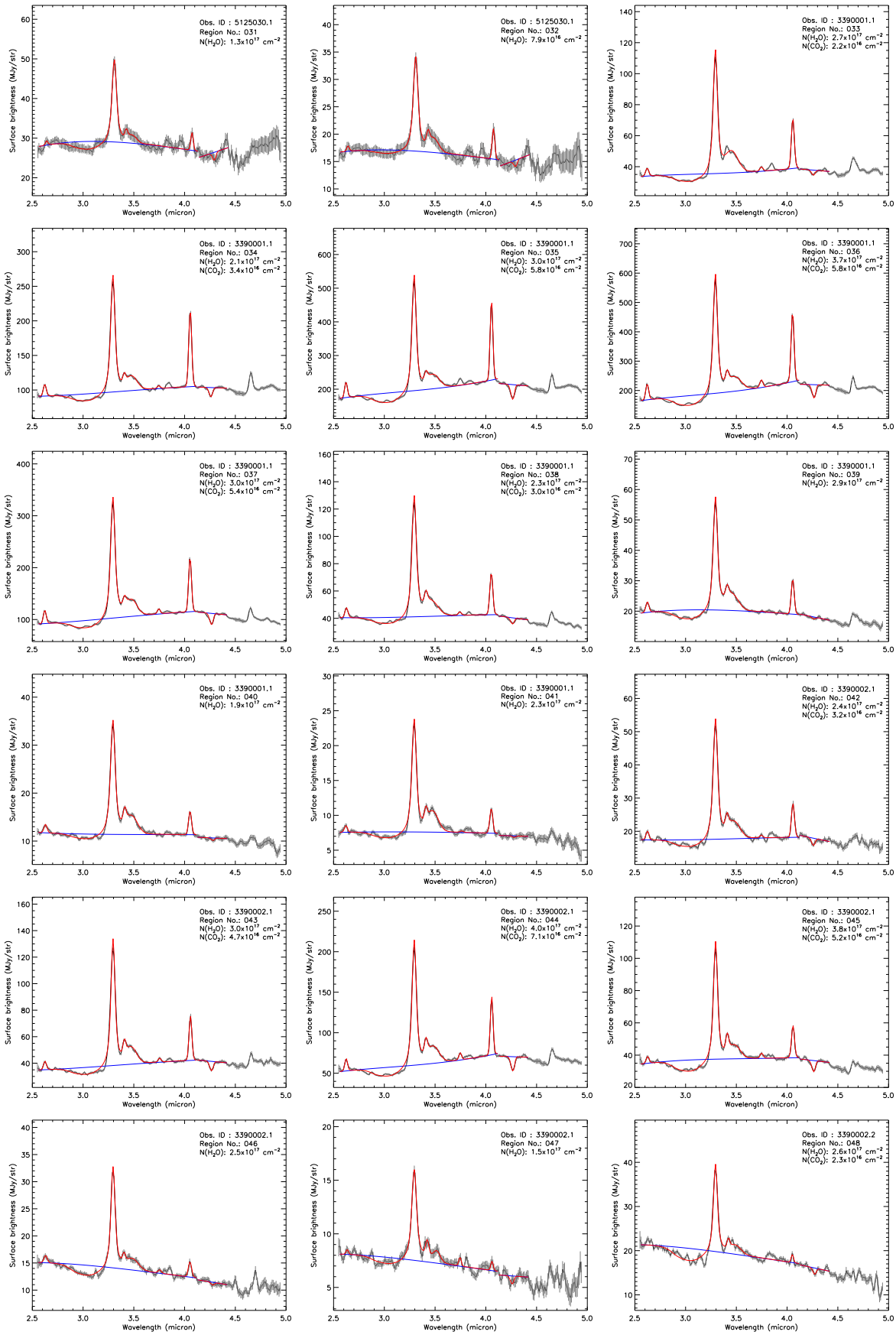

Figure A.1 Continued

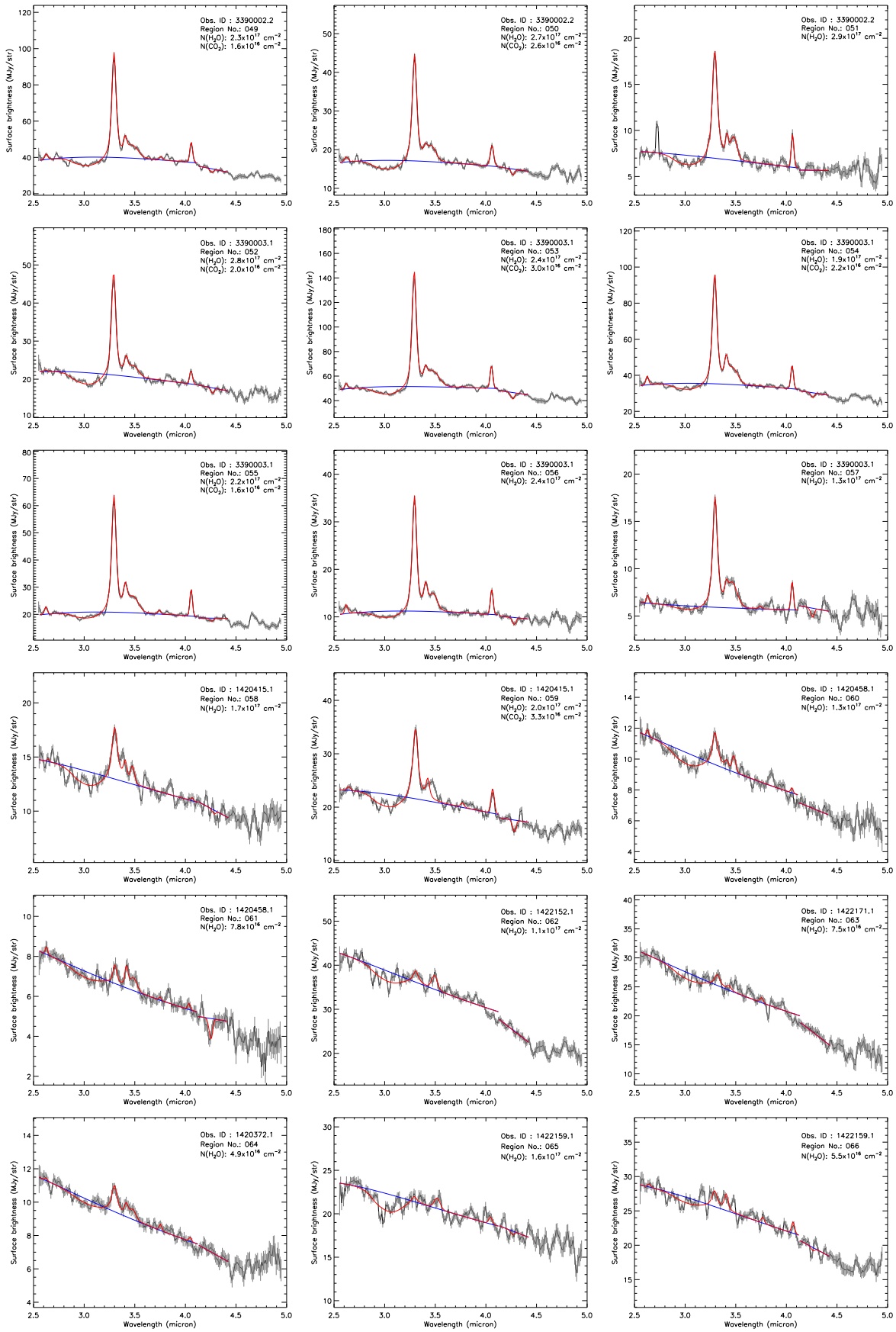

Figure A.1 Continued

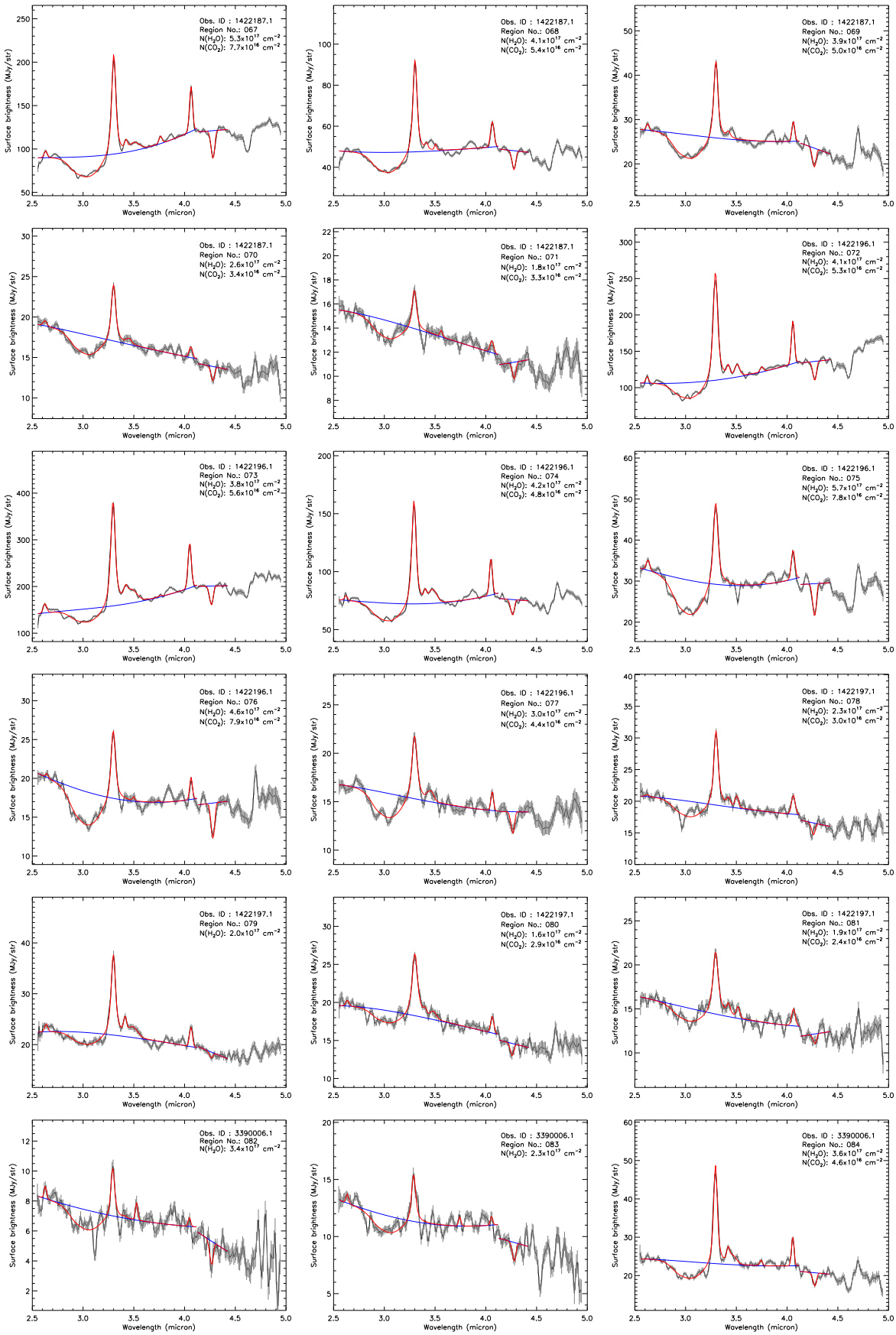

Figure A.1 Continued

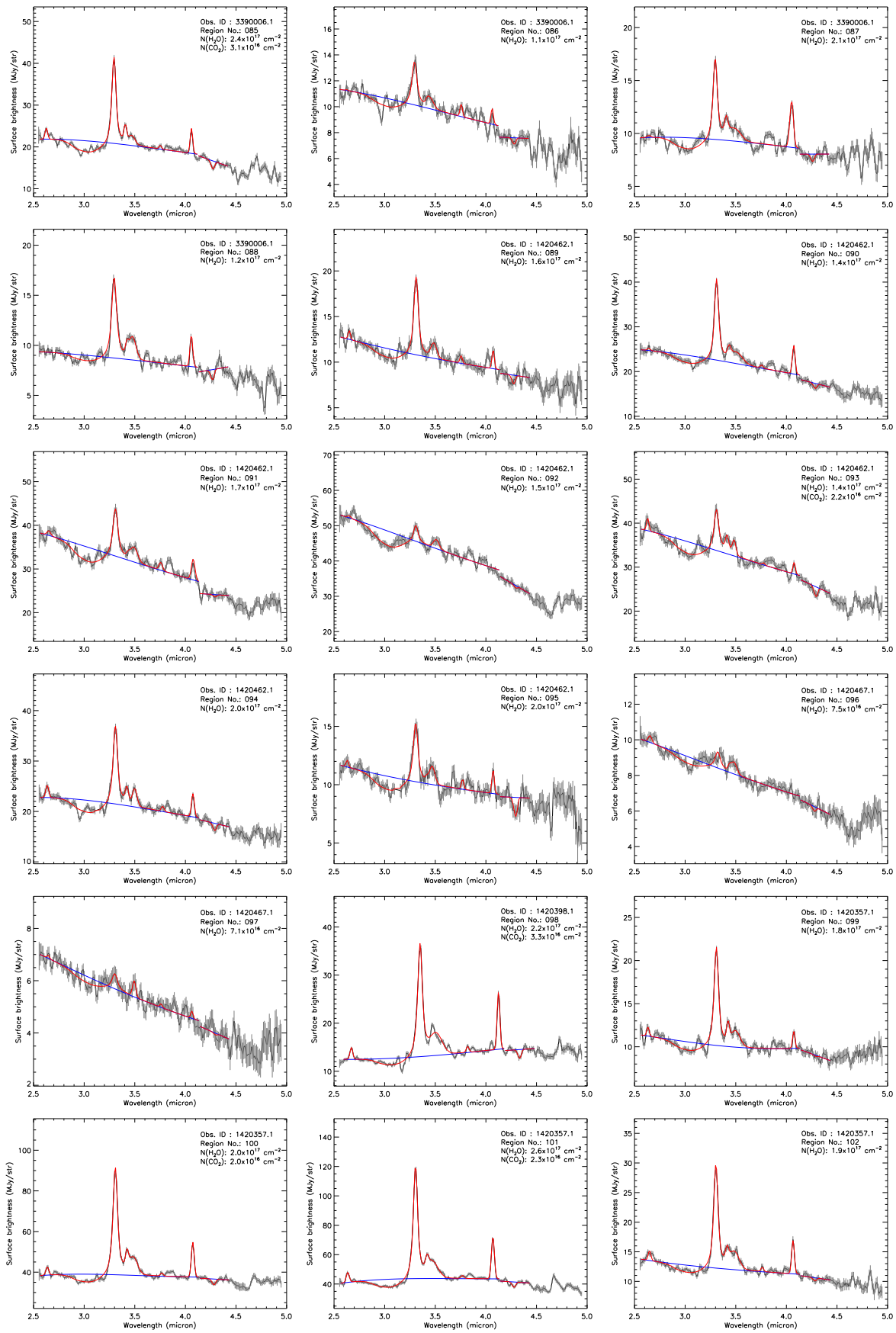

Figure A.1 Continued

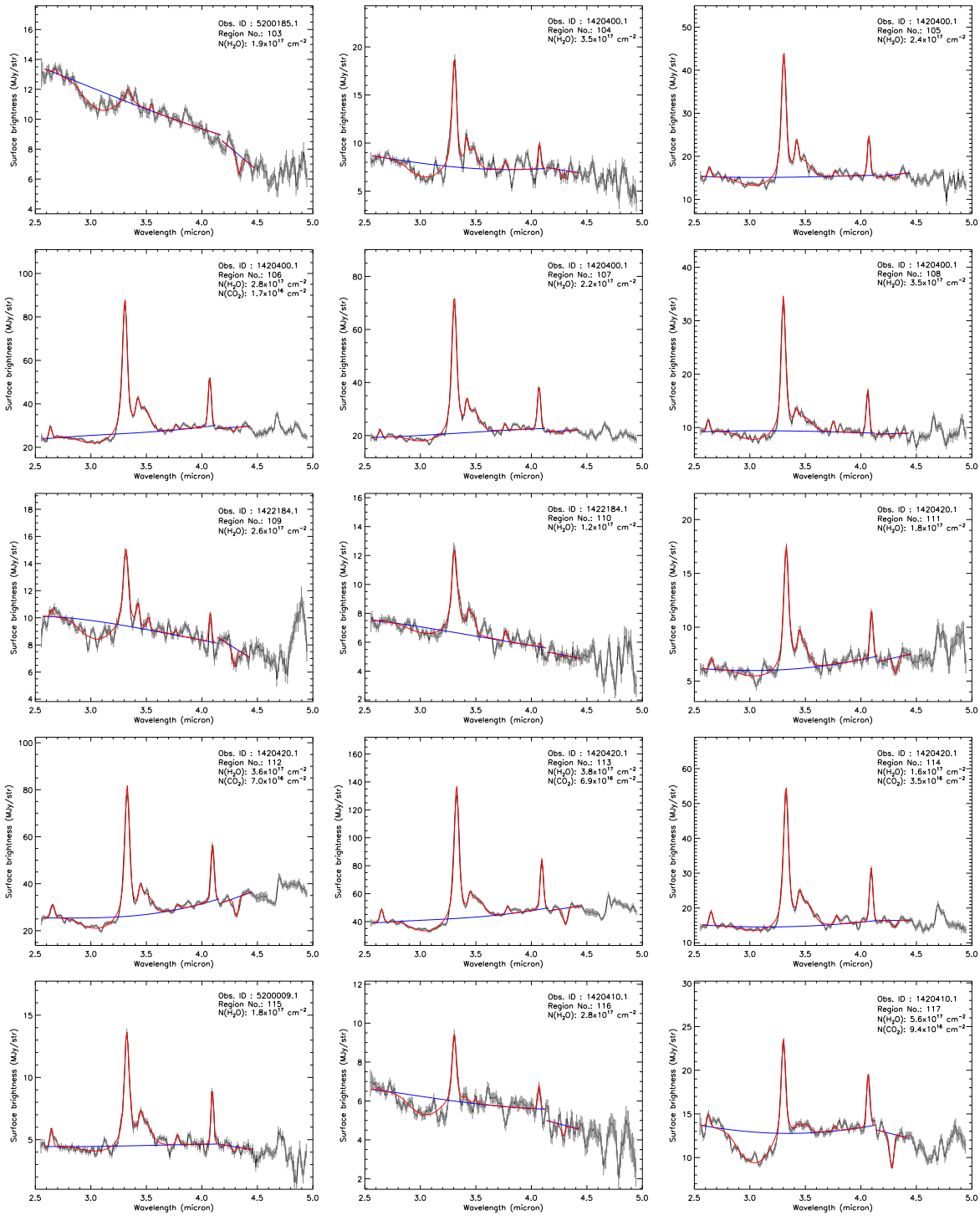

Figure A.1 Continued

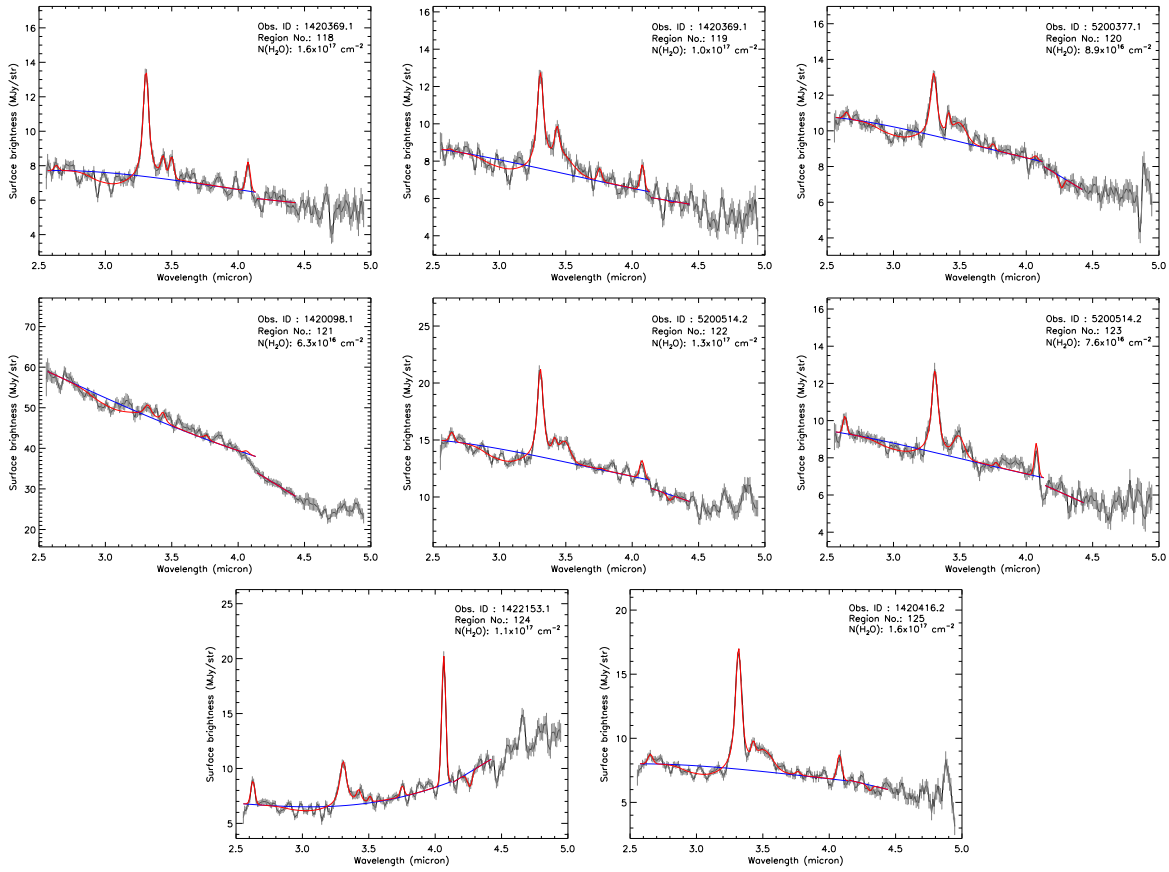

Figure A.1 Continued

Appendix B Dust masses and star formation rates of the galaxies with detection of ices

The dust masses and star formation rates of the galaxies where ices are detected were estimated from the AKARI FIR all-sky diffuse maps. The FIR fluxes of the galaxies are measured by the aperture photometry. The radii used to determine the source flux and sky level for each galaxy were set to $<1.5D_{25}$ and 1.5–2.0R_{25}, respectively, where R_{25} is the radius of the major axis in the optical B band taken from de Vaucouleurs et al. (1991) and SIMBAD astronomical database. The spatial resolution of the FIR maps is $\sim 80''$ which is larger than $1.5R_{25}$ of small galaxies. Therefore, the minimum radius of $3'$ was set to measure all the flux from compact sources (Shirahata et al. 2009). The areas used in the calculations are shown in Fig. B.1, while the resultant fluxes in the 65–160 μm bands are summarized in Table B.1. Figure B.2 shows comparison of the FIR photometric data taken with AKARI and IRAS. In the figure, it is confirmed that the AKARI 65 μm band fluxes are consistent with the IRAS 60 μm band fluxes, while there is a systematic difference between the AKARI 90 μm band fluxes and the IRAS 100 μm band fluxes. Therefore, the AKARI 90 μm band fluxes were not used in the calculations below.

Dust temperatures were estimated by fitting the AKARI FIR SEDs of the galaxies in 65, 140, and 160 μm by a single-temperature graybody model with an emissivity power-law index of $\beta = 1$:

$$I_{\rm d} = A \left(\frac{\nu}{\nu_0}\right)^{\beta} B_\nu(T). \tag{B.1}$$

The result of the fitting calculation for each galaxy is shown in Fig. B.3. The dust mass was calculated by using the following equations:

$$M_{\rm dust} = \frac{4a\rho D^2}{3Q_\nu}\frac{F_\nu}{B_\nu(T)}, \tag{B.2}$$

$$Q_\nu = \frac{3}{4000}\left(\frac{\nu}{\nu_{125\mu{\rm m}}}\right), \tag{B.3}$$

where $M_{\rm dust}$, D, a, and ρ are the dust mass, distance to a galaxy, the average grain radius, and the specific dust mass density, respectively. F_ν , Q_ν, and $B_\nu(T)$ are the observed flux density, grain emissivity, and the value of the Planck function at a frequency of ν and a dust temperature of T. An averaged grain radius of 0.1 μm, and a specific dust mass density of 3 g/cm^3 were adopted. The grain emissivity factor was given by Hildebrand (1983). The star-formation rate (SFR) of each galaxy was also evaluated by using the following equation (Kennicutt 1998):

$$\mathrm{SFR} = 1.7 \times 10^{-10}\frac{L_{\rm IR}}{L_\odot}, \tag{B.4}$$

where $L_{\rm IR}$ is the total luminosity of the dust emission integrated between 1–1000 μm. The resultant $M_{\rm dust}$, T, and SFR are summarized in Table **??**.

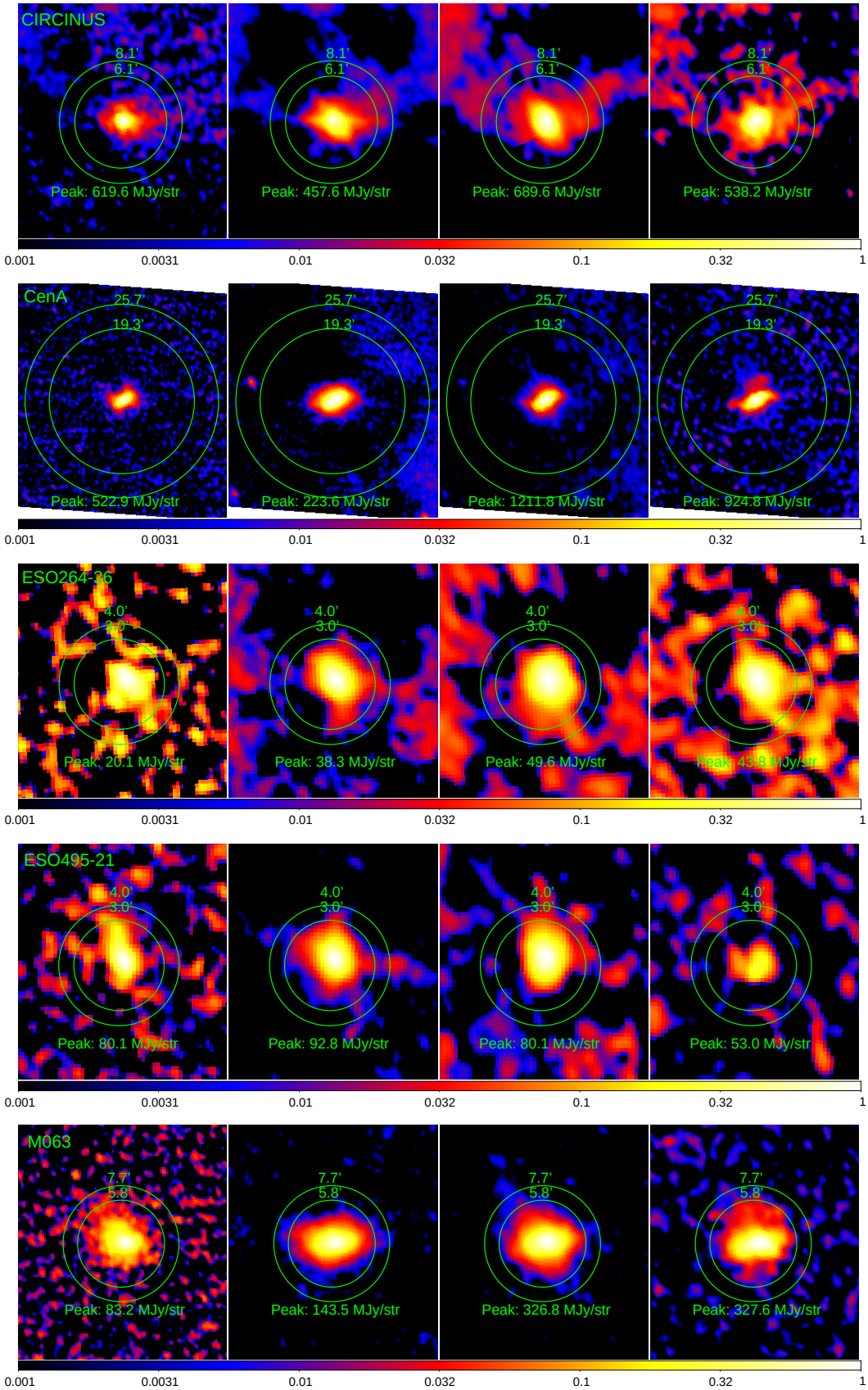

Figure B.1 Areas used to calculate source fluxes and sky levels overlaid on the AKARI FIR all-sky diffuse maps. Each map is normalized to the peak value which is denoted in the figure. The regions within the inner circles were used to calculate the source flux, while those between inner and outer circles were used to calculate the sky level. The radii of inner and outer circles are shown in the upper part.

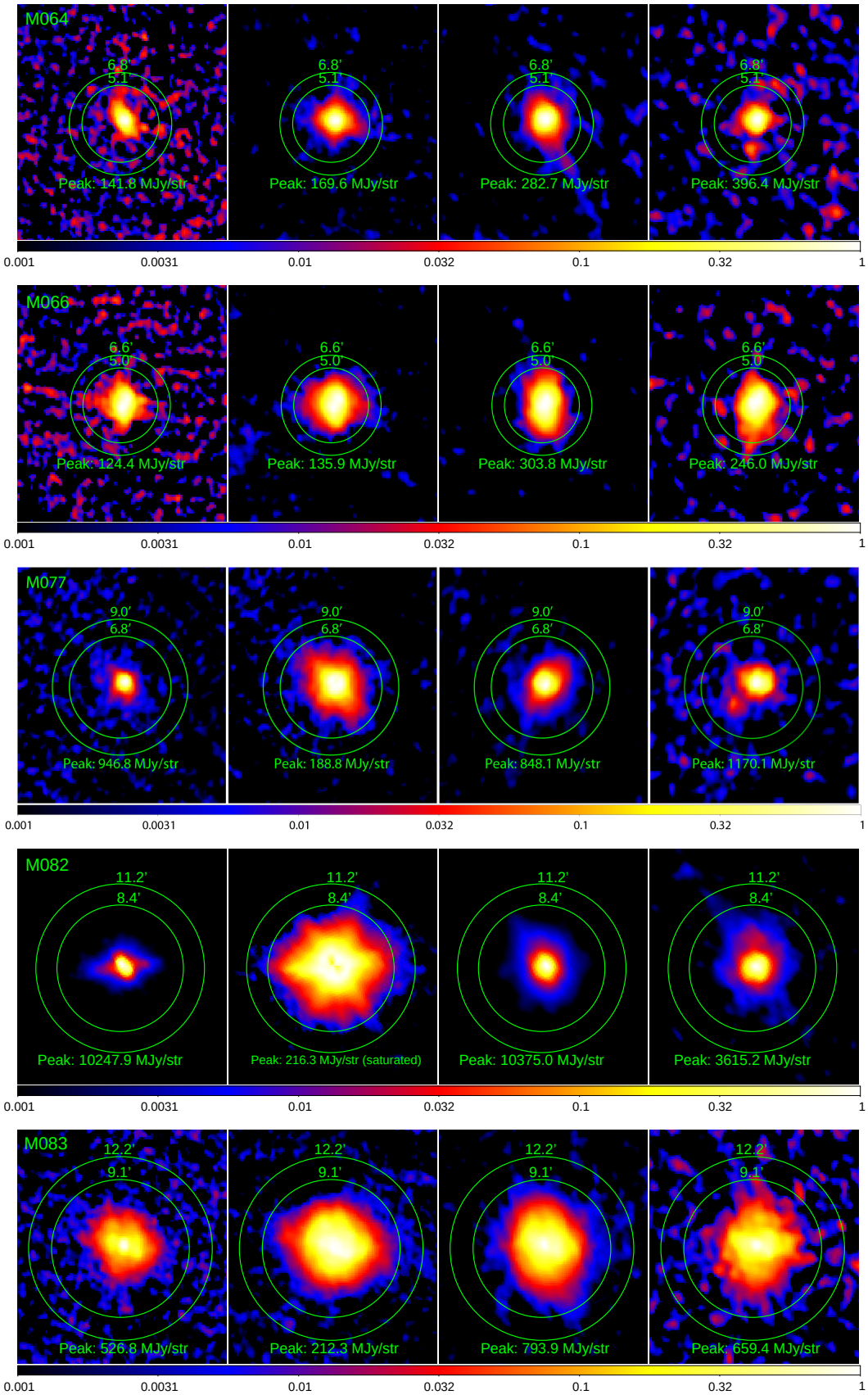

Figure B.1 Continued

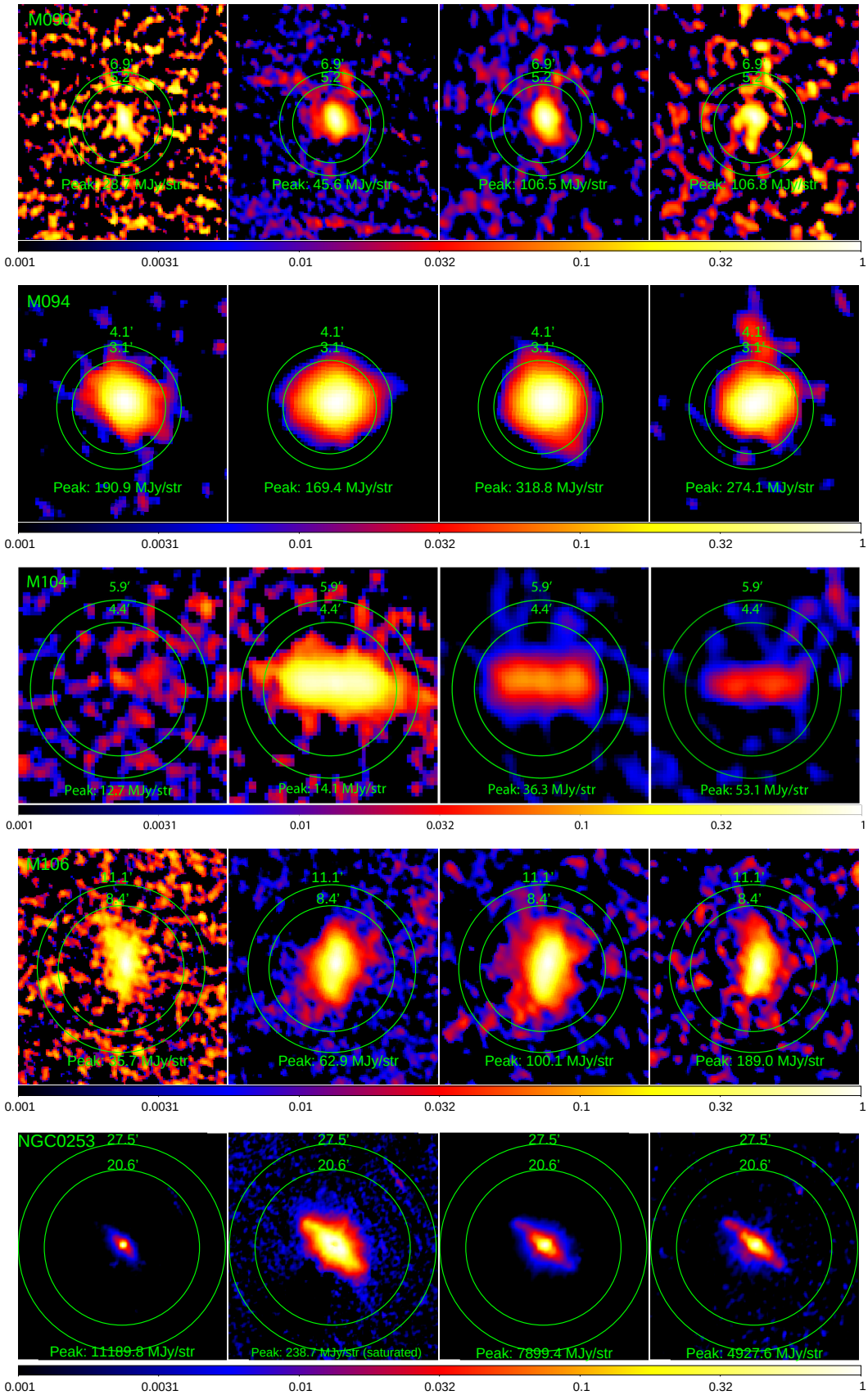

Figure B.1 Continued

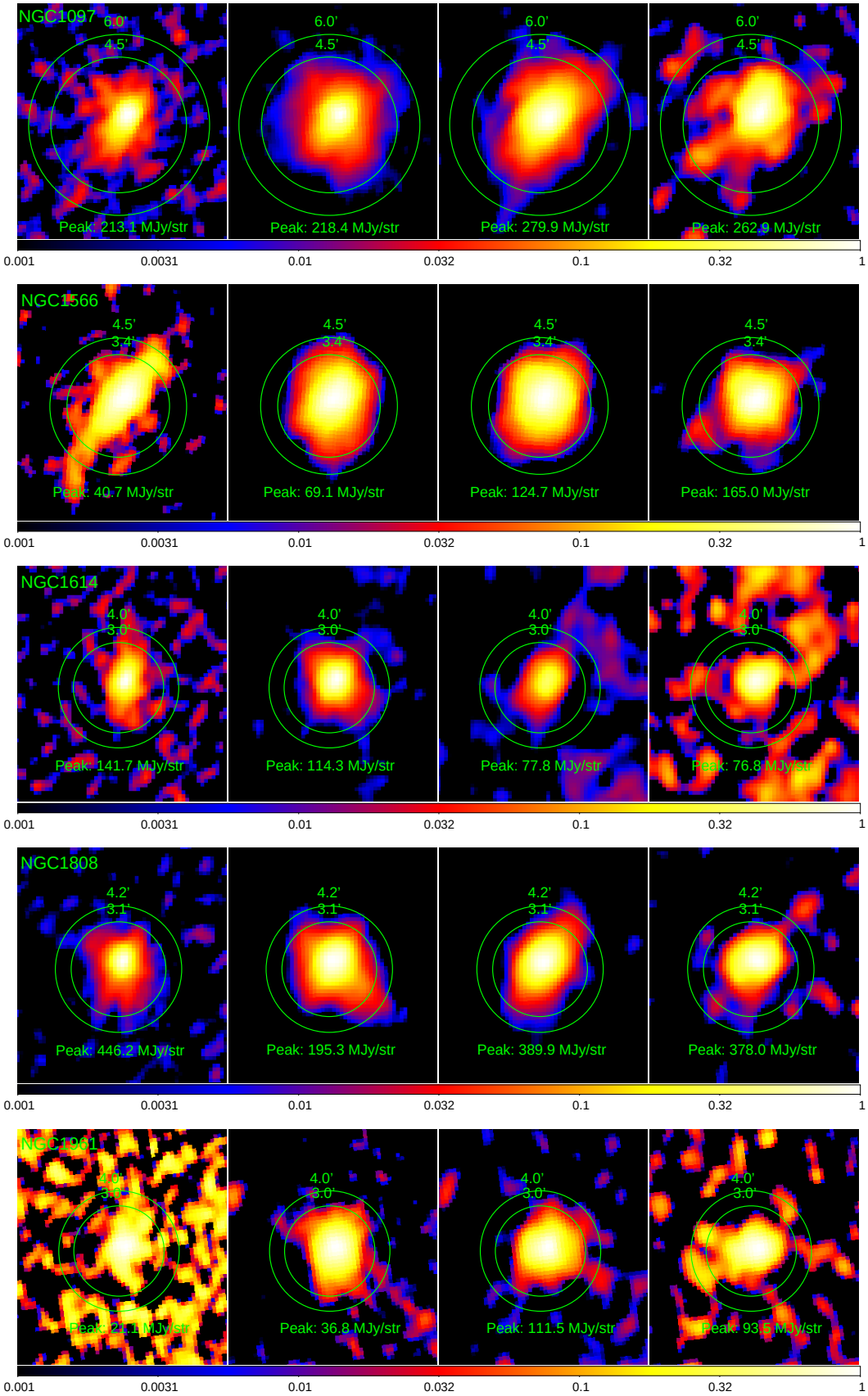

Figure B.1 Continued

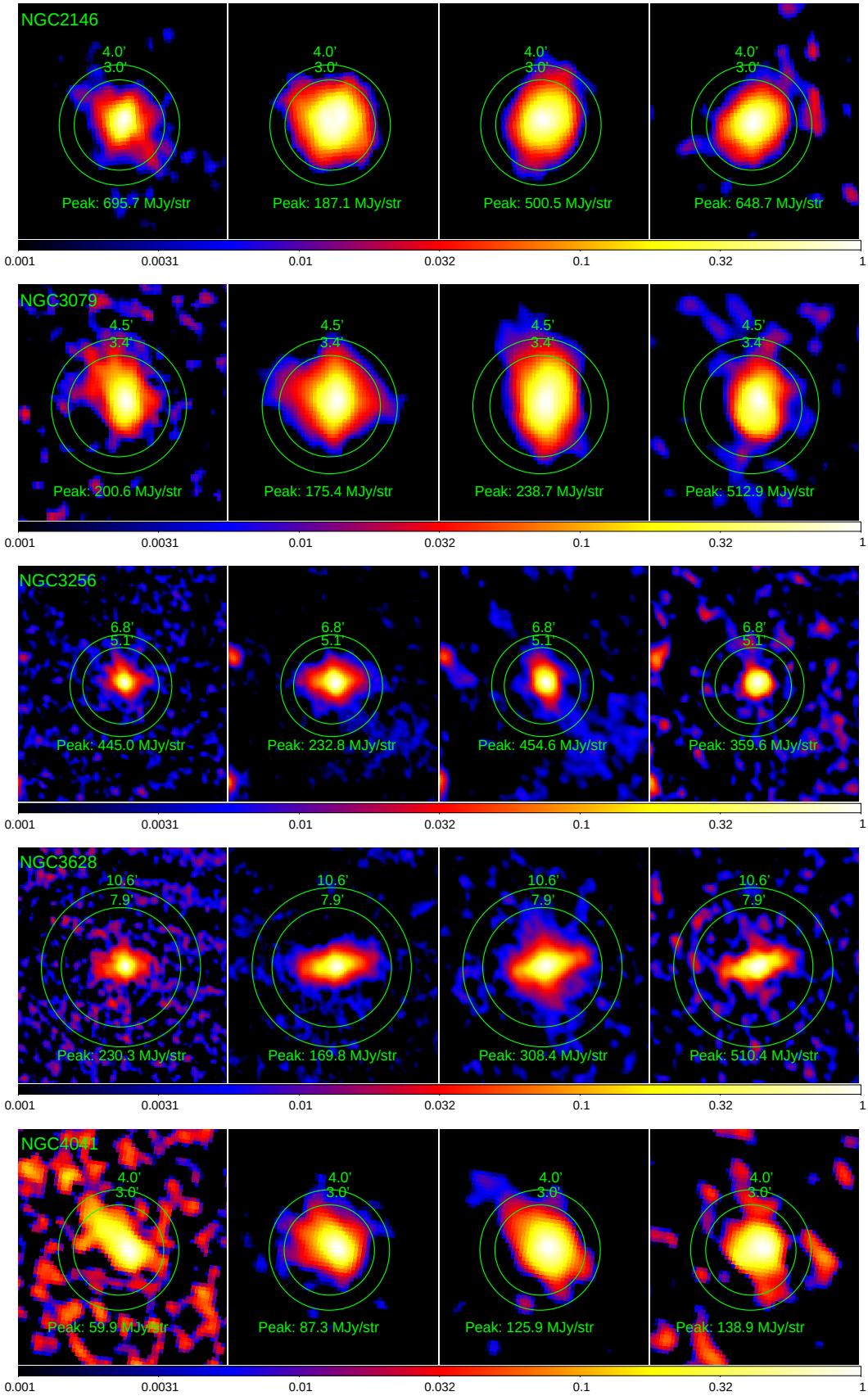

Figure B.1 Continued

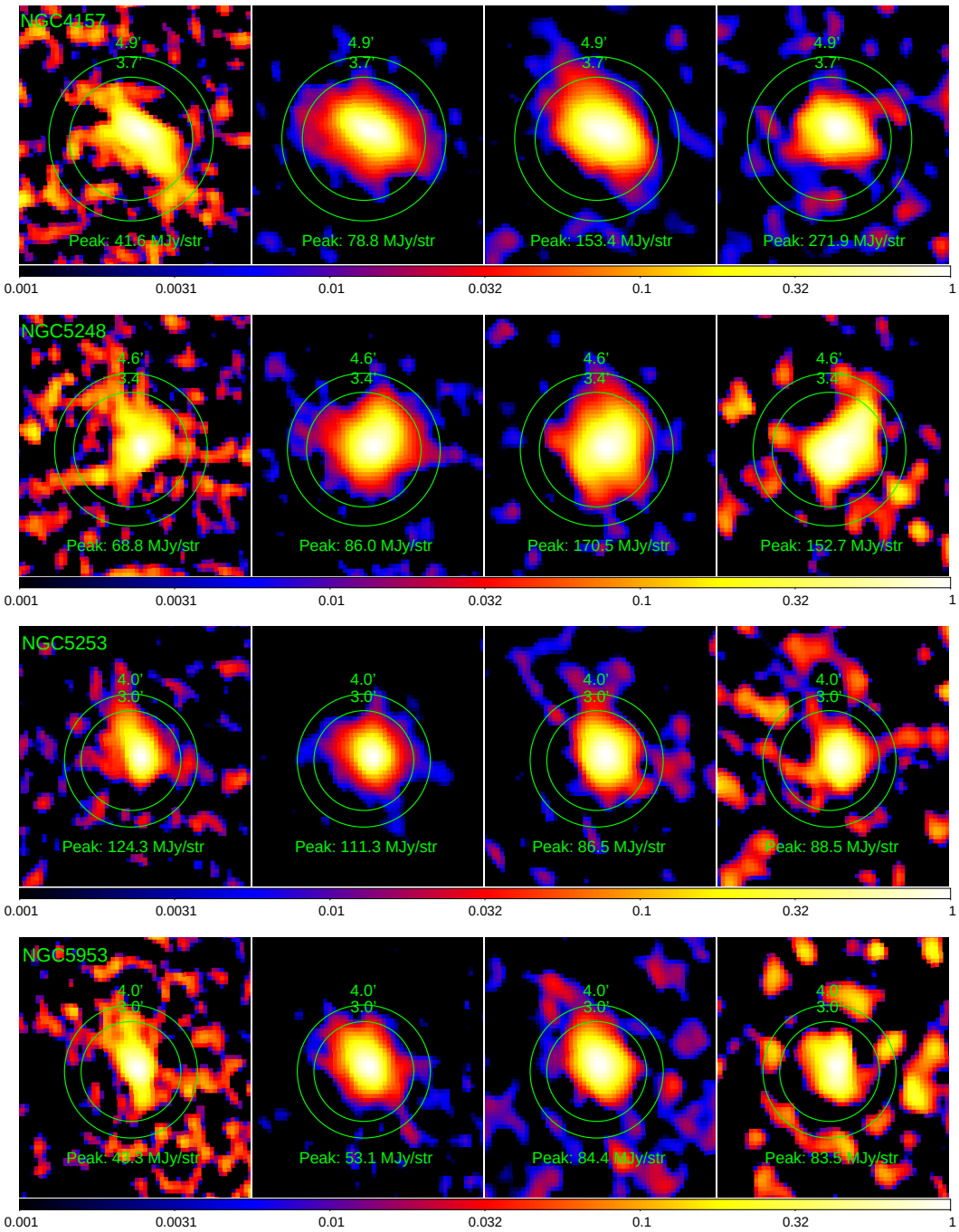

Figure B.1 Continued

Table B.1 Summary of the AKARI FIR photometric data points.

Target	Flux 65 μm (Jy)	Flux 90 μm (Jy)	Flux 140 μm (Jy)	Flux 160 μm (Jy)
CenA	266.8 ± 7.6	270.3 ± 2.9	1020.6 ± 19.8	812.6 ± 21.4
CIRCINUS	148.9 ± 11.7	182.7 ± 5.3	410.7 ± 11.3	327.9 ± 13.3
ESO264-36	4.2 ± 0.7	8.2 ± 0.4	15.8 ± 0.8	12.6 ± 1.3
ESO495-21	15.0 ± 1.4	19.0 ± 1.0	21.2 ± 1.3	10.5 ± 2.0
M063	54.7 ± 1.6	95.0 ± 1.3	266.5 ± 4.5	275.3 ± 7.7
M064	38.0 ± 2.2	51.7 ± 1.7	113.0 ± 4.2	119.6 ± 8.5
M066	62.7 ± 2.2	90.2 ± 1.7	215.6 ± 5.0	170.5 ± 6.2
M077	165.9 ± 13.1	136.5 ± 2.4	279.3 ± 12.5	405.7 ± 24.1
M082	1717.8 ± 142.8	504.7[a]± 4.7	2710.8 ± 168.5	1293.3 ± 72.9
M083	306.2 ± 8.0	410.8 ± 2.5	1104.1 ± 11.6	773.3 ± 14.5
M090	9.0 ± 1.4	16.4 ± 0.5	43.9 ± 1.9	42.8 ± 4.3
M094	59.5 ± 2.4	68.7 ± 1.8	142.5 ± 4.7	118.9 ± 6.4
M104	6.0 ± 1.1	12.5 ± 0.2	37.6 ± 0.9	40.8 ± 2.4
M106	32.9 ± 1.8	57.1 ± 0.6	127.2 ± 1.7	134.2 ± 4.6
NGC0253	1573.2 ± 142.6	735.8[a]± 4.7	4117.1 ± 117.6	2864.4 ± 93.7
NGC1097	52.2 ± 3.0	67.9 ± 1.9	137.9 ± 4.5	129.3 ± 6.3
NGC1566	20.4 ± 0.7	36.1 ± 0.6	73.7 ± 1.8	70.3 ± 2.9
NGC1614	23.3 ± 2.0	23.8 ± 1.2	21.8 ± 1.4	18.9 ± 1.8
NGC1808	69.7 ± 5.7	69.9 ± 2.0	128.2 ± 5.7	115.3 ± 7.7
NGC1961	8.4 ± 1.1	14.6 ± 0.4	38.5 ± 1.8	34.1 ± 2.6
NGC2146	108.8 ± 11.3	81.2 ± 2.6	160.8 ± 8.8	174.9 ± 13.4
NGC3079	42.0 ± 2.4	51.9 ± 1.6	95.4 ± 4.0	135.1 ± 11.4
NGC3256	77.9 ± 5.6	79.8 ± 2.1	125.4 ± 7.0	102.8 ± 7.6
NGC3628	59.8 ± 3.4	69.8 ± 1.6	198.0 ± 4.3	268.5 ± 12.2
NGC4041	15.7 ± 1.1	18.7 ± 0.8	40.4 ± 1.9	39.0 ± 2.9
NGC4157	16.3 ± 1.0	28.5 ± 0.8	77.1 ± 2.6	92.7 ± 5.6
NGC5248	21.6 ± 1.4	32.7 ± 0.8	81.0 ± 2.8	91.6 ± 5.9
NGC5253	24.9 ± 1.7	22.6 ± 1.1	28.2 ± 1.5	24.7 ± 2.6
NGC5953	10.7 ± 0.9	14.1 ± 0.5	27.3 ± 1.4	21.3 ± 2.5

[a] Saturated.

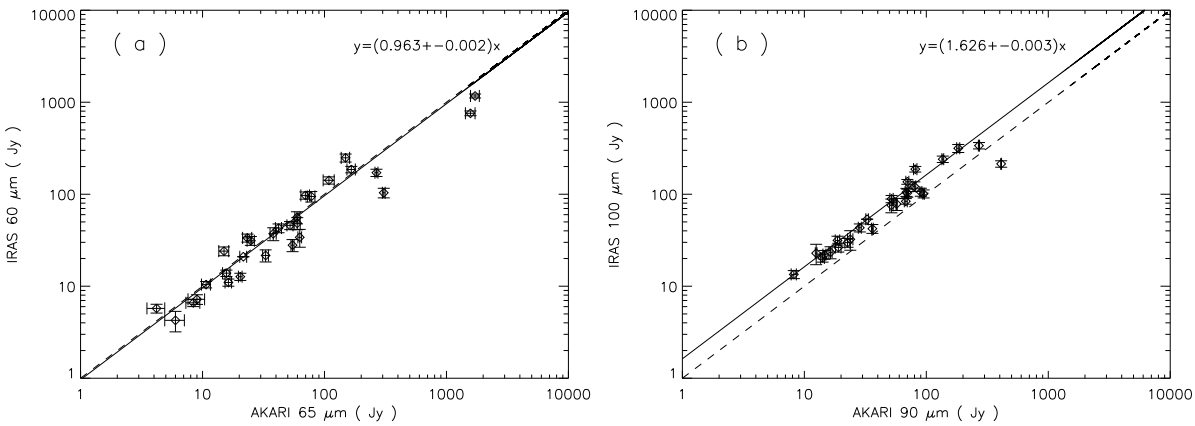

Figure B.2 Comparison of the AKARI and IRAS FIR photometric data points of galaxies with detection of ices: (a) IRAS 60 μm vs. AKARI 65 μm. (b) IRAS 100 μm vs. AKARI 90 μm. The dashed and solid lines represent $y = x$ and the best-fit linear relation, respectively. The best-fit parameters of the linear relation are indicated in the figure. The data with IRAS were taken from Beichman et al. (1988).

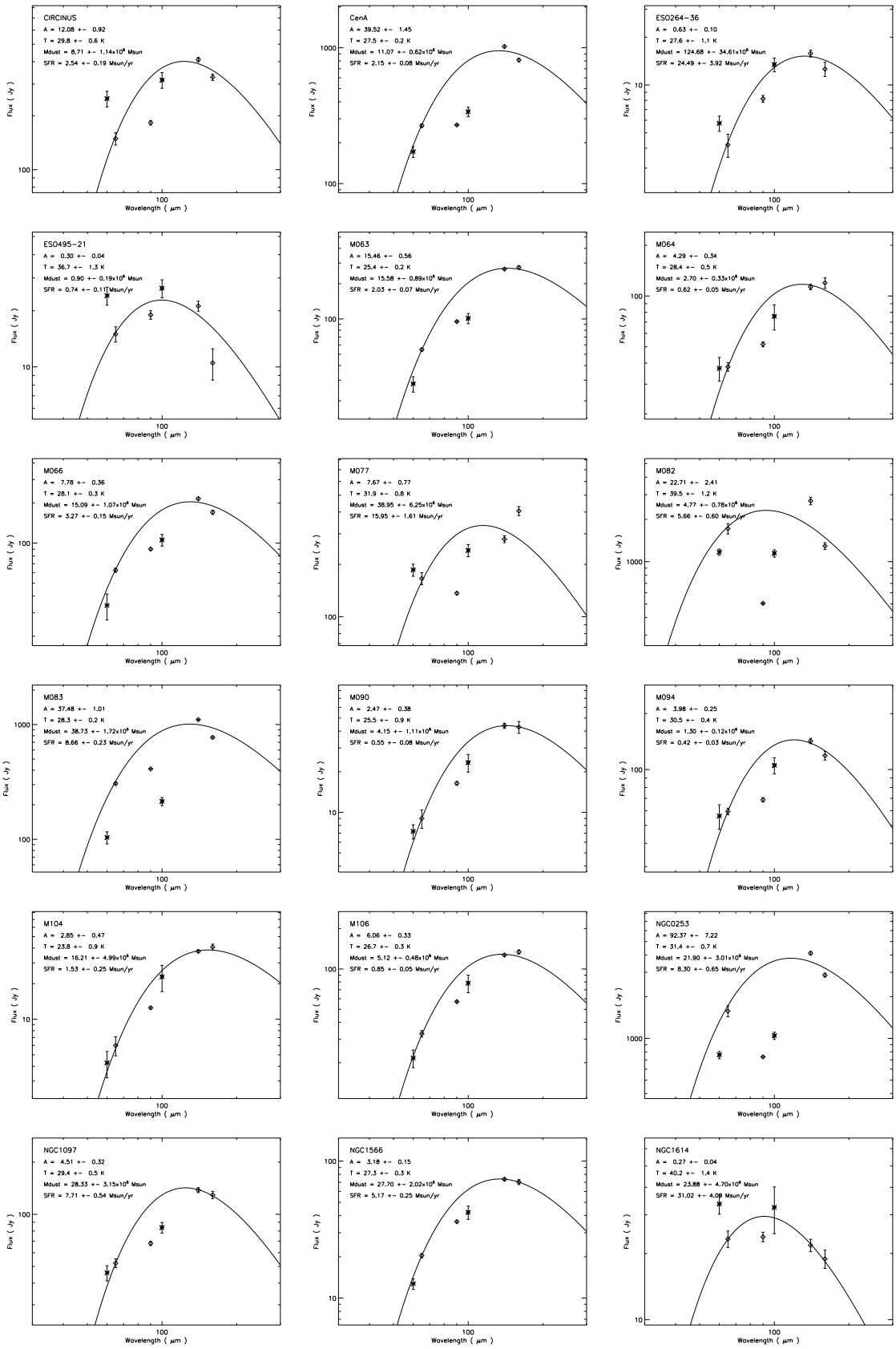

Figure B.3 FIR photometric data points are plotted together with the best-fit graybody curve. The diamonds and asterisks indicate the data taken with AKARI and IRAS, respectively. The solid curve indicates the best-fit graybody model ($\beta = 1$) fitted to the AKARI FIR (65, 140, and 160 μm) data points.

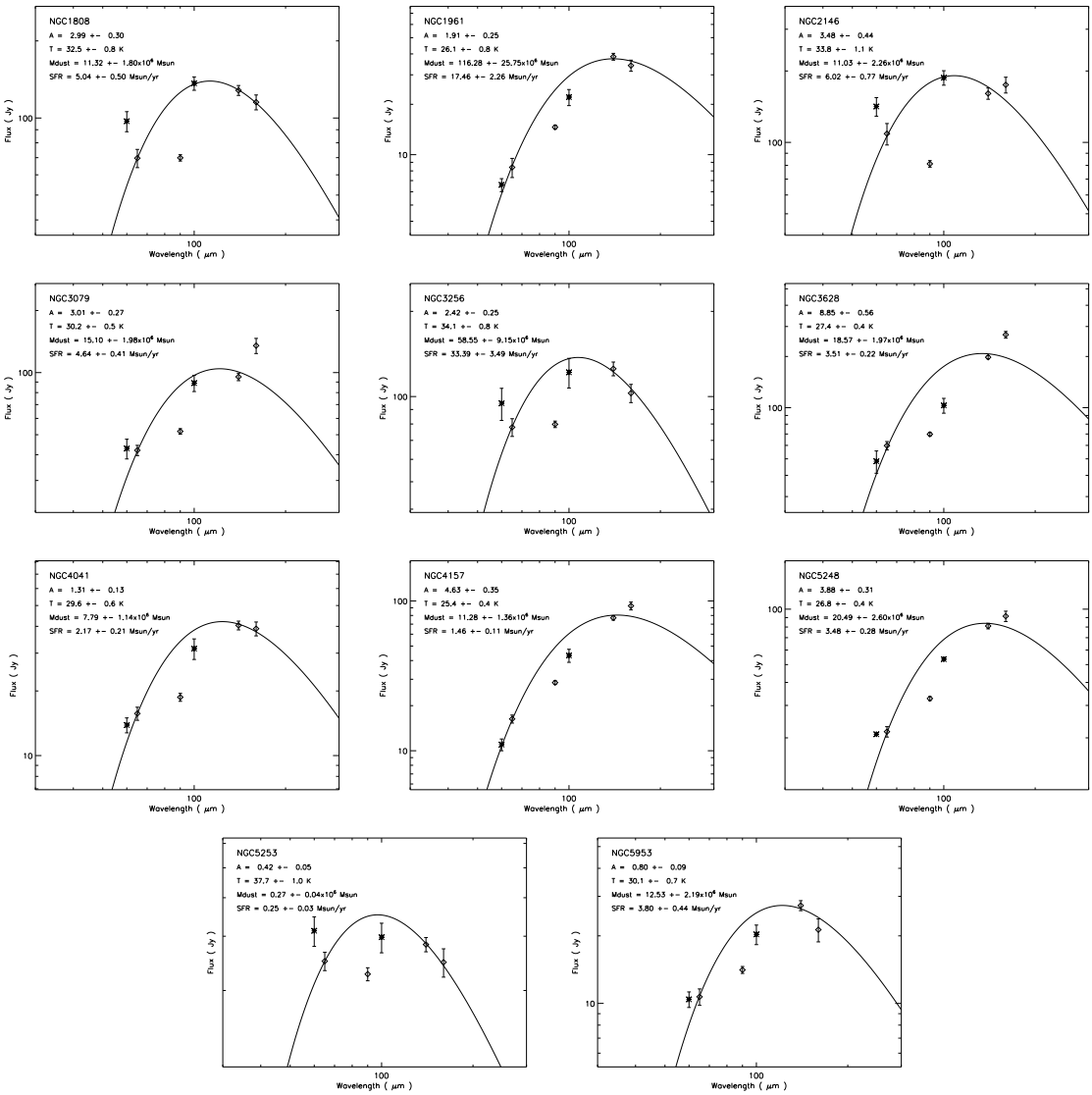

Figure B.3 Continued

References

Abdo, A. A., Ackermann, M., Ajello, M., et al. 2010, ApJ, 709, L152

Allamandola, L. J., Tielens, A. G. G. M., & Barker, J. R. 1989, ApJS, 71, 733

Baker, J. G., & Menzel, D. H. 1938, ApJ, 88, 52

Beichman, C. A., Neugebauer, G., Habing, H. J., Clegg, P. E., & Chester, T. J. 1988, Infrared astronomical satellite (IRAS) catalogs and atlases. Volume 1: Explanatory supplement, 1

Bergin, E. A., Neufeld, D. A., & Melnick, G. J. 1999, ApJ, 510, L145

Bergman, P., Parise, B., Liseau, R., et al. 2011, A&A, 531, L8

Blitz, L., & Shu, F. H. 1980, ApJ, 238, 148

Boogert, A. C. A., Chiar, J. E., Knez, C., et al. 2013, ApJ, 777, 73

Boogert, A. C. A., & Ehrenfreund, P. 2004, in Astronomical Society of the Pacific Conference Series, Vol. 309, Astrophysics of Dust, ed. A. N. Witt, G. C. Clayton, & B. T. Draine, 547

Boogert, A. C. A., Pontoppidan, K. M., Knez, C., et al. 2008, ApJ, 678, 985

Bottinelli, S., Boogert, A. C. A., Bouwman, J., et al. 2010, ApJ, 718, 1100

Brooke, T. Y., Sellgren, K., & Geballe, T. R. 1999, ApJ, 517, 883

Burke, D. J., & Brown, W. A. 2010, Physical Chemistry Chemical Physics (Incorporating Faraday Transactions), 12, 5947

Ceccarelli, C., Hily-Blant, P., Montmerle, T., et al. 2011, ApJ, 740, L4

Chiar, J. E., Adamson, A. J., & Whittet, D. C. B. 1996, ApJ, 472, 665

Chiar, J. E., Pendleton, Y. J., Allamandola, L. J., et al. 2011, ApJ, 731, 9

Cuppen, H. M., & Herbst, E. 2007, ApJ, 668, 294

de Vaucouleurs, G., de Vaucouleurs, A., Corwin, Jr., H. G., et al. 1991, Third Reference Catalogue of Bright Galaxies. Volume I: Explanations and references. Volume II: Data for galaxies between 0^h and 12^h. Volume III: Data for galaxies between 12^h and 24^h.

D'Hendecourt, L. B., Allamandola, L. J., & Greenberg, J. M. 1985, A&A, 152, 130

Draine, B. T. 2003, ARA&A, 41, 241

Draine, B. T., & Li, A. 2007, ApJ, 657, 810

Dudley, C. C., & Wynn-Williams, C. G. 1999, MNRAS, 304, 549

Ehrenfreund, P., Boogert, A. C. A., Gerakines, P. A., et al. 1996, A&A, 315, L341

Eiroa, C., & Hodapp, K.-W. 1989, A&A, 210, 345

Garrod, R. T., & Pauly, T. 2011, ApJ, 735, 15

Geballe, T. R., & Oka, T. 2010, ApJ, 709, L70

Gerakines, P. A., Schutte, W. A., Greenberg, J. M., & van Dishoeck, E. F. 1995, A&A, 296, 810

Gerakines, P. A., Whittet, D. C. B., Ehrenfreund, P., et al. 1999, ApJ, 522, 357

Gerin, M., Combes, F., & Nakai, N. 1988, A&A, 203, 44

Gibb, E. L., Whittet, D. C. B., Boogert, A. C. A., & Tielens, A. G. G. M. 2004, ApJS, 151, 35
Gibb, E. L., Whittet, D. C. B., Schutte, W. A., et al. 2000, ApJ, 536, 347
Gillett, F. C., & Forrest, W. J. 1973, ApJ, 179, 483
Goto, M., Usuda, T., Nagata, T., et al. 2008, ApJ, 688, 306
Grim, R. J. A., & Greenberg, J. M. 1987, ApJ, 321, L91
Herbst, E., & Leung, C. M. 1986, MNRAS, 222, 689
Hildebrand, R. H. 1983, QJRAS, 24, 267
Hsieh, P.-Y., Matsushita, S., Lim, J., Kohno, K., & Sawada-Satoh, S. 2008, ApJ, 683, 70
Hsieh, P.-Y., Matsushita, S., Liu, G., et al. 2011, ApJ, 736, 129
Hummer, D. G., & Storey, P. J. 1987, MNRAS, 224, 801
Imanishi, M., Nakagawa, T., Shirahata, M., Ohyama, Y., & Onaka, T. 2010, ApJ, 721, 1233
Indriolo, N., Blake, G. A., Goto, M., et al. 2010, ApJ, 724, 1357
Kaneda, H., Ishihara, D., Suzuki, T., et al. 2010, A&A, 514, A14
Karachentsev, I. D., Dolphin, A. E., Geisler, D., et al. 2002, A&A, 383, 125
Kawada, M., Baba, H., Barthel, P. D., et al. 2007, PASJ, 59, 389
Kennicutt, Jr., R. C. 1998, ARA&A, 36, 189
Keto, E., Hora, J. L., Fazio, G. G., Hoffmann, W., & Deutsch, L. 1999, ApJ, 518, 183
Kohno, K., Ishizuki, S., Matsushita, S., Vila-Vilaró, B., & Kawabe, R. 2003, PASJ, 55, L1
Kondo, T., Kaneda, H., Oyabu, S., et al. 2012, ApJ, 751, L18
Kornei, K. A., & McCrady, N. 2009, ApJ, 697, 1180
Kuno, N., Sato, N., Nakanishi, H., et al. 2007, PASJ, 59, 117
Lacy, J. H., Baas, F., Allamandola, L. J., et al. 1984, ApJ, 276, 533
Luck, R. E., Moffett, T. J., Barnes, III, T. G., & Gieren, W. P. 1998, AJ, 115, 605
Miyauchi, N., Hidaka, H., Chigai, T., et al. 2008, Chemical Physics Letters, 456, 27
Mori, T., Oyabu, S., Kaneda, H., Ishihara, D., & Yamagishi, M. 2012, Publication of Korean Astronomical Society, 27, 263
Murakami, H., Baba, H., Barthel, P., et al. 2007, PASJ, 59, 369
Noble, J. A., Dulieu, F., Congiu, E., & Fraser, H. J. 2011, ApJ, 735, 121
Oba, Y., Watanabe, N., Hama, T., et al. 2012, ApJ, 749, 67
Oba, Y., Watanabe, N., Kouchi, A., Hama, T., & Pirronello, V. 2010, ApJ, 712, L174
Öberg, K. I., Boogert, A. C. A., Pontoppidan, K. M., et al. 2008, ApJ, 678, 1032
—. 2011, ApJ, 740, 109
Öberg, K. I., Fraser, H. J., Boogert, A. C. A., et al. 2007, A&A, 462, 1187
Ohyama, Y., Onaka, T., Matsuhara, H., et al. 2007, PASJ, 59, 411
Onaka, T., Matsuhara, H., Wada, T., et al. 2007, PASJ, 59, 401
Pontoppidan, K. M., Boogert, A. C. A., Fraser, H. J., et al. 2008, ApJ, 678, 1005
Prasad, S. S., & Tarafdar, S. P. 1983, ApJ, 267, 603
Rekola, R., Richer, M. G., McCall, M. L., et al. 2005, MNRAS, 361, 330
Ruffle, D. P., & Herbst, E. 2001, MNRAS, 324, 1054
Sajina, A., Spoon, H., Yan, L., et al. 2009, ApJ, 703, 270
Sakamoto, K., Mao, R.-Q., Matsushita, S., et al. 2011, ApJ, 735, 19
Shaw, M. A., Combes, F., Axon, D. J., & Wright, G. S. 1993, A&A, 273, 31

Shen, C. J., Greenberg, J. M., Schutte, W. A., & van Dishoeck, E. F. 2004, A&A, 415, 203

Shimonishi, T., Onaka, T., Kato, D., et al. 2010, A&A, 514, A12

Shirahata, M., Nakagawa, T., Usuda, T., et al. 2013, PASJ, 65, 5

Shirahata, M., Matsuura, S., Hasegawa, S., et al. 2009, PASJ, 61, 737

Soifer, B. T., Puetter, R. C., Russell, R. W., et al. 1979, ApJ, 232, L53

Spoon, H. W. W., Keane, J. V., Tielens, A. G. G. M., et al. 2002, A&A, 385, 1022

Spoon, H. W. W., Koornneef, J., Moorwood, A. F. M., Lutz, D., & Tielens, A. G. G. M. 2000, A&A, 357, 898

Spoon, H. W. W., Moorwood, A. F. M., Pontoppidan, K. M., et al. 2003, A&A, 402, 499

Storchi-Bergmann, T., Baldwin, J. A., & Wilson, A. S. 1993, ApJ, 410, L11

Sturm, E., Lutz, D., Tran, D., et al. 2000, A&A, 358, 481

Tanaka, M., Sato, S., Nagata, T., & Yamamoto, T. 1990, ApJ, 352, 724

Tielens, A. G. G. M. 2005, The Physics and Chemistry of the Interstellar Medium

Tielens, A. G. G. M., & Hagen, W. 1982, A&A, 114, 245

Tielens, A. G. G. M., Tokunaga, A. T., Geballe, T. R., & Baas, F. 1991, ApJ, 381, 181

Tsumura, K., Matsumoto, T., Matsuura, S., et al. 2013, PASJ, 65, 119

Tully, R. B. 1988, Nearby galaxies catalog

van der Tak, F. F. S., van Dishoeck, E. F., & Caselli, P. 2000, A&A, 361, 327

Walter, F., Weiss, A., & Scoville, N. 2002, ApJ, 580, L21

Watanabe, N., & Kouchi, A. 2002, ApJ, 567, 651

Watanabe, N., Mouri, O., Nagaoka, A., et al. 2007, ApJ, 668, 1001

Webber, W. R. 1998, ApJ, 506, 329

Webster, B. L., & Smith, M. G. 1983, MNRAS, 204, 743

Westmoquette, M. S., Smith, L. J., Gallagher, III, J. S., et al. 2007, ApJ, 671, 358

Whittet, D. C. B. 2003, Dust in the galactic environment

Whittet, D. C. B., Bode, M. F., Longmore, A. J., et al. 1988, MNRAS, 233, 321

Whittet, D. C. B., Shenoy, S. S., Bergin, E. A., et al. 2007, ApJ, 655, 332

Whittet, D. C. B., Gerakines, P. A., Tielens, A. G. G. M., et al. 1998, ApJ, 498, L159

Willick, J. A., Courteau, S., Faber, S. M., et al. 1997, ApJS, 109, 333

Yamada, R., Oyabu, S., Kaneda, H., et al. 2013, ArXiv e-prints, arXiv:1307.6356

Yamagishi, M., Kaneda, H., Ishihara, D., et al. 2012, A&A, 541, A10

—. 2011, ApJ, 731, L20

—. 2013, ApJ, 773, L37

Yu, H. 2001, Chemical Physics Letters, 349, 547

Yun, M. S., Ho, P. T. P., & Lo, K. Y. 1993, ApJ, 411, L17

Acknowledgments

First, I would like to give special thanks to my supervisor Prof. Hidehiro Kaneda. For six years in Uir laboratory, he gave me useful and incisive comments. I respect him for his extensive knowledge about both science and experiments including the ISM, galaxies, optics, and semiconductors.

Additionally, many people supported this study. I would like to thank Dr. Shinki Oyabu, Dr. Daisuke Ishihara, and Dr. Takahiro Nagayama. Dr. Oyabu and Dr. Ishihara gave me many pieces of knowledge and information on the AKARI data analysis, which were necessary to write this thesis. Dr. Nagayama taught me the basics of ground-based observations, which are helpful not only to analyze data taken with ground-based telescopes but also to take a larger view on observations. It was valuable experience for me to operate the IRSF telescope and observe targets personally. I also thank the co-authors of the refereed papers. They gave me valuable comments to improve the theses. Prof. Takashi Onaka pointed out profound issues about the discussions. Dr. Takashi Shimonishi deeply discussed various topics of ices with me. I thank all the members of the AKARI project. This work is based on observations with AKARI, a JAXA project with the participation of ESA.

Finally, I am grateful to the friends in the doctoral course and all the students in Uir laboratory (particularly, Tomita-kun, Kondo-kun, and Yamada-san). They supported this study in many ways, and provided mental support for me, which was crucial to complete this thesis.